FREQUENCIES AND AMPLITUDES OF HIGH-DEGREE SOLAR OSCILLATIONS

Thesis by
James Morris Kaufman

In Partial Fulfillment of the Requirements
for the Degree of
Doctor of Philosophy

California Institute of Technology
Pasadena, California

1991
(Submitted November 2, 1990)

ACKNOWLEDGEMENTS

This thesis would not have been possible without the help of my advisor, Prof. Ken Libbrecht. His guidance (*"Well... if I were doing it, this is how I'd do it..."*), support (*"Ahhh!!! You'll figure it out!"*), and patience (*"Science marches on..."*) have been indispensible. I have had hours and hours of very useful discussions (which always seem to start at 5 o'clock in the afternoon) with Dr. Martin Woodard. Dr. Pawan Kumar has kept me honest, at least theoretically. In addition to explaining all the theoretical aspects of solar oscillations, Pawan has become a very close friend (*"This is your Captain speaking... "*). Prof. Peter Goldreich (and also Pawan) have made this work worthwhile by continually expressing interest in the results. Dr. Dale Gary (Astronomer Extraordinaire and Master of Style) has patiently put up with thousands of my computing/plotting/TEXing questions (some of which weren't even too stupid) (*"Thanks, Dr. GENPLOT."*). The observations described in this thesis were made using the BBSO VMG system. Observing time was provided through the courtesy of Prof. Hal Zirin. Dr. Haimin Wang has provided me with insight into some of the more interesting observable aspects of the Sun, such as convection and magnetic fields (*"Well... I suppose life isn't so tough anymore."*). Jeff Nenow's cleverness, inventiveness, photo wizardry, and stimulating conversation have never ceased to amaze me (*"So... ah... Jeff!"*). Terri Griffin ably undertook Jeff's photo lab duties after his move to bigger and better things at BBSO.

The observations in this thesis could not have been carried out without the help of the BBSO staff: Dr. Alan Patterson, Bill Marquette, Randy Fear, Curtis Odell, Dr. John Varsik, and Melinda Hope. Alan's help was essential in that he modified the VMG programs to allow for the collection of the limb profile data. Furthermore, I could not have carried out the observations were it not for the presence of three individuals at Big Bear whose time is spent onshore: Max, Sunshine, and Fringes. The BBSO engineering staff (Rich Goeden, Simon Groesz, and Denny Dingley) has managed to overcome seemingly insurmountable odds and has kept things in

running condition. Our Administrative Assistant, Nora Knicker, has kept this nut house running more or less smoothly. Her inquiries into the color of my underwear have been most stimulating. She has also taken great pleasure in pointing out all of my grammatical foibles as she read through this thesis (*"What do you want, you Miserable Worm?!?"*).

During my tenure at Caltech, in addition to learning how to "do science," I have learned a very important lesson: There's more to life than physics. Three members of my class have been instrumental in helping me realize this simple fact: Eric Aslakson, Gary Gutt, and Chris Starr. They have also been very good friends over the years. My officemate, Michal Peri, was also a good friend during the past few years. The Caltech/JPL Flying Club has provided me with an interesting (although some would say time-consuming) diversion from the usual humdrum at Caltech. A word of gratitude should also be said to the Teledyne Continental and Avco Lycoming companies for their reliable products. ✈

This work has been supported by the National Science Foundation [ATM-8907012] and for three years by a NASA Graduate Student Researchers Program Fellowship [NGT-50187].

To my parents

who have been there through the thick and the thin of it all

ABSTRACT

Measurements of some of the properties of high-degree solar p- and f-mode oscillations are presented. Using high-resolution velocity images from Big Bear Solar Observatory, we have measured mode frequencies, which provide information about the composition and internal structure of the Sun, and mode velocity amplitudes (corrected for the effects of atmospheric seeing), which tell us about the oscillation excitation and damping mechanisms.

We present a new and more accurate table of the Sun's acoustic vibration frequencies, $\nu_{n\ell}$, as a function of radial order n and spherical harmonic degree ℓ. These frequencies are averages over azimuthal order m and approximate the normal mode frequencies of a nonrotating, spherically symmetric Sun near solar minimum. The frequencies presented here are for solar p- and f-modes with $180 \leq \ell \leq 1920$, $0 \leq n \leq 8$, and $1.7\,\mathrm{mHz} \leq \nu_{n\ell} \leq 5.3\,\mathrm{mHz}$. The uncertainties, $\sigma_{n\ell}$, in the frequencies are as low as $3.1\,\mu\mathrm{Hz}$. The theoretically expected f-mode frequencies are given by $\omega^2 = gk_h \approx g\ell/R_\odot$, where g is the gravitational acceleration at the surface, k_h is the horizontal component of the wave vector, and $R_\odot$ is the radius of the Sun. We find that the observed frequencies are significantly less than expected for $\ell > 1000$, for which we have no explanation.

Observations of high-degree oscillations, which have very small spatial features, suffer from the effects of atmospheric image blurring and image motion (or "seeing"), thereby reducing the amplitudes of their spatial-frequency components. In an attempt to correct the velocity amplitudes for these effects, we have simultaneously measured the atmospheric modulation transfer function (MTF) by looking at the effects of seeing on the solar limb. We are able to correct the velocity amplitudes using the MTF out to $\ell \approx 1200$. We find that the frequency of the peak velocity power (as a function of ℓ) increases with ℓ. We also find that the mode energy is approximately constant out to $\ell \approx 200$, at which point it begins to decrease. Mode energy is expected to be constant as a function of ℓ if the modes are excited

by stochastic interactions with convective turbulence in the solar convection zone. Finally, we discuss the accuracy of the seeing correction and a test of the correction using the 1989 March 7 partial solar eclipse.

TABLE OF CONTENTS

CHAPTER 1

Introduction

1.1 Historical Overview

The study of solar oscillations promises to uncover a wealth of information about the solar interior. The information presented in this thesis is intended to add to the body of knowledge that has so far been acquired. Solar oscillations are interesting not only as one of the many phenomena visible in the photosphere, but also as a tool for probing the solar interior. Solar oscillations, which are largely vertical motions of the solar atmosphere with periods of roughly five minutes, were discovered by Leighton and co-workers (Leighton, Noyes, and Simon 1962), and were quickly dubbed the solar "five-minute" oscillations. Leighton's observations showed that any given point in the solar photosphere behaves as if a wave packet were passing by, which lasts 6 to 7 cycles and has a peak velocity of $\sim 1\,\mathrm{km/sec}$. Scientifically, the field lay barren for a decade until the oscillations were explained by Ulrich (1970) and independently by Leibacher and Stein (1971) as the superposition of millions of coherent acoustic normal modes oscillating within cavities in the interior of the Sun. Thus, the wave-packet nature of the five-minute oscillations can be explained as a beating effect between modes of nearly identical frequency. The normal modes can be characterized by their frequency ν and degree ℓ, where ℓ is a measure of the spatial frequency of the mode. Higher values of ℓ correspond to higher spatial frequencies, or correspondingly to smaller spatial features. Ando and Osaki (1975) calculated a dispersion relation for the oscillations, which subsequently was observationally confirmed by Deubner (1975) and by Rhodes, Ulrich, and Simon

(1977) for the $200 \lesssim \ell \lesssim 1000$ range. The observations were high-resolution, partial-disk Doppler observations of the photosphere, which when spatially and temporally Fourier-transformed, revealed that the modes fall along distinct ridges in the ℓ-ν plane.

Observational progress continued with the low spatial resolution, high temporal resolution, integrated-sunlight, full-disk Doppler measurements made by Claverie *et al.* (1979) and Grec, Fossat, and Pomerantz (1980), in which the $\ell = 0$, 1, 2, and 3 modes were identified. The individual mode velocity amplitudes were found to be $\sim 20\,\mathrm{cm/sec}$. These modes have also been seen in integrated sunlight brightness measurements (albeit with a much lower signal-to-noise ratio) in which data from the Active Cavity Radiometer Irradiance Monitor (ACRIM) on board the Solar Maximum Mission (SMM) spacecraft were used (Woodard and Hudson 1983). By splitting the solar image into a central disk and an outer annulus and then differencing the Doppler signals, modes with $\ell = 3$, 4, and 5 have been identified (Scherrer *et al.* 1982). The gap between these low-ℓ observations and the earlier high-ℓ observations was finally bridged by Duvall and Harvey (1983, 1984), who used full-disk Doppler and Ca II K brightness images and subjected them to a spatio-temporal decomposition using the theoretical mode eigenfunctions. Their analysis resulted in frequencies for the range $1 \lesssim \ell \lesssim 200$. Note that the list of observations here is not intended to be comprehensive—only those that represent major advances in mode coverage have been listed.

These observations have spawned the field of helioseismology, or the study of the interior of the Sun through the study of its vibrations. This is similar to terrestrial seismology, in which vibrations of the Earth (i.e., earthquakes) are used as probes of its interior. The mode frequencies provide information about the composition and internal structure of the Sun, whereas the amplitudes and linewidths are related to the mechanisms that excite and damp the oscillations. Modes of different degree are used to probe the Sun to different depths. The low-ℓ modes sample the Sun from the surface to nearly the center, whereas the higher-ℓ modes sample only the upper portion of the convection zone. There are two approaches to using the oscillations as probes of the solar interior. The most straightforward method is the so-called "forward problem," in which mode properties are calculated for a given solar model and then compared with the observational properties. Parameters in the solar model are then adjusted so that the calculated properties agree with the observed properties. The other method is the "inverse problem," in which the radial and latitudinal dependence of certain physical quantities in the Sun are deduced through the use of integral equations that use the observed frequencies as inputs. See Unno *et al.* (1989) and Brown, Mihalas, and Rhodes (1986) for reviews of these two methods. Below, we briefly summarize some of the key results of helioseismology.

The most obvious result of the forward-problem approach is the calculation of the mode frequencies and the identification of the modes in the observational data. Other results include adjustments to the helium and heavy-metal abundances, and a new estimate of the depth of the convection zone (see Gough 1983, and Stix 1989 for brief reviews of these topics). Inversions of oscillation frequencies have been used to determine the sound speed as a function of depth (Christensen-Dalsgaard *et al.* 1985; and Christensen-Dalsgaard, Gough, and Thompson 1988). There has been a considerable effort to map the Sun's rate of rotation as a function of depth and latitude using frequency inversions. The main conclusion is that the rotation rate is roughly constant from the surface down to the base of the convection zone with a latitudinal dependence equal to that seen on the surface. A transition to solid-body rotation occurs below the convection zone (Libbrecht 1988d; see also Harvey 1988, and Libbrecht and Morrow 1991 for reviews of this subject). Finally, changes in the mode frequencies as a function of solar cycle have recently been observed by Libbrecht and Woodard (1990). They have measured the frequency shift as a function of ν and have concluded that the mechanisms driving the shift are operating within a few scale heights below the photosphere.

The next major advance in solar oscillation observations is expected to occur when the Global Oscillation Network Group (GONG) project comes on line in 1994.

The GONG project will consist of six sites, located at approximately 60° intervals around the Earth, which will make coordinated Doppler observations of the full solar disk. This network of sites will observe 24 hours per day for three years. Furthermore, there will be partially redundant coverage between sites, so that data gaps produced by bad weather will be avoided. The designers of the GONG project expect a duty cycle of $\gtrsim 93\%$ with an instrument that can see modes out to $\ell \approx 150$ (Harvey, Kennedy, and Leibacher 1987; Harvey *et al.* 1988; Hill *et al.* 1988; and Pintar *et al.* 1988). Beyond GONG lie the solar oscillation instruments that will be carried on the NASA/ESA Solar and Heliospheric Observatory (SOHO) spacecraft (Domingo 1988).

1.2 Overview of Thesis

This thesis deals with some of the observable properties of high-ℓ solar p- and f-modes. We present measurements of the temporal frequencies of the modes, and also the velocity amplitudes of the oscillations. The key difficulty in studying these modes (especially the velocity amplitudes) is the need for high spatial resolution. Unfortunately, the Earth's atmosphere robs us of this needed resolution via what astronomers refer to as "seeing." Atmospheric seeing blurs and distorts high-resolution images of the Sun. As such, we have developed a method for correcting for these effects.

In Chapter 2, we present the needed theoretical background for the understanding of solar oscillations. We discuss the concept of resonant cavities within the Sun, and their associated normal modes. The existence of a mode does not imply that there is any energy in the mode, just as the fact that a tuning fork *can* vibrate at a given frequency does not mean that it *is* vibrating. Accordingly, the most likely mechanisms that can pump energy into and drain energy out of the modes are discussed.

The frequency measurements are covered in Chapter 3. To this end, we describe the principles behind the data-acquisition system that is used to create a time sequence of Dopplergrams, or velocity images, of the Sun. The starting point for most helioseismology studies is the calculation of the oscillation power spectrum (known as a k_h-ω diagram), which we create from the Dopplergrams. Since we are not able to resolve individual modes in this spectrum, we have approximated the mode frequencies using a multi-Gaussian approach. This results in a table of mode frequencies which will extend the measurements described in § 1.1. These high-ℓ frequencies sample the very top of the convection zone, and it is hoped that the physics of this region in the Sun can be better understood through inversions of these frequencies. As an example of an open question, we find a significant difference between the measured and calculated values of the f-mode frequencies. We have no explanation for this discrepancy.

The mode velocity amplitudes are measured using essentially the same technique as that used to measure the frequencies. Chapter 4 covers our velocity amplitude measurements. An earlier attempt by Libbrecht *et al.* (1986) to study the mode velocity amplitudes was inconclusive because of the effects of atmospheric seeing. We repeat their observations and correct for the effects of seeing. Furthermore, we hope to be able to make some statements concerning the mode excitation and damping mechanisms. As mentioned above, seeing artificially reduces the amplitude of the high-ℓ modes. We correct for this effect by measuring the modulation transfer function (MTF) of the atmosphere by looking at the atmosphere-induced blurring of the solar limb. We describe the limb profile data along with our model of the seeing which we have used to create the MTF. The MTF is used to correct the amplitude response of the k_h-ω diagram. The remainder of Chapter 4 is concerned with presenting the corrected amplitude measurements in a useful form. We find that the frequency of the peak velocity power (as a function of ℓ) increases with ℓ. We know of no explanation for this result. The most widely accepted solar oscillation excitation mechanism is that the modes are stochastically excited through interactions with turbulent convection in the solar convection zone. The key idea behind this theory is that the modes share energy with convective eddies.

For $\ell \lesssim 200$, we find that the mode energy is approximately constant. Mode energy is expected to be constant if the modes are in energy equipartition with the eddies.

Finally, in Chapter 5 we address a very difficult subject—the degree to which we have accurately corrected for the effects of atmospheric seeing. We examine this issue from three different points of view. First, we discuss our choice for the model of the seeing and compare it to those used by others. Second, we address any systematic errors that may be introduced by the model used. Last, we describe a test of the seeing measurements using the 1989 March 7 partial solar eclipse.

CHAPTER 2

Theoretical Background

2.1 Introduction

Of all the phenomena visible in the solar photosphere, the five-minute oscillations are one of the most completely understood, and are widely used as tools to probe the interior of the Sun. In this Chapter, we shall review the theory of solar oscillations. The oscillations have been explained as normal-mode, acoustic vibrations in resonant cavities within the Sun. There are two key issues to consider: the frequency spectrum of the oscillations, and the energy (or in terms of observed quantities, the surface velocity) spectrum. We will begin by introducing the equation of motion for the solar plasma. This leads to the concept of resonant cavities and their associated eigenfrequencies. While this model has worked quite well, the quality of the observations has advanced to the point where theorists are using observational data to generate minor refinements to the standard solar model. Given the concept of resonant cavities in the Sun, we next address the question of what mechanism is exciting the normal modes of the cavities. The most likely explanation is that the modes are excited stochastically through interactions with turbulent convection. This model has not yet reached the level of refinement of the former, but it is clear that progress is being made. Throughout this review I have drawn very heavily from three very excellent review articles, the first by Deubner and Gough (1984) for the description of the resonant cavities and their frequencies, the second by Libbrecht (1988c) for the description of the excitation and damping mechanisms (a more technical review can be found in Cox, Chitre, Frandsen, and

Kumar 1991), and finally, the third, by Libbrecht (1988a) which covers both topics. Other very good review articles are referred to as required.

2.2 Propagation Characteristics of Solar Oscillations

Since the oscillations have very small amplitudes, along with very high Q-values, they can be described by a linearized, adiabatic theory. The linearized equations of motion for conservation of momentum, energy, and mass are normally solved numerically for a given solar model. However, in order to gain a better physical understanding of the oscillations, these equations, in a spherical geometry, can be reduced to (Deubner and Gough 1984)

$$\frac{d^2\Psi}{dr^2} + k_r^2\Psi = 0, \tag{2.1}$$

where we have also ignored perturbations in the gravitational potential (the Cowling approximation). Here, $\Psi = \rho^{1/2}c^2\boldsymbol{\nabla}\cdot\boldsymbol{\xi}$, where ρ, c, and $\boldsymbol{\xi}$ are the density, the speed of sound, and the fluid displacement vector, respectively, and k_r is the radial component of the wave vector. The eigenfunctions for the displacement are

$$\begin{aligned}\boldsymbol{\xi}_{n\ell m} = \mathrm{Re}\Bigg\{\Bigg[&R_{n\ell}(r)Y_{\ell m}(\theta,\phi)\mathbf{r}\\ &+\Theta_{n\ell}(r)\left(\frac{\partial Y_{\ell m}(\theta,\phi)}{\partial\theta}\boldsymbol{\theta}+\frac{1}{\sin\theta}\frac{\partial Y_{\ell m}(\theta,\phi)}{\partial\phi}\boldsymbol{\phi}\right)\Bigg]e^{i\omega_{n\ell m}t}\Bigg\},\end{aligned} \tag{2.2}$$

where $Y_{\ell m}(\theta,\phi)$ is a spherical harmonic, $R_{n\ell}(r)$ and $\Theta_{n\ell}(r)$ are the radial and horizontal displacement eigenfunctions, and $\mathbf{r}$, $\boldsymbol{\theta}$, and $\boldsymbol{\phi}$ are unit vectors in spherical coordinates. Perturbations to scalar quantities (such as ρ, p, and T) are given, for example, by

$$\delta\rho_{n\ell m} = \mathrm{Re}\left[\delta\rho_{n\ell}(r)Y_{\ell m}(\theta,\phi)e^{i\omega_{n\ell m}t}\right], \tag{2.3}$$

where $\delta\rho_{n\ell}(r)$ is a radial wave function. In Eqs. (2.2) and (2.3), $\omega_{n\ell m}$ is the angular frequency of the mode, and n, ℓ, and m are integers, where n is the *order* of the mode, ℓ is the *degree* of the mode, and m is the *azimuthal order* of the mode. There are n nodes in the radial direction, $2m$ zeroes in the equatorial direction, and from pole to pole there are $\ell - |m|$ nodes. There are $2\ell + 1$ values of m with $|m| \leq \ell$. Modes with $m = 0$ are called *zonal* modes, and those with $m = \pm\ell$ are called *sectoral* modes. The eigenfunctions described by Eq. (2.2) are somewhat analogous to the wave functions of a hydrogen atom.

The dispersion relation for the radial component of the wave vector, k_r, is given by

$$k_r^2 = \frac{\omega^2 - \omega_c^2}{c^2} + k_h^2 \left(\frac{N^2}{\omega^2} - 1 \right), \tag{2.4}$$

where the acoustic cutoff frequency, ω_c, is defined as

$$\omega_c^2 = \frac{c^2}{4H^2} \left(1 - 2\frac{dH}{dr} \right), \tag{2.5}$$

the horizontal component of the wave vector, k_h, is

$$k_h^2 = \frac{\ell(\ell+1)}{r^2}, \tag{2.6}$$

and the square of the buoyancy (or Brunt-Väisälä) frequency, N, is

$$N^2 = g \left(\frac{1}{H} - \frac{g}{c^2} \right), \tag{2.7}$$

where c is the speed of sound, H is the density scale height, and g is the acceleration due to gravity. The buoyancy frequency is the frequency at which a parcel of gas in a gravitational field will oscillate when displaced from its equilibrium position. When $N^2 < 0$, the gas is unstable in response to small perturbations, and convection results. Note that the dispersion relation is independent of m. This suggests that the oscillation frequencies will be degenerate in m. This also follows from the fact that we are treating the Sun as being spherically symmetric, and hence, there is no preferred orientation of the angular coordinate axes.

If $k_r^2 < 0$, then the oscillations are evanescent and propagation does not occur. If $k_r^2 > 0$, then the oscillations are wavelike and propagation does occur; i.e., energy will be transported. In the latter case, there are two classes of propagating normal modes in the Sun: p-modes in which pressure is the restoring force, and

g-modes in which gravity (or buoyancy) is the restoring force. The p-modes are essentially acoustic vibrations. There is a third class of propagating waves that are not described by the above formalism, namely, the f-modes. These are essentially compressionless surface gravity waves in which $\Psi = 0$. The f-mode dispersion relation is

$$\omega^2 = g k_h. \tag{2.8}$$

In order to further examine the propagation characteristics, we can rewrite Eq. (2.4) as

$$k_r^2 = \frac{\omega^2}{c^2}\left(1 - \frac{\omega_+^2}{\omega^2}\right)\left(1 - \frac{\omega_-^2}{\omega^2}\right), \tag{2.9}$$

where

$$\omega_\pm^2 = \frac{1}{2}\left(S_\ell^2 + \omega_c^2\right) \pm \left[\frac{1}{4}\left(S_\ell^2 + \omega_c^2\right)^2 - N^2 S_\ell^2\right]^{1/2}, \tag{2.10}$$

and where

$$S_\ell = c\frac{\sqrt{\ell(\ell+1)}}{r} = c k_h, \tag{2.11}$$

which is known as the Lamb frequency. As stated before, we must have $k_r^2 > 0$ for propagation to occur. This occurs for either of the following two cases: (a) $\omega^2 > \omega_+^2$ and $\omega^2 > \omega_-^2$, or (b) $\omega^2 < \omega_+^2$ and $\omega^2 < \omega_-^2$. Clearly, these two cases represent high- and low-frequency regimes.

For the high-frequency case (a), Eq. (2.4) reduces to

$$k_r^2 = \frac{\omega^2 - \omega_c^2}{c^2} - k_h^2, \tag{2.12}$$

which is the dispersion relation for acoustic waves in a stratified atmosphere (Leibacher and Stein 1981). This allows us to identify case (a) as being p-modes. We now want to consider how the p-mode propagation characteristics vary with depth. The sound speed increases with temperature as $c \propto T^{1/2}$, and therefore increases as r decreases. Consider an acoustic wave of frequency ω and horizontal wave number k_h that is propagating downward. According to Eq. (2.12), k_r decreases as the wave goes down (since a region of increased sound speed is being entered), and the wave is refracted away from the radial direction. The wave turns around when its horizontal phase speed, ω/k_h, exceeds the local speed of sound. This is essentially a restatement of Snell's Law—a ray is refracted away from the normal when it enters a region of decreasing index of refraction (or increasing phase speed). We see here from Eq. (2.12) that when $\omega < \omega_c$, an acoustic wave will not propagate. The acoustic cutoff frequency ω_c decreases with temperature as $\omega_c \propto T^{-1/2}$, and therefore, increases as r increases. At some point ω_c will increase above the wave frequency ω, and the wave will no longer propagate and will be totally reflected. The acoustic cutoff frequency in the photosphere is $\nu_c \sim 5.5\,\mathrm{mHz}$, and any wave with a frequency higher than this will propagate out of the photosphere and into the chromosphere where its energy may be dissipated into chromospheric heating. These waves will no longer be trapped in the Sun. In summary, p-waves encounter two turning points that define the boundaries of resonant cavities in the Sun. The lower turning point is produced by refraction (caused by a change in the sound speed), and the upper turning point is produced by internal reflection (caused by change in the acoustic cutoff frequency).

For the low-frequency case (b), Eq. (2.4) reduces to

$$k_r^2 = k_h^2 \left(\frac{N^2}{\omega^2} - 1 \right) - \frac{\omega_c^2}{c^2}, \tag{2.13}$$

which is the dispersion relation for gravity waves in a compressible atmosphere (Leibacher and Stein 1981). This permits us to associate case (b) with g-modes. The propagation characteristics for g-modes are slightly different from those for p-modes. From Eq. (2.13), we see that when $\omega > N$, gravity waves will not propagate. This condition holds in the convection zone where N^2 is negative (this is, in fact, the defining characteristic of the convection zone). Therefore, gravity waves will not propagate within the convection zone, and are evanescent in this region because the solar material is buoyantly unstable. The condition $\omega > N$ also holds very near the center of the Sun. In summary, g-waves encounter a turning point at the base of the convection zone, or at $r \approx 0.71 R_\odot$, where $R_\odot$ is the radius of the Sun, and can propagate from this point down to very near the center of the Sun. We shall not go into much more detail concerning g-modes, since this work covers only f- and p-mode oscillations. There are many review articles (in addition to those previously mentioned) that cover g-modes, such as Toomre (1984), Severny and Kotov (1984), Christensen-Dalsgaard (1988a), and Vorontsov and Zharkov (1989).

The above discussion can all be united in a propagation diagram that shows the critical frequencies $\omega_{\pm}$. Fig. 2.1 shows such a propagation diagram for a standard solar model. ω_{+} is plotted as a solid curve for several values of ℓ, and ω_{-} is plotted as a dashed curve. The horizontal lines represent modes: When they are solid, the mode is propagating, and when they are dashed, the mode is evanescent. This picture is very similar to those used to describe quantum mechanical potential well problems. From this picture we see how waves are trapped in the solar interior to form normal modes. The p-modes are trapped between an outer boundary very near the surface of the Sun, and an inner boundary, the location of which is ℓ- and ω-dependent. Furthermore, we see that the low-ℓ modes penetrate deep into the Sun, but not to the core, and the high-ℓ modes all exist just below the photosphere. The g-modes can propagate almost all the way to the center of the Sun, but are reflected at a boundary just below the base of the convection zone.

This leads to a very simple picture of a p-mode as being an acoustic wave trapped in a cavity defined by two concentric spherical surfaces, the outer surface of which is just below the photosphere (see Fig. 2.2). We do not observe the actual propagating wave, but instead, see the evanescent action of the wave in the photosphere. Since g-modes are trapped deep in the Sun, it is very difficult to see their evanescent action in the photosphere, as it has been greatly diminished. The same holds true for the very low-frequency, low-ℓ p-modes (see Fig. 2.1). As a result of this, there is very little observational evidence for these two classes of modes. In the case of the g-modes, this is very unfortunate, since they are the modes that best sample the deep interior of the Sun.

2.3 The p-Mode Frequency Spectrum

Oscillation frequencies $\nu_{n\ell m} = \omega_{n\ell m}/2\pi$ can be estimated from the condition for a normal mode:

$$\int_{r_{\rm in}}^{r_{\rm out}} k_r dr \simeq (n+\epsilon)\pi, \tag{2.14}$$

where $r_{\rm in}$ and $r_{\rm out}$ are the locations of the inner and outer turning points. Basically, this condition states that an integral number (n) of half wavelengths must fit between the boundaries of the cavity. The extra phase factor of $\epsilon\pi$ (where ϵ is of order unity) takes into account the fact that the oscillation amplitudes do not actually go to zero at $r_{\rm in}$ and $r_{\rm out}$, but instead must match the decaying, evanescent solutions outside the cavity.

Using Eq. (2.14), a low-ℓ ($n \gg \ell$), asymptotic expression for $\nu_{n\ell}$ was derived by Vandakurov (1967) and later modified by Tassoul (1980):

$$\nu_{n\ell} \approx \nu_0 \left[n + \frac{1}{2}\left(\ell + \frac{1}{2}\right) + \epsilon_{\rm p}\right] + \delta_{n\ell}, \tag{2.15}$$

where

$$\nu_0 = \left[2\int_0^{R_\odot} \frac{dr}{c}\right]^{-1} \simeq 135\,\mu{\rm Hz}, \tag{2.16}$$

and where

$$\delta_{n\ell} = -\nu_0 \frac{\alpha\ell(\ell+1) - \beta}{n + \frac{1}{2}\ell + \epsilon_{\rm p}}. \tag{2.17}$$

The constant $\epsilon_{\rm p}$ is of order unity and is related to the effective polytropic index near the photosphere. The constants α and β, also both of order unity, are related to the equilibrium structure of the Sun. Note that the oscillation frequencies are approximately evenly spaced in order n for modes of the same degree ℓ. Further note that modes separated by $\Delta n = \mp 1$ and $\Delta\ell = \pm 2$ (i.e., leaving $n + \frac{1}{2}\ell$ unchanged) have approximately the same frequency.

A high-ℓ ($\ell \gg n$) asymptotic expression for $\nu_{n\ell}$ can also be derived from Eq. (2.14) (Deubner and Gough 1984):

$$\nu_{n\ell}^2 \simeq \frac{1}{2\pi^2}(n+\epsilon)Gk_h, \tag{2.18}$$

where $G = -dc^2/dr$ and is of order the solar surface gravity g. For $\ell \gg 1$, and since these modes are trapped just below the photosphere, we can make the approximation

$$k_h \approx \frac{\ell}{R_\odot}, \tag{2.19}$$

and therefore, Eq. (2.18) becomes

$$\nu_{n\ell}^2 \simeq \frac{1}{2\pi^2}(n+\epsilon)G\frac{\ell}{R_\odot}. \tag{2.20}$$

This equation describes parabolas (for constant n) in the ℓ-ν (or k_h-ω) plane as shown in Fig. 2.3 (and also Figs. 3.6 and 3.7). It is the frequencies described by these parabolas that are the subject of Chapter 3.

The m-degeneracy in the oscillation frequencies can be lifted by the application of deviations from spherical symmetry. The most obvious deviation is uniform rotation, which produces a frequency splitting of the form

$$\nu_{n\ell m} = \nu_{n\ell 0} + m\nu_\odot, \tag{2.21}$$

where $\nu_\odot \approx 0.440\,\mu\text{Hz}$ is an average solar rotational frequency. The concept here is analogous to the Zeeman effect in atomic physics in which the application of a magnetic field lifts the degeneracy of the energy levels of an atom. There is a physical explanation for Eq. (2.21) in which we consider two modes $(n, \ell, \pm m)$ in a spherically symmetric Sun. These two modes are traveling in opposite directions (owing to the the $e^{\pm im\phi}$ terms contained in the spherical harmonics $Y_{\ell,\pm m}(\theta,\phi)$). When rotation is included, the two modes are advected past the observer at different rates. The prograde mode (e.g., $+m$) travels faster than normal, and the retrograde mode (e.g., $-m$) travels slower than normal. These changes can be interpreted as changes to the oscillation frequencies. Further deviations from spherical symmetry, such as a latitudinal dependence in the rotation, produce splittings of the form

$$\nu_{n\ell m} = \nu_{n\ell 0} + m\nu_1 + m^3\nu_3 + \cdots. \tag{2.22}$$

Measurements of these deviations are used to measure solar rotation as a function of depth and latitude (Harvey 1988, and other references contained in those proceedings; and Libbrecht and Morrow 1991).

Taking into account the frequencies specified in Eqs. (2.8), (2.15), and (2.20), Eq. (2.21), which describes rotational frequency splitting, and the fact that $\nu_c \sim 5.5\,\mathrm{mHz}$, we find that there are about 10 million modes in the range $0 \leq \ell \leq 3000$, which is a spectrum rich with information about the internal structure of the Sun. Beyond $\ell = 3000$, all modes are above the acoustic cutoff frequency, and therefore propagate out of the photosphere.

2.4 Excitation and Damping Mechanisms

The evidence that the solar five-minute oscillations are trapped acoustic waves is quite compelling. The errors between the calculated frequencies of the oscillations and the measured frequencies are in the 0.5% to 3.0% range (at least for $0 \leq \ell \leq 1000$), with the discrepancies increasing with ℓ and ν (Christensen-Dalsgaard 1990). In fact, the state of the field is now such that the measured frequencies are used to study the internal structure of the Sun (see Stix 1989 for a brief review; see also Brown, Mihalas, and Rhodes 1986). However, the excitation mechanisms that drive the oscillations to their observed amplitudes have yet to be fully explained. There are two main types of excitation mechanisms that have been proposed, namely, overstability mechanisms, and interactions with turbulent convection. There are also other less commonly accepted mechanisms (see Brown, Mihalas, and Rhodes 1986 for a brief review). We shall discuss these two categories of mechanisms in the following paragraphs.

An overstability is a situation in which a perturbation grows with time; i.e., it is a situation of positive feedback. A system driven by an overstability mechanism is said to be self-excited. The overstability mechanism most commonly studied in conjunction with solar oscillations is the κ-mechanism. In the κ-mechanism, the opacity, κ, can be thought of as a "radiation valve" in which a compression-induced increase in κ causes an excess of radiation to be trapped, which further heats the solar plasma. The resulting expansion is greater than the previous cycle of expansion. The κ-mechanism is responsible for the large ($\Delta R/R \sim 0.1$), slow oscillations in Cepheid variables (with periods measured in days) and RR Lyrae stars (with periods measured in hours).

There have been a number of attempts to calculate the stability of p-modes (Ando and Osaki 1975; Goldreich and Keeley 1977a; Christensen-Dalsgaard and Frandsen 1983; Kidman and Cox 1984; and Antia, Chitre, and Narashima 1986). However, the results have been inconclusive, primarily because of the difficulties associated with modeling interactions of the oscillations with radiation and convection. Specifically, if the κ-mechanism were the dominant excitation mechanism, then the driving would occur in the hydrogen ionization zone (which is just below the photosphere), where energy is transported primarily by convection and to a lesser extent, by radiation. The key difficulty lies in calculating the modulation of the convective energy transport processes that is a result of the presence of the acoustic oscillations. Assuming that the solar p-modes are found to be overstable, there must also be a nonlinear damping mechanism operating to limit the growth of the mode amplitudes to finite values.

Kumar and Goldreich (1989) have taken another approach to this problem. They essentially assumed that the p-modes are self-excited by an overstability mechanism, and then they investigated possible damping mechanisms, specifically nonlinear 3-mode coupling. They have explored the implications of these assumptions by comparing them to observations, and have concluded that the modes are not overstable. Their argument has two parts to it, one of which applies to p-modes, and the other of which applies only to f-modes.

For small-amplitude, overstable p-modes, the energy input rate is

$$\frac{dE}{dt} = \alpha E, \tag{2.23}$$

where $\alpha > 0$. In order for the mode energy to remain finite, there must be a nonlinear damping term of the form $-\beta E^2$ (with $\beta > 0$) in the energy growth-rate equation. This would give a steady-state energy of $E = \alpha/\beta$. Kumar and Goldreich have looked at 3-mode coupling, which was thought to be the most efficient method of limiting the energy of overstable solar p-modes, and have found that the energy dissipation rate is

$$\frac{dE}{dt} = -\gamma E, \tag{2.24}$$

where $\gamma > 0$. Therefore, the total rate of change of the p-mode energy is

$$\frac{dE}{dt} = (\alpha - \gamma)E. \tag{2.25}$$

If $\alpha > \gamma$, then the mode energy will grow exponentially, and if $\alpha < \gamma$, the mode energy will decay to zero. Neither of these situations can be the case since we observe the modes to have nonzero, steady-state energy values. If $\alpha = \gamma$, then the mode energy will be constant (as observed), but of an arbitrary value that is not determined by the overstability mechanism. It is, however, very unlikely that the energy input and dissipation rates would exactly cancel in this fashion. Therefore, Kumar and Goldreich conclude that the p-modes are most likely not overstable. It should be noted, however, that there may be some subtle form of nonlinear damping acting on the solar p-modes, which has not yet been investigated.

The f-modes are essentially compressionless waves, and therefore cannot be self-excited by the κ-mechanism. Kumar and Goldreich have considered the possibility that the f-modes receive energy from p-modes via 3-mode couplings, and have found that two competing processes are at work. They have found that two p-modes will couple with an f-mode to transfer energy into the f-mode. On the other hand, an f-mode will couple with either an f- or a p-mode and a propagating wave to remove energy from the f-mode. (A propagating wave, here, refers to a wave with a frequency higher than the acoustic cutoff frequency, which will, therefore, propagate out of the solar atmosphere. Such a wave removes energy from the atmosphere.) The net outcome is that the resulting f-mode energy is several orders of magnitude less than the energy of a p-mode of similar frequency. Since f-modes are observed to have roughly the same energy as p-modes with comparable frequencies (see Chapter 4), there must be some other excitation mechanism driving the f-modes. It is possible that an overstability mechanism (other than the κ-mechanism) is driving the f-modes, but there are none that satisfy the above argument regarding overstability of p-modes. As a result, Kumar and Goldreich find that it is not unreasonable to assume that the mechanism that excites the p-modes also excites the f-modes.

The other leading contender for the mode excitation mechanism is that the modes are stochastically excited by interactions with turbulent convection, the details of which were first worked out by Goldreich and Keeley (1977b) and later refined by Goldreich and Kumar (1988, 1990). The basic idea here is that turbulence in the convective zone generates acoustic noise. Some of this acoustic energy is then transferred into the acoustic modes. The concept is similar to what happens when one feeds a microwave cavity with a broad-band frequency spectrum of electromagnetic radiation — the cavity resonates at its resonant frequencies. Of course, with the Sun, the details are much more complicated.

Acoustic noise is generated by turbulence via the Lighthill mechanism (Lighthill 1952; see also Stein and Leibacher 1981 for a very simple explanation). There are two types of turbulence discussed in the Goldreich/Keeley/Kumar papers: free turbulence, which is turbulence in the absence of any external forces, and forced turbulence, which is turbulence in the presence of an external driving force, such as gravity. Lighthill found that the dominant emission process for homogeneous, free turbulence is quadrupolar in nature. The resulting acoustic power is proportional to M^8 where M is the Mach number of the turbulence. One sees, right away, that the power radiated by turbulence is highly sensitive to the turbulence model. Any lack of understanding of the turbulence (of which there are many) is greatly amplified when calculating the acoustic noise generated by the turbulence. It should be noted that the mechanism at work here is similar to that which is responsible for noise from jet aircraft engines. (However, I have yet to personally test this theory! ✈)

Goldreich and Keeley (1977b) considered not only the emission of acoustic noise by turbulence, but also the absorption of acoustic noise by turbulence. They considered quadrupole emission and absorption terms and found that the modes were in energy equipartition with resonant, convective eddies; i.e., the energy in a mode, E, is approximately the same as the kinetic energy in a convective eddy that has a turnover time equal to the period of the mode:

$$E \approx mv^2, \tag{2.26}$$

where m is the mass of the eddy, and v is the characteristic velocity of the turbulence. They related the eddy size to the scale height, H, and used $m \sim \rho H^3$. Eq. (2.26) can be related to the observed photospheric mode velocities by introducing a quantity, M_v, referred to as the mode mass (Goldreich and Keeley 1977b), which can best be thought of as that quantity of mass which, when moving with the surface velocity of a given mode, has the same energy as the energy in the mode. Then the energy of a mode is given by

$$E = M_v P_v, \tag{2.27}$$

where P_v is the observed surface velocity power. Given this basis of comparison, Eq. (2.26) underestimates the observed mode energies by several orders of magnitude.

Goldreich and Kumar (1988) have since refined this work and considered the effects of gravity on acoustic emission and absorption, and found that the dominant emission term is dipolar, whereas the dominant absorption term is still a quadrupole. It should be noted that their model consists of turbulence in a box, which bears little resemblance to the actual Sun. They find that for homogeneous, gravity-driven turbulence in a box, the energy in a mode is increased by a factor of M^{-2} so that

$$E \approx mc^2, \tag{2.28}$$

where they now associate the convective eddies with granulation cells. Note that the granulation-cell turnover times are of order five minutes, which is just right for driving the five-minute oscillations. Also note that the spread in granulation cell turnover times nicely accounts for the fact that the 10 million different modes all have approximately the same energy (see Chapter 4), and are simultaneously excited. Libbrecht (1988a) shows, as follows, that Eq (2.28) is in rough agreement with the low-ℓ observations (Libbrecht 1988b). The energy in a convective eddy is simply

$$E \approx \rho H L^2 c^2, \tag{2.29}$$

where $\rho \approx 10^{-7}\,\mathrm{gm/cm^3}$ is the density at $\tau_{5000} = 1$, $H \approx 100\,\mathrm{km}$ is the scale height, $L \approx 1000\,\mathrm{km}$ is the horizontal size of a granulation cell, and $c \approx 10\,\mathrm{km/sec}$. This gives $E \sim 10^{28}$ ergs which is, as stated, in rough agreement with the low-ℓ observations.

Recently, Goldreich and Kumar (1990) have further modified their theory by introducing a density gradient in their turbulent fluid, thereby better approximating actual conditions in the Sun. They now find that monopole emission is also a significant factor. This has the effect of canceling out the dipole emission of the previous model, thereby reducing the mode energy by a factor of M^2, which, once again, gives a mode energy given by Eq. (2.26). However, in this case, we still associate the convective eddies with granulation cells. Since $M \sim 0.3$ just below the photosphere, the mode energy is reduced by a factor of ~ 10, giving $E \sim 10^{27}$ ergs. This is in rough agreement with the higher-ℓ observations (see Chapter 4).

At any rate, it appears most likely that the modes are stochastically excited by interactions with turbulent convection. This mechanism has the advantage in that it explains the observed f- and p-mode energies to "astrophysical accuracy." It is also apparent that further work is needed to fully determine the excitation and damping mechanisms.

Figure Captions

Figure 2.1: A propagation diagram for a standard solar model. Solid curves represent $\omega_+/2\pi$, and dashed curves represent $\omega_-/2\pi$ in the regions where the critical frequencies are real. The lower horizontal axis scale extends out to $r/R_\odot = 0.9995$; beyond that value, the scale is expanded by a factor of 100, and is indicated on the upper horizontal axis, where h is the height above the photosphere. The curves $\omega_\pm$ are for $\ell = 1,\ 5,\ 50$, and 100. In all cases, $\omega_\pm$ are increasing functions of ℓ at fixed $r/R_\odot$, which permits the identification of the curves. In the interior, the ω_- curves for $\ell = 5,\ 50$, and 500 are essentially indistinguishable, as are all four ω_+ curves in the atmosphere, where $\omega \approx \omega_c$. The thin horizontal lines represent normal modes; they are continuous in zones of propagation and dashed in the evanescent regions. This picture is very similar to those used to describe quantum mechanical potential well problems. The lowest-frequency mode is an $\ell \gtrsim 25$ g-mode. Its amplitude is likely to be substantial in either the interior or the atmosphere, but not both. The next line represents an $\ell = 1$ g_1-mode (where the subscript is the radial order n of the mode), which has the character of a p-mode in its outer zone of propagation. The third line is an $\ell = 5$ p_4-mode, which is a simple p-mode confined to a single region of propagation. The highest-frequency line is an $\ell = 500$ p_6-mode; because the evanescent regions are thin, this mode could have a substantial amplitude in both the photosphere and the chromosphere. (From Deubner and Gough 1984).

Figure 2.2: A ray diagram for acoustic waves trapped in the solar interior. The circle represents the solar surface, and rays for standing waves for different values of ℓ are plotted. This diagram shows schematically that lower ℓ modes penetrate deeper into the solar interior, and that the wave vector (and also the fluid displacement) is predominantly vertical at the surface. (From Libbrecht 1988a, which was adapted from Toomre 1986).

Figure 2.3: A schematic ℓ-ν diagram showing the loci of p-mode frequencies determined from a theoretical solar model. The different lines (or "ridges") are for

different values of the radial order n, and are labeled on the right side of the diagram.

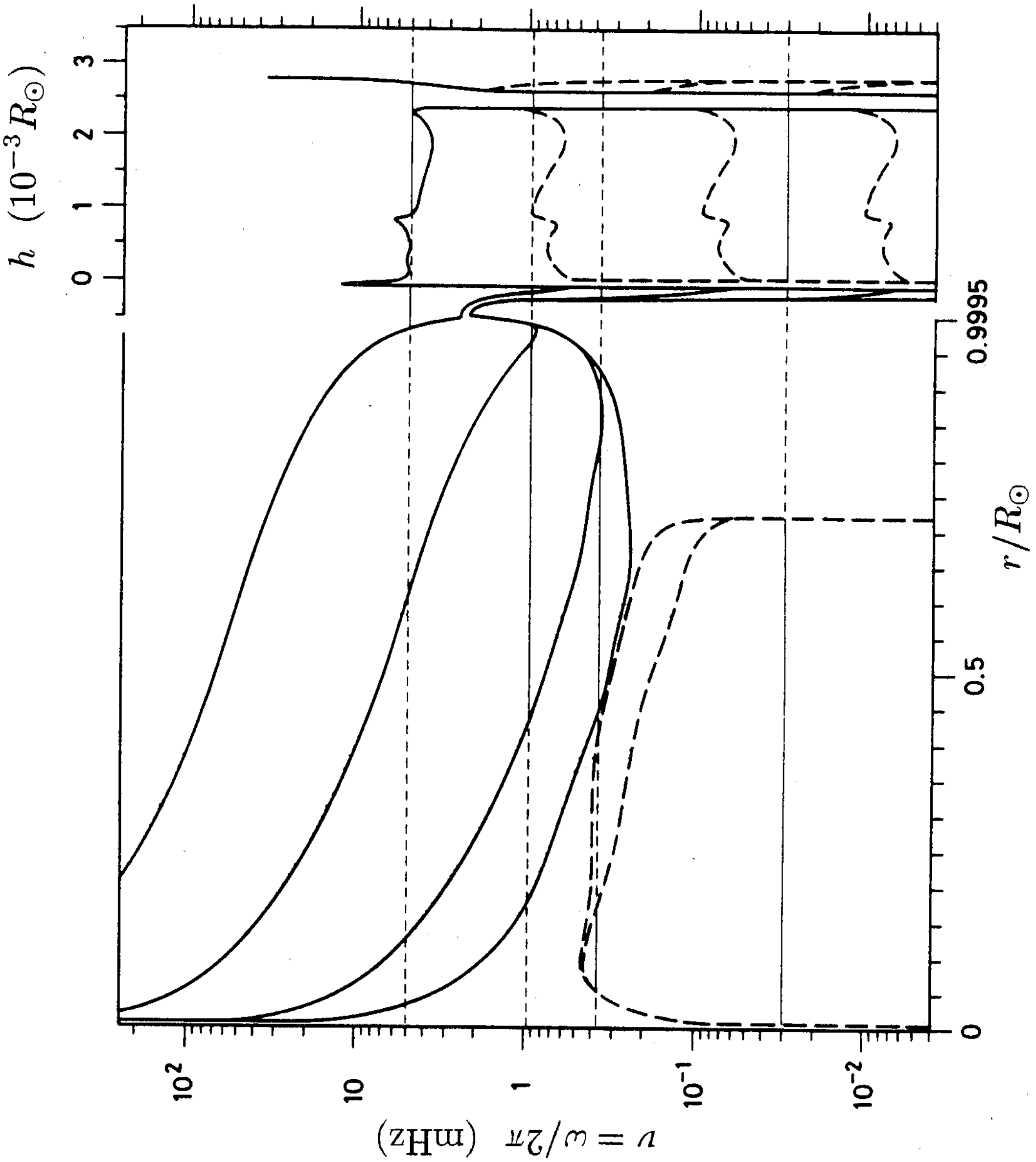

h $(10^{-3}R_\odot)$
0
1
2
3
0.9995
0.5
0
$r/R_\odot$
10^2
10
1
10^{-1}
10^{-2}
$\nu = \omega/2\pi$ (mHz)

Fig. 2.1

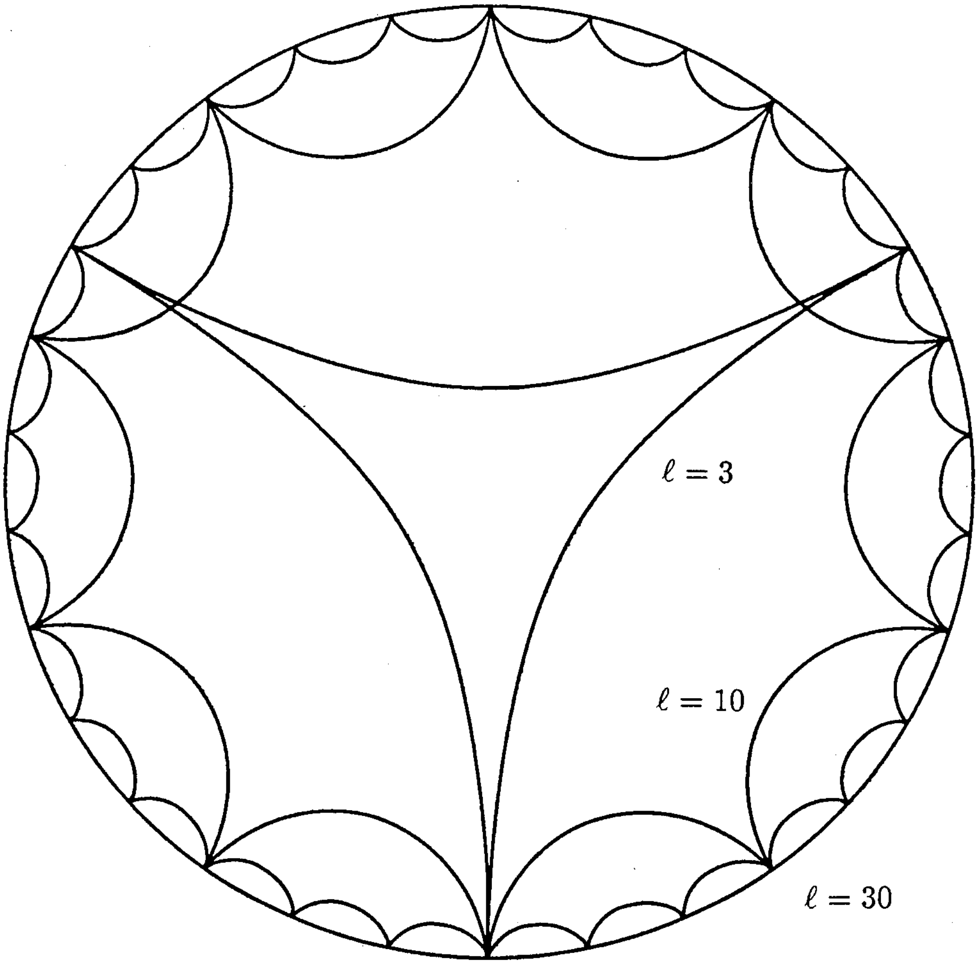

Fig. 2.2

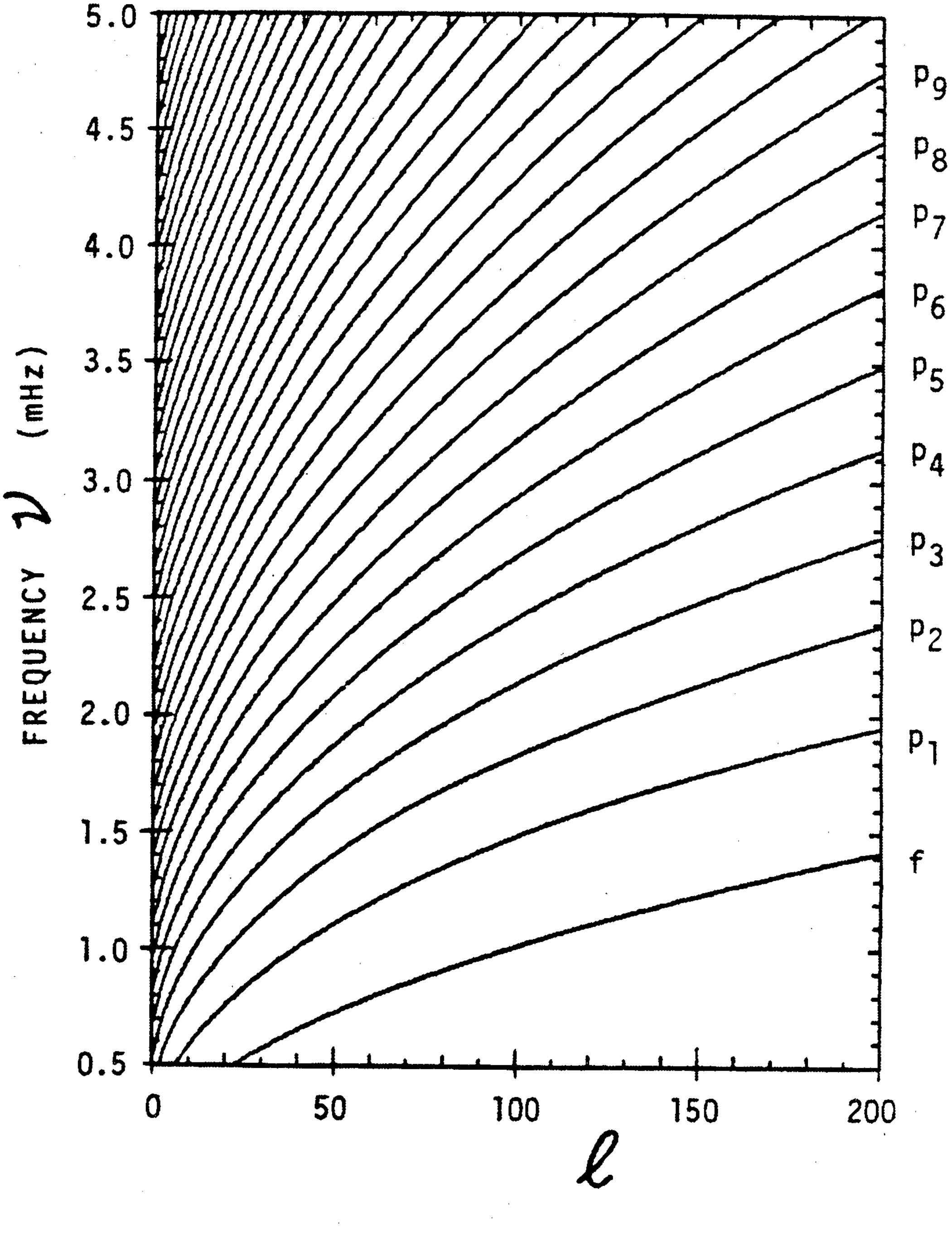
FREQUENCY ν (mHz)
5.0
4.5
4.0
3.5
3.0
2.5
2.0
1.5
1.0
0.5
0
50
100
150
200
ℓ
p_9
p_8
p_7
p_6
p_5
p_4
p_3
p_2
p_1
f

Fig. 2.3

CHAPTER 3

Frequency Measurements

3.1 Introduction

The solar normal mode frequencies, $\nu_{n\ell}$, as a function of degree, ℓ (averaged over azimuthal order, m), and radial order, n, are particularly useful in modeling the radial structure of the Sun, since the agreement between the measured and calculated mode frequencies can be used to test solar models. Without the normal mode spectrum, one would have to be satisfied with reproducing little more than the observed solar radius and luminosity, given the Sun's mass, age, and chemical composition—not a good situation, given the uncertainties in the solar helium abundance and our lack of understanding of the physics of convection. Furthermore, because different solar oscillation modes penetrate the solar interior to different depths, it is possible, with an accurate set of mode frequencies, to invert the data to determine the internal sound speed as a function of radius (Christensen-Dalsgaard *et al.* 1985; Christensen-Dalsgaard 1988b; Shibahashi and Sekii 1988; and Vorontsov 1988). From this, one would hope that a better understanding of the physics of the solar interior would ensue.

Much work has been done in measuring the frequencies of low- and intermediate-ℓ modes (see, for example, Duvall and Harvey 1983, 1984; Grec, Fossat, and Pomerantz 1983; Woodard and Hudson 1983; Henning and Scherrer 1986; Libbrecht and Zirin 1986; Duvall *et al.* 1988; and Jiménez *et al.* 1988), as these modes sample the greatest range in solar depths. At first glance, it would seem that high-ℓ ($\ell \gtrsim 150$)

modes are not as useful for inversion purposes since they are confined to the upper 1–2% of the solar interior. However, the pressure is rapidly varying in this depth range, and as a result, the high-ℓ modes sample a large range of pressure values, and are, therefore, also useful for understanding the structure of the convection zone. Unfortunately, not much work has been done in this area of measuring the frequencies of high-ℓ modes. The work that does exist typically uses data with very low signal-to-noise ratios. Also, when data with good signal-to-noise ratios exist, very little effort has been made to accurately measure the mode frequencies (Kneer, Newkirk, Jr., and von Uexküll 1982; Deubner 1983; Gouttebroze, Damé, and Malherbe 1984; Nishikawa *et al.* 1986; and Hill 1988).

With this in mind, we have undertaken to produce a new set of high-degree solar oscillation mode frequencies, with as high an accuracy as possible, and covering the greatest range in ℓ and ν possible; our results are presented in Table 3.2. This table, using new and better data, covers higher values of ℓ and a greater range in ν, plus frequency uncertainties and systematic errors that are considerably smaller than those quoted in previous papers. Much of the work in this chapter is based on, and is an extension of, work presented by Libbrecht, Woodard, and Kaufman (1990).

3.2 Overview of Data Analysis

A helioseismology data set usually consists of a time series of intensity or velocity images of the Sun, with sample intervals of about one minute and lengths ranging from one day to several months. In this work, we have used velocity images, or Dopplergrams, which are produced by differencing images made in the red and blue wings of a solar absorption line. Here we shall briefly describe the techniques used for modal decomposition of a time series of Dopplergrams. We will later expand upon this description of the analysis.

A standard practice used for identifying individual solar normal modes is to fit a time series of solar velocity images to projected spherical harmonics with a range of ℓ and m, and then Fourier-transform the time series of fit coefficients. The resulting power spectra, $S_{\ell m}(\nu)$, show a number of sharp features that are due to solar p- and f-modes, and these power spectra are further analyzed to determine the solar oscillation frequencies. Another standard technique commonly employed to increase the signal-to-noise ratio is to average the power spectra over all m for a fixed ℓ, forming averaged power spectra, $S_{\ell}(\nu)$, after first displacing the individual $S_{\ell m}(\nu)$ spectra to remove the effects of rotational splitting. The resulting peaks in the averaged power spectra are then analyzed to determine the frequencies of the p- and f-modes at fixed ℓ and n, which approximate what one would find if the Sun were spherically symmetric and nonrotating. With this brief description of the modal decomposition of solar oscillation data, we begin the discussion of the particular analysis used on the current data.

3.3 Instrumentation and Data Acquisition

Solar oscillations, which are essentially mechanical vibrations of the Sun, are typically observed using one of two techniques. The first is to look at the resulting intensity changes that are due to compressions and rarefactions of the solar atmosphere. The second method is to look at the motion of the solar photosphere using an absorption line that has been Doppler-shifted by the oscillations. The latter method, while instrumentally more complicated, is capable of producing data with a much higher signal-to-noise ratio than the former technique. The velocity of the solar photosphere at a given point can be measured by sampling the red and blue wings of an absorption line. The difference in these two quantities is proportional to the velocity of the absorbing medium at that point. Velocity images, or Dopplergrams, of the photosphere were first made by Leighton (Leighton 1959; and Leighton, Noyes, and Simon 1962), and are produced by making images of the Sun in the red and blue wings of an absorption line, and then subtracting the two images. This technique necessitates the use of a very narrow bandpass ($\lesssim 0.25$Å) imaging filter so that light from only one wing of the line can be seen. Several different types of filters meeting this requirement are currently in use in solar astronomy. In this work we have used a birefringent, or Lyot, filter (Lyot 1933). In essence, the birefringent filter works by passing linearly polarized light through a birefringent crystal (usually quartz or calcite). The birefringence produces a wavelength-dependent phase shift, and hence, a wavelength-dependent rotation of the input polarization vector. The resulting transmission profile, T, after passing through an analyzing polarizer, is

$$T = \cos^2\left(\frac{\pi d\epsilon}{\lambda}\right), \tag{3.1}$$

where d is the thickness of the crystal, and ϵ is the difference between the fast and slow indices of refraction of the crystal. Peaks in the transmission profile are given by $n\lambda_0 = d\epsilon$, where n is an integer. If we let $\Delta\lambda = \lambda - \lambda_0 \ll \lambda_0$, then the transmission profile can be approximated by

$$T = \cos^2\left(\frac{\pi\Delta\lambda}{\lambda_0}\right). \tag{3.2}$$

The important point here is that there are approximately equally spaced maxima in the transmission profile. One can vary the spacing between maxima by varying the length and/or properties of the birefringent crystal. By combining several stages of the crystal/polarizer elements (with appropriately chosen spacing between transmission maxima), one can create a filter with a bandpass of ~ 0.25Å or smaller. The birefringent filter is described in more detail by Evans (1949).

By varying the orientation of the polarization vector of the initial polarized light to the filter by ±90°, the center of the filter bandpass can be shifted by $\pm 1/2$ of the bandpass. This can be accomplished by either mechanically rotating a polarizer, or by electrically chopping an electro-optic crystal. The latter technique was used for these observations, and employed a polarizer and $\lambda/4$ plate (creating a circular polarizer), and a KD*P crystal. The circular polarizer sends circularly polarized light into the KD*P crystal. The voltage applied to the crystal is chopped by an amount such that the crystal produces $\pm\pi/4$ of retardation. This results in an output consisting of linearly polarized light, the two states of which are perpendicular to each other, and which can serve as inputs to the filter. This technique is described in more detail by Mosher (1976). It should be noted that the filter described here is an idealization of the actual filter. The actual filter is somewhat more complicated in design and requires other optical elements to function properly as a Doppler analyzer. It should also be noted that with minor modifications, the techniques described above are commonly used to measure solar magnetic fields.

All data described here were collected in 1987 and 1988 at Big Bear Solar Observatory (BBSO) using the BBSO videomagnetograph (VMG) system configured for Doppler measurements (Zirin 1985). The 6439 Å Ca line was used for all measurements. The typical optical setup used for these observations is shown schematically in Fig. 3.1. The output of the telescope was sent through several ancillary filters (typically neutral density and heat absorbing filters), and an interference prefilter with a bandpass of ~ 20 Å. The beam then passed through a "wavelength selector," consisting of a linear polarizer, a $\lambda/4$ plate (these two elements forming a circular polarizer), and an Inrad KD*P electro-optic crystal. A field lens was used to make the beam more collimated as it passed through a Zeiss 0.25 Å birefringent filter, originally designed for use at H_α, which has been modified for use at 6439 Å. The filter output was re-imaged onto a COHU 4810 CCD camera with a standard RS-170 video output.

The data acquisition system is shown schematically in Fig. 3.2. A PDP 11/44 microcomputer controlled the acquisition of data. Images were taken at video rates (30 images/sec) and were digitized into eight-bit 512 × 481 pixel images using a Quantex DS-20 image processor. For technical reasons, the usable part of the image was slightly smaller than this. Under computer control, a red image was acquired and stored in the 12-bit memory of the Quantex. After switching the voltage on the KD*P crystal, a blue image was acquired and subsequently digitally subtracted from the stored red image, resulting in a velocity-proportional image. This process was repeated 96 times, each time adding the resulting red/blue pair to the Quantex memory. This entire procedure resulted in a Dopplergram, consisting of integrated red/blue pairs, that took slightly less than 10 seconds to create. Dopplergrams were collected at the rate of one per minute. Each Dopplergram was written to magnetic tape, and was also displayed on a video monitor. The video monitor was then photographed by a Mitchell 35mm motion picture camera operated in single frame mode by the computer. This resulted in a movie of the velocity data, which, quantitatively, was not of much value, but was very useful for debugging purposes. It should be noted that the VMG system (configured for Doppler measurements) operates in much the same fashion as the data acquisition system on the BBSO dedicated helioseismology telescope described by Libbrecht and Zirin (1986).

3.4 Description of Data

As mentioned above, data were collected at BBSO for a few weeks in the summers of 1987 and 1988. In the end, only one day from each year was analyzed as all of the remaining days suffered from problems (e.g., equipment failures, clouds, poor seeing, etc.). Each data set consists of a time series of Dopplergrams, taken at a rate of one per minute, of the center portion of the solar disk. Since different telescopes were used for each of these observing campaigns, most of the relevant parameters describing the two data sets are different. Table 3.1 shows these parameters; however, the primary difference between the two data sets is that the 1988 set has approximately twice the spatial resolution of the 1987 set. These data sets were originally made for the purpose of measuring velocity power as a function of ℓ at high ℓ (Kaufman 1988, and Chapter 4). Such measurements are easily affected by atmospheric seeing. To correct for this effect, the telescope was moved from the center disk to the limb, at approximately 15-minute intervals, and a series of short-exposure limb profiles were acquired. This was accomplished without interrupting the collection of Doppler images. Atmospheric seeing was then quantitatively determined from smearing of the limb profile. For the purposes of the frequency measurements described in this chapter, no correction for the effects of seeing has been made. Fig. 3.3 shows a typical Dopplergram.

Since the Dopplergrams are only partial disk images and the solar limb is not visible, we have no direct way of accurately determining the image scale from the

Table 3.1

Observational Parameters

Date	1987 July 23	1988 July 19
Time (UT)	14:45–00:59	14:18–20:28
No. of images	616	372
Telescope	25 cm (10 in) refractor	66 cm (26 in) reflector
Image size	$267'' \times 197''$	$136'' \times 100''$
No. of pixels	498×460	498×460
Horizontal image scale, S_H	$0.536''$/pixel	$0.273''$/pixel
$R_\odot$	$945.94''$	$944.30''$
Preliminary scale factor, $d\ell/dk$	21.66	42.92
Qualitative seeing	fair	good

data itself. However, approximate image scale information was collected during the observing runs by making two images of a sunspot, with the telescope moved a known amount between the two images. These two images were later digitally superimposed using an image processing system that has the capability of sliding one image across the other. In this way, the pixel shift between the two images was measured, and hence, the approximate image scale was determined. The horizontal image scales for the 1987 and 1988 data sets are given in Table 3.1. Since the CCD camera used to acquire data has pixels with differing horizontal and vertical dimensions, and since the camera output is in video format (with its associated aspect ratio of 4/3), the horizontal and vertical image scales are different. However, given one image scale, it is easy to find the other, since

$$S_V = \frac{3}{4}\frac{512}{481} S_H, \tag{3.3}$$

where S_V and S_H are the vertical and horizontal image scales. In Table 3.1, we also present preliminary values for the scale factor (see § 3.7),

$$d\ell/dk = \frac{2\pi R_\odot}{512 S_H}, \tag{3.4}$$

where $R_\odot$ is the solar radius. The scale factor is expressed in terms of the horizontal image scale, since vertical distances will later be expressed in terms of S_H.

3.5 Preliminary Data Analysis

The time series of Dopplergrams were not perfect—there were occasional gaps or bad images. The gaps were typically produced by computer failures, and the bad images were typically due to a cloud passing in front of the field of view, or the telescope being bumped by one of the operators. Locating missing images in the time sequence was a trivial task. Bad images were located, first by collapsing each image onto a line, and then fitting a straight line to each image. The resulting fit coefficients were then plotted as a function of image number (or time). Bad images appeared as spikes in the plot. If the duration of the bad segments in the time series was excessive ($\gtrsim$ 30 minutes, or about 5% of a day's worth of data), that data set was deemed unusable. In the remaining data sets, the bad or missing images were replaced with linear interpolations using the the two endpoint images that surround the gap.

The birefringent filter used to produce the Dopplergrams suffers from spatial nonuniformity across the field of view. This is for numerous reasons, such as the difficulty in producing birefringent blocks of quartz and calcite with perfectly plane-parallel faces, temperature gradients in the filter (which change the lengths of the optical elements), and the inherent feature that the filter bandpass is different for axial and nonaxial rays. A rough attempt at correcting for the filter nonuniformities was made by subtracting a best-fit planar background from each image. This later turned out to introduce more problems than it solved, as will be seen in Chapter 4. However, this correction had no effect on the frequency measurements described in this chapter.

3.6 The k_h-ω Diagram

Carrying out the above operations results in a "perfect" data set which can then be decomposed into component modes. A 512 × 512 point, two-dimensional spatial Fourier transform was performed on each image, thereby turning the data set into a k_x-k_y-t diagram. The Fourier transform is equivalent to making a plane-wave approximation to the spherical harmonics (Hill 1988). Since each image was slightly smaller than 512 × 512 points, the array to be transformed was padded with zeroes. For each time series of spatial-frequency components, a best-fit linear background was subtracted. Temporal Fourier transforms (using 1024 points for 1987 and 512 points for 1988, with appropriate zero padding as required) were then done, resulting in a k_x-k_y-ω diagram. This entire procedure is schematically illustrated in Fig. 3.4. At this point, the k_x-k_y-ω diagram is in general complex, and contains the amplitude spectral density of the oscillations. However, we are primarily interested in the power spectral density (PSD), so we next calculated the squared magnitude of the k_x-k_y-ω diagram to get the PSD. We shall normally refer to the PSD as the power spectrum. Accomplishing this 3-D Fourier transform was not a trivial task, because of the large amounts of data and the limited amounts of computer memory and disk space. At one step in the computation, the 1987 data set required upwards of 130 Mbytes of storage. This storage requirement necessitated that the data set be broken up into more manageable chunks, thus increasing the complexity of the computation and the associated bookkeeping tasks.

The mode structure of the oscillations, as seen in k_x-k_y-ω space, takes on the form of concentric, slightly nonaxisymmetric surfaces, which Hill (1988) refers to as "trumpets." Solar rotation is responsible for the nonaxisymmetric aspects of the surfaces. These surfaces are depicted schematically in Fig. 3.5, which is taken from Hill (1988). Peri (1988) prefers a more colorful description for these surfaces and compares them to calla lillies. The approximate relationships between k_x and k_y and the mode indices, ℓ and m, are $k_x \approx m/R_\odot$ and $k_y \approx \sqrt{\ell^2 - m^2}/R_\odot$. From this, one sees that the $k_y = 0$ plane corresponds to sectoral modes ($\ell = \pm m$), and that the surfaces are symmetric about the $k_y = 0$ plane. See Hill (1988) for a further explanation of this procedure.

We then corrected for frequency shifts produced by solar rotation (Eq. 2.21) using a value of $\nu_\odot = 0.475\ \mu$Hz. This correction was an approximate one and is the result of trial and error with different values of $\nu_\odot$. The optimal value of $\nu_\odot$ was selected by correcting the frequency shifts in only the sectoral modes (the $k_y = 0$ plane), and then folding this plane along the ω axis. This latter operation amounts to adding the spectral amplitudes of the prograde and retrograde components of the sectoral oscillations. When good alignment was observed between the prograde and retrograde modes, the optimal value of $\nu_\odot$ was found. Note that our value of $\nu_\odot$ differs from the commonly accepted value of 0.440 μHz. We believe that this discrepancy is due to a slow, flexure-induced drift of the telescope over the course of the observations. In essence, if the telescope is made to point at the center of the solar *disk*, then the solar *surface* will appear to move slowly past the field of view because of solar rotation. Flexure-induced image motion will appear as a similar drift and will therefore modify the measured value of $\nu_\odot$. In summary, this discrepancy is not cause for concern.

After the corrections for rotational effects have been completed, the surfaces in the k_x-k_y-ω diagram (trumpets) are axisymmetric and can be described as figures of revolution about the ω-axis. These figures of revolution can now be collapsed upon themselves by integrating along circles of constant

$$k_h = \sqrt{k_x^2 + k_y^2} = \sqrt{\ell(\ell+1)}/R_\odot \tag{3.5}$$

(taking into account the different horizontal and vertical image scales), thereby producing averaged power spectra, $S_k(\nu)$, where k is an integer index corresponding to the spectral components in the spatial Fourier transform. This procedure is equivalent to the procedure of azimuthally averaging the rotationally corrected $S_{\ell m}(\nu)$ spectra to get averaged power spectra, $S_\ell(\nu)$. Collectively, the $S_k(\nu)$ form a k_h-ω (or ℓ-ν) diagram. Fig. 3.6 shows the k_h-ω diagram for the 1987 data set.

Ridges (corresponding to radial eigenfunctions with constant n) can be seen out to $\ell \sim 1800$. The k_h-ω diagram for the 1988 data set is shown in Fig. 3.7. Qualitatively (and quantitatively, as shall be seen in Chapter 4), the seeing was better for the 1988 observing run (see Table 3.1); and, as a result, the amplitude degradation of higher spatial frequency features, e.g., higher-ℓ modes, is less. Consequently, ridges in the 1988 data can be seen out to slightly higher ℓ, i.e., out to $\ell \sim 1900$. Also, note that since the 1988 time series is half as long as the 1987 time series, the temporal frequency resolution for 1988 is twice as large as the 1987 resolution.

3.7 Frequency Measurements: Ridge Fitting and Systematic Errors

At high ℓ, say for $\ell \gtrsim 250$ (the value here is not very well known), the mode linewidth is greater than $\partial\nu_{n\ell}/\partial\ell$, and therefore it is impossible to resolve individual multiplets. Indeed, at this point the oscillations will no longer be true global modes. In principle one could make a detailed model of the data to determine a mean multiplet frequency, although the large widths of the spectral peaks for this range of ℓ make accurate frequency determinations more difficult. We have chosen here a somewhat simpler and quicker analysis—namely, fitting the constant-n features in the averaged power spectra (the ridges) to Gaussian functions of ν, then using the centroid of the Gaussian to estimate the ridge frequency at fixed ℓ. This Gaussian "ridge-fitting" technique was first exploited by Libbrecht and Kaufman (1988).

Mode frequencies were estimated by fitting the power spectra, $S_k(\nu)$, to a series of Gaussians

$$S_k(\nu) \rightarrow \sum_{i=1}^{N} A_i e^{-(\nu-\nu_i)^2/\sigma_i^2} + A_B e^{-(\nu-\nu_B)^2/\sigma_B^2} + C, \tag{3.6}$$

where ν_i is the frequency of the ith ridge, the subscript B refers to a wide background Gaussian, and C is a constant background offset. The necessity for including the two background terms will become more apparent below. These terms will also be needed to accomplish the velocity power measurements described in Chapter 4. The nonlinear, least-squares fits were accomplished using the Levenberg-Marquardt method described in Press *et al.* (1986), and were made over the range

$\nu_{\min} = 1.5\,\mathrm{mHz}$ to $\nu_{\max} = 5.5\,\mathrm{mHz}$. Initial guesses for the ν_i came from Libbrecht and Kaufman (1988) where available, and were hand-identified from plots of the $S_k(\nu)$ when no tabulated values were available. A first attempt at fitting the above equation to $S_k(\nu)$ for 1987 gave adequate results except where the frequency of the background Gaussian was within ≈ 300 μHz of the frequency of the f ridge. This occurred for $\ell \gtrsim 1100$, and for these spectra the f-mode frequency and width were sufficiently close to the background frequency and width to prevent the fitting algorithm from converging on appropriate values for the f-mode and background amplitudes. In Fig. 3.8 one can see that for $k \gtrsim 54$ ($\ell \gtrsim 1100$), ν_B, σ_B, and A_B no longer vary smoothly because of the fit convergence problems. The background offset, C, appears not to have been affected by this problem. Below $\ell \approx 1100$, the fitting algorithm was well behaved and we determined that both ν_B and σ_B varied approximately linearly with ℓ (see Fig. 3.8). This fact was exploited by re-doing the fits to Eq. (3.6) with ν_B and σ_B no longer free parameters. We used $\nu_B = 3126 + 8.55k$ μHz and $\sigma_B = 648 + 5.58k$ μHz. Similar results were found for the 1988 data. Fig. 3.9 shows the new background fit parameters; the background Gaussian amplitude, A_B, now behaves more sensibly above $k \gtrsim 54$. Fixing ν_B and σ_B also allowed the fitting algorithm to converge to sensible values of the f-mode amplitude, A_f. Below $\ell = \ell_{\min}$ (or $k = k_{\min}$) the Gaussian model of the power spectra breaks down because individual ridges can no longer be resolved. For the 1987 data, $\ell_{\min} \approx 170$, and the breakdown occurs at $\ell_{\min} \approx 340$ for the shorter duration 1988 data. Above $\ell = \ell_{\max}$ (or $k = k_{\max}$) the signal-to-noise ratio has decreased to the point where ridges can no longer identified. For the 1987 data $\ell_{\max} \approx 1880$, and for the 1988 data (which were acquired under conditions with better seeing) $\ell_{\max} \approx 1930$. Typical power spectra and their fits are shown in Fig. 3.10. Typically, the σ_i were found to be about $60 - 200$ μHz, and are certainly not indicative of the intrinsic mode linewidths, at least in the regions of the ℓ-ν plane where others have measured linewidths (e.g., see Libbrecht 1988b). Fig. 3.11 shows the raw ν_i in a schematic ℓ-ν diagram with error bars given by the ridge widths, σ_i. Note that in the $k = 80$ ($\ell \approx 1683$) spectrum in Fig. 3.10, the Gaussian component of the background noise is clearly visible, and appears as a shoulder on the low-frequency side of the $n = 0$ ridge. As shown in Fig. 3.12a, for $\ell \lesssim 1500$, A_B is a constant 20% of the maximum ridge amplitude at fixed ℓ, $A_{i,\max}(\ell)$, and by $\ell \approx 1880$ it increases to a factor of 3 greater than $A_{i,\max}(\ell)$. Similarly, for the velocity power, P (which is proportional to $\sigma_j A_j$ and is shown in Fig. 3.12b), $P_B(\ell)/P_{i,\max}(\ell) \approx 1$ until $\ell \approx 1500$, and then increases with ℓ to ~ 20 at $\ell \approx 1880$. Similar results were found for the 1988 data set.

The cause of this background noise is unknown. There are two major classes of possible explanations. One is that the background noise is a real solar phenomenon. Duvall and Harvey (1986) have suggested a possible mechanism whereby large-scale convective turbulence (such as supergranulation) modulates the spatial frequency of the oscillations, thereby producing a plethora of nearby sidebands. If the sidebands are closely spaced and if the spatial frequency resolution is relatively poor, the sidebands could appear as background noise in the five-minute band. Duvall and Harvey (1986) even suggest that this effect has been seen in their data at $\ell = 150$, however, only at the 2% level. The other class of explanations is that the noise is due to some sort of spurious Doppler signal introduced into the data. Heterodyning of low temporal frequency, large velocity signals (again, such as supergranulation) by seeing can introduce broad-band noise (Ulrich *et al.* 1984). Phase jitter could also have been introduced by imperfect repointing of the telescope after the above-described seeing measurements. Changes in the angle of arrival of a light beam entering a birefringent filter produce changes in the spectral response of the filter. If the filter used in these observations was not perfectly telecentrically located in the optical path, then angle-of-arrival changes produced by seeing would cause spectral response changes, which would amplitude-modulate the Doppler oscillation signal (Grigoryev and Kobanov 1988). Again, this could produce sidebands that would show up as a background noise at five minutes.

The 1987 ℓ-ν diagram was calibrated by comparing the ridge frequencies in the range $170 \leq \ell \leq 400$ ($340 \leq \ell \leq 400$ for the 1988 data) with those determined from an intermediate-resolution data set containing full-disk Ca II K images. This data set has been described in detail by Libbrecht, Woodard, and Kaufman (1990), but, to briefly summarize, it contains frequencies in the intermediate-ℓ range of $145 \leq \ell \leq 400$, with typical uncertainties of ~ 1 μHz. The procedure for determining the optimal scale factor, $d\ell/dk$, is to assume different values of $d\ell/dk$, and for each value of $d\ell/dk$, calculate the difference between each measured frequency (from the high-resolution data set) and the appropriate reference frequency (from the intermediate-resolution data set). These differences are then averaged and plotted as a function of $d\ell/dk$. A line is then fit to the resulting points; the point at which the line intercepts the $d\ell/dk$-axis is the optimal value of $d\ell/dk$ (see Fig. 3.13). Using this method, we found a scale factor of $d\ell/dk = 21.304 \pm 0.013$ for 1987 and 42.735 ± 0.107 for 1988. These agreed adequately with the less accurate scale factors shown in Table 3.1, which were determined by independent means. The factor-of-10 difference in the scale factor errors is due to the fact that the region of comparison for 1987 contained 65 points, whereas for 1988 it contained only 10 points.

These Gaussian "ridge fits" are not completely free of systematic error, since they do not derive from a detailed model of the data. In addition to a possible scale error in the images, the dominant source of systematic errors in ridge-fit frequencies is due to a combination of the fact that the mode eigenfunctions are not completely orthogonal to our set of spatial filter functions, and that the oscillation power, P, is not constant at fixed n. The former allows spatial sidelobes from modes with $\ell' \neq \ell$ to leak into the spectrum $S_\ell(\nu)$, while the latter insures that sidelobes that are approximately symmetrically spaced in frequency about the central peak are not of equal amplitude. This tends to pull the measured frequency of a ridge in the direction of higher power. These systematic errors are approximated by

$$\Delta\nu \approx s^2 \frac{d\nu}{d\ell} \frac{1}{P} \frac{\partial P(n,\ell)}{\partial \ell} + \epsilon\ell \frac{d\nu}{d\ell}, \tag{3.7}$$

where we have followed Libbrecht and Kaufman (1988) in approximating the spherical harmonic overlap function by $V(\ell,\ell') = \exp[-(\ell - \ell' - \alpha)^2/2s^2]$, with $\alpha = \epsilon\ell$

representing a small scale error. Since an explicit derivation of Eq. (3.7) has never been published, we have included its derivation, along with those of Eqs. (3.8) and (3.9) below, in Appendix I.

The parameter s cannot be straightforwardly estimated from the data because of the artificially large linewidths. Instead, we considered the plane-wave approximation to the spherical harmonic overlap function, $V(\ell, \ell')$, finding

$$V(\ell, \ell') \approx \operatorname{sinc}^2 \frac{\pi(\ell - \ell')}{d\ell/dk}. \tag{3.8}$$

The small scale error, α, is not included here since it is considered separately in terms of corrections to the scale factor, $d\ell/dk$. The formalism developed in Eq. (3.7) can still be used if we approximate the plane-wave mode leakage function by a Gaussian of the appropriate width. By matching the full width at half maximum (FWHM) of the sinc^2 function with that of a Gaussian, we obtained

$$s = 0.3762 \frac{d\ell}{dk} \approx 8 \tag{3.9}$$

for the 1987 data. This produces corrections that range from -4 μHz to $+9$ μHz.

The corrected frequencies were then used to recalibrate the ℓ-ν diagram using the above-mentioned method, giving new scale factors of $d\ell/dk = 21.344 \pm 0.013$ for 1987 and $d\ell/dk = 42.921 \pm 0.101$ for 1988. Fig. 3.14 shows the region of overlap between the intermediate-ℓ frequencies used for the calibration and the 1987 corrected high-ℓ frequencies.

3.8 Random Errors

The corrected frequencies were interpolated using a cubic spline onto a grid with integral ℓ and spacing of 20 for 1987 and 40 for 1988. Random errors in the frequencies, $\sigma_{n\ell}$, were inferred by measuring the scatter in the fit frequencies along a given ridge. That is, for each ℓ in a given ridge, a quadratic polynomial in ℓ' was fit to the frequencies in that ridge over some range $\ell - \Delta\ell \leq \ell' \leq \ell + \Delta\ell$. After subtracting the polynomial fit, the uncertainty was determined from the residual scatter, assuming normally distributed errors. Typically, a 25-point (corresponding to $\Delta\ell = 240$ for 1987 and $\Delta\ell = 480$ for 1988) fit was used, except when there were less than 25 points in the ridge. In these cases, the quadratic was fit to the largest odd number of points in the ridge. At the ends of a ridge, 25 points (if available) were still used in the fit, but they were no longer centered on the mode of interest. By plotting the frequency differences between the high- and intermediate-ℓ data sets against $\frac{1}{2}s^2\frac{d\nu}{d\ell}\frac{1}{P}\frac{\partial P(n,\ell)}{\partial \ell}$ and $\epsilon\ell\frac{d\nu}{d\ell}$ from Eq. (3.7) (cf. Figs. 3a and 3b in Libbrecht and Kaufman 1988), we find that the residual systematic errors are of the order of $\pm$ 20 μHz for 1987, with considerable scatter. However, the random errors in the high-ℓ frequencies are considerably greater than those in the intermediate-ℓ calibration frequencies. When this is taken into account, we find that the systematic errors in the high-ℓ frequencies are probably no greater than the associated random errors. As an example, the systematic errors associated with the uncertainty in the scale factor, $d\ell/dk$, can be found as follows. Since $\nu \propto \ell^{1/2}$ (*cf.* Eq. 2.20), the error in frequency due to an uncertainty in ℓ is $\Delta\nu = \frac{1}{2}\frac{\Delta\ell}{\ell}\nu$. Now, $\Delta\ell = \epsilon k$, where ϵ is the error in the scale factor. Therefore,

$$\Delta\nu = \frac{1}{2}\frac{\epsilon}{d\ell/dk}\nu, \tag{3.10}$$

and, for $\nu = 4000$ μHz, $\Delta\nu = 1.2$ μHz. This is approximately 10 times smaller than the random errors in the frequencies. We therefore conservatively estimate that the remaining systematic errors are equal to the random errors. The final frequency uncertainty for a single mode can be found by adding, in quadrature, the random and systematic errors. This amounts to multiplying the random error by $\sqrt{2}$.

3.9 Discussion

Fig. 3.15 is a schematic ℓ-ν diagram showing both the 1987 and 1988 frequencies. Table 3.2 contains the high-ℓ frequencies and their uncertainties for the logical union of the 1987 and 1988 data sets, with 1987 values taking priority. The $\sigma_{n\ell}$ in Table 3.2 do not include the assumed remaining systematic errors. Fig. 3.15 can be used as a guide for determining which frequencies are from 1987 and which are from 1988. All the frequencies and their uncertainties in Table 3.2 are plotted schematically in Fig. 3.16. Also plotted in Fig. 3.16 is Eq. (2.8), a theoretical expression for the f-mode frequencies, $\omega^2 = gk_h$, or, equivalently, $\nu = 3158\sqrt{\ell/1000}$ μHz.

As can be seen from Fig. 3.16, there is a considerable discrepancy between the observed and theoretical values of the f-mode frequencies, going as high as 150 μHz at $\ell = 1860$. We are unable to explain this discrepancy. It could be real, in which case it might be caused by the presence of an exponentially decaying, horizontal chromospheric magnetic field. Roberts and Campbell (1988) and Campbell and Roberts (1989) have analyzed such a case, but they have calculated that the f-mode frequencies would *increase* by as much as 127 μHz at $\ell = 1300$ for a 200 Gauss field. Evans and Roberts (1990) have examined the case of a uniform chromospheric magnetic field and found even greater f-mode frequency shifts. However, these are, again, frequency increases.

Another explanation for the f-mode frequency shifts might involve variations in the propagation properties of the acoustic waves which result from modification of the wave phase velocity by turbulent convection. The basic idea is that turbulent convection introduces a small, randomly fluctuating velocity field which randomly increases and decreases the oscillation phase velocity. This reduces the average phase velocity of the wave, and hence decreases the frequency of the mode. Note that this mechanism acts not only on the f-modes, but also on the p-modes. Furthermore, the effect is greatest primarily at high ℓ and secondarily at high ν, since modes with these characteristics propagate primarily in the convection zone. Brown (1984) has examined the case of a randomly fluctuating vertical velocity field and has found that the frequency of the $\ell \approx 1450$ f-mode will be decreased by $\approx 17\,\mu$Hz. This is a factor of ~ 4 smaller than the measured difference. Goodman (1990) has considered the case where convection produces velocity fluctuations in the horizontal direction and has found similar results for the frequency shifts (albeit still an order of magnitude less than the observed shifts).[1]

---

[1] I thank Peter Goldreich for bringing these results to my attention.

We cannot exclude the possibility that the frequency discrepancy could also be due to unknown systematic effects, such as differential image motion, and misregistration between images induced by seeing and telescope shake. Hill (1984) has modeled the effects of differential image motion on modes with ℓ ranging from 500 to 550 and found that frequency differences up to 12 μHz can be produced. However, the difference is not systematically high or low, and the simulation assumes that the seeing is much worse than what would normally be encountered at any ground-based observatory. Finally, the f-mode frequencies might be pulled downward by the presence of the background noise. The background noise appears as a straight ridge in the ℓ-ν plane, which crosses below the f ridge at $\ell \approx 1400$ and, as noted above, makes the f ridge look asymmetric. This asymmetry could cause the centroid of the Gaussian fit to be shifted toward lower frequencies. However, we believe that we have accounted for this effect by including the appropriate background terms in Eq. (3.6). Also, the frequency discrepancy starts to appear at $\ell \approx 1000$, which is well before the background ridge crosses below the f ridge. If this pulling effect were the cause of the frequency differences, we would expect that the observed frequencies would be greater than the theoretical values for $\ell \lesssim 1000$, and this is not observed.

Finally, we consider any changes in the p-mode frequencies that may have occurred between 1987 and 1988 because of solar cycle effects. In Fig. 3.17 we show the frequency change, $\Delta\nu = \nu_{88} - \nu_{87}$, as a function of ℓ. The error bars were found by standard error-propagation techniques; i.e., $\sigma_{\Delta\nu} = \sqrt{\sigma_{87}^2 + \sigma_{88}^2}$. No attempt was made to classify the frequency change for different frequency ranges. After averaging these results we get $\langle\Delta\nu\rangle = 10.8 \pm 1.3$ μHz. The uncertainty associated with $\langle\Delta\nu\rangle$ does not contain any uncertainty associated with errors in the scale factors. Using Eq. (3.10) evaluated at 4000 μHz, we can include these uncertainties by adding them in quadrature to the intial uncertainty of 1.3 μHz to get a new result of $\langle\Delta\nu\rangle = 10.8 \pm 5.0$ μHz.

Libbrecht and Woodard (1990) have studied frequency changes over the period 1986–1988 for $5 \leq \ell \leq 140$ and $1\,\mathrm{mHz} \lesssim \nu \lesssim 4\,\mathrm{mHz}$. Throughout this range, they have found that $\Delta\nu \propto M_v^{-1}$, where M_v is the mode mass (see § 2.4). By assuming that this relationship still holds at $\ell \approx 1500$, we can compare our results with the Libbrecht and Woodard results. If we assume that their frequencies changed linearly with time over the two-year span from 1986 to 1988, we would expect $\Delta\nu(1500) \approx 2$ μHz. Murray (1990) has used the magnitude of the solar surface magnetic field, $|\mathrm{B}|$, averaged over the visible portion of the Sun, as an indicator of solar cycle related changes. His results, which are derived from Kitt Peak National Observatory full-disk magnetograms, show that magnetic activity was constant in the period 1986–1987, and that magnetic activity started to increase during the period 1987–1988. This suggests that all of the changes in the Libbrecht and Woodard frequencies occurred in the one-year period from 1987 to 1988, and that we would then expect $\Delta\nu(1500) \approx 4$ μHz. This $\gtrsim 1\sigma$ difference, combined with all of the aforementioned uncertainties that are due to both transient magnetic effects and high-ℓ frequency modifications resulting from surface interactions with turbulent convection, suggests that our frequency shifts are in agreement with those measured by Libbrecht and Woodard.

Table 3.2
Solar p-Mode Frequencies[a]

n	ℓ	ν	n	ℓ	ν	n	ℓ	ν
0	280	1698.2±5.5	0	920	3022.2± 3.7	0	1560	3855.2±14.0
	300	1743.6±5.5		940	3047.1± 3.7		1580	3881.5±14.3
	320	1799.1±5.5		960	3078.4± 3.5		1600	3906.9±14.4
	340	1867.7±5.5		980	3112.8± 3.4		1620	3943.3±14.4
	360	1903.9±5.5		1000	3140.1± 3.4		1640	3957.2±14.4
	380	1942.3±5.5		1020	3167.8± 3.2		1660	3976.8±14.4
	400	1998.0±5.5		1040	3195.8± 3.1		1680	3992.2±14.4
	420	2042.8±5.5		1060	3230.7± 3.3		1700	4019.4±14.4
	440	2090.9±5.5		1080	3261.4± 3.4		1720	4010.6±14.4
	460	2147.4±5.5		1100	3281.8± 3.6		1740	4042.0±14.4
	480	2190.2±5.5		1120	3309.3± 3.4		1760	4048.3±14.4
	500	2227.8±5.5		1140	3341.7± 3.3		1780	4067.5±14.4
	520	2277.8±5.5		1160	3368.9± 3.7		1800	4150.8±14.4
	540	2325.4±5.6		1180	3394.7± 4.1		1820	4140.1±14.4
	560	2364.8±5.5		1200	3418.3± 4.3		1840	4132.8±14.4
	580	2404.1±5.6		1220	3444.9± 4.3		1860	4156.2±14.4
	600	2437.8±4.5		1240	3471.0± 4.3		1880	4272.7±22.3[b]
	620	2487.1±4.6		1260	3494.4± 5.4		1920	4275.8±22.3[b]
	640	2523.9±4.2		1280	3519.2± 5.4			
	660	2562.8±4.2		1300	3540.3± 5.4	1	180	1900.4± 7.0
	680	2602.3±4.1		1320	3565.0± 5.5		200	1975.1± 7.0
	700	2632.4±4.1		1340	3602.4± 5.5		220	2044.9± 7.0
	720	2671.4±3.9		1360	3621.2± 5.4		240	2110.0± 7.0
	740	2712.5±3.9		1380	3644.0± 6.4		260	2159.9± 7.0
	760	2742.6±3.8		1400	3676.2± 6.6		280	2215.7± 7.0
	780	2778.3±3.8		1420	3702.5± 6.7		300	2296.4± 7.0
	800	2821.0±3.7		1440	3711.5± 6.7		320	2345.6± 7.0
	820	2857.6±3.6		1460	3738.9± 7.0		340	2399.8± 7.0
	840	2890.9±3.7		1480	3771.4± 8.2		360	2448.9± 7.0
	860	2926.3±3.6		1500	3777.6± 8.4		380	2501.1± 7.0
	880	2957.1±3.5		1520	3814.8± 9.5		400	2546.7± 7.0
	900	2984.1±3.6		1540	3845.9±10.5		420	2604.2± 7.0

Note: All values derived from 1987 data except where noted.

[a] n = Radial Order, ℓ = Spherical Harmonic Degree, ν = Frequency (μHz).

[b] Value derived from 1988 data.

Table 3.2
Solar p-Mode Frequencies[a]

n	ℓ	ν	n	ℓ	ν	n	ℓ	ν
1	460	2700.5±6.0	1	1100	4070.1± 5.9	2	220	2490.1±11.7
	480	2745.3±6.0		1120	4108.3± 6.0		240	2565.7±11.7
	500	2795.2±5.8		1140	4147.1± 6.0		260	2637.8±11.7
	520	2846.4±5.8		1160	4189.2± 7.2		280	2709.6±11.7
	540	2890.1±5.7		1180	4232.1± 8.7		300	2787.1±11.7
	560	2929.7±4.4		1200	4267.4± 8.8		320	2844.1±11.7
	580	2977.9±3.8		1220	4303.9±10.0		340	2912.5±11.7
	600	3024.7±3.7		1240	4356.1±12.0		360	2961.7±11.7
	620	3065.2±3.8		1260	4391.5±13.5		380	3027.3±11.7
	640	3116.7±3.8		1280	4427.8±14.4		400	3089.6±11.7
	660	3159.2±3.6		1300	4461.8±14.4		420	3138.5±11.7
	680	3199.4±3.8		1320	4501.6±20.8		440	3194.4± 8.7
	700	3241.4±3.7		1340	4537.2±20.9		460	3252.4± 8.4
	720	3281.3±3.8		1360	4591.2±20.9		480	3307.8± 8.4
	740	3329.2±3.7		1380	4642.4±22.5		500	3359.1± 8.2
	760	3372.6±3.7		1400	4671.1±23.3		520	3412.0± 7.9
	780	3410.9±3.6		1420	4709.1±23.4		540	3471.3± 7.8
	800	3450.5±3.8		1440	4766.6±23.4		560	3519.7± 6.3
	820	3497.2±3.9		1460	4836.4±23.4		580	3565.6± 5.7
	840	3547.4±4.1		1480	4886.5±23.4		600	3622.5± 4.7
	860	3586.5±4.1		1500	4924.3±23.4		620	3675.6± 4.9
	880	3623.1±4.1		1520	4957.4±23.4		640	3721.5± 4.9
	900	3663.6±4.1		1540	4968.2±23.4		660	3781.5± 5.1
	920	3701.3±4.0		1560	5083.2±23.4		680	3832.7± 5.6
	940	3751.0±4.1		1580	5061.9±23.4		700	3877.4± 5.6
	960	3785.8±4.1		1600	5082.1±23.4		720	3922.5± 5.6
	980	3829.9±4.0		1620	5088.2±23.4		740	3982.3± 5.9
	1000	3873.6±4.7		1640	5133.9±23.4		760	4024.8± 6.0
	1020	3910.9±5.0		1660	5194.1±23.4		780	4065.6± 6.2
	1040	3945.0±5.0					800	4119.9± 6.7
	1060	3996.9±5.0	2	180	2298.5±11.7		820	4171.8± 7.8
	1080	4037.9±5.1		200	2400.3±11.7		840	4225.2± 7.7

Note: All values derived from 1987 data except where noted.

[a] n = Radial Order, ℓ = Spherical Harmonic Degree, ν = Frequency (μHz).

[b] Value derived from 1988 data.

Table 3.2
Solar p-Mode Frequencies[a]

n	ℓ	ν	n	ℓ	ν	n	ℓ	ν
2	880	4320.1± 8.2	3	340	3391.8±10.4	3	980	5245.2± 7.5
	900	4374.3± 8.2		360	3457.6±10.4		1000	5310.9± 7.5
	920	4425.1± 9.5		380	3535.2±10.4		1020	5346.2± 7.5
	940	4465.3±12.0		400	3606.5±10.4			
	960	4506.8±13.0		420	3669.2±10.4	4	180	3021.9± 9.2
	980	4549.2±13.1		440	3740.6± 8.3		200	3149.8± 9.2
	1000	4600.8±13.6		460	3804.8± 8.4		220	3261.3± 9.2
	1020	4648.0±14.0		480	3861.5± 8.3		240	3353.3± 9.2
	1040	4694.2±15.7		500	3925.4± 8.3		260	3448.4± 9.2
	1060	4737.3±16.2		520	3990.8± 8.3		280	3545.8± 9.2
	1080	4805.7±16.2		540	4050.0± 8.3		300	3654.5± 9.2
	1100	4861.2±16.2		560	4105.3± 7.5		320	3750.9± 9.2
	1120	4889.2±16.2		580	4162.9± 6.1		340	3840.0± 9.2
	1140	4944.1±16.2		600	4224.7± 5.2		360	3912.6± 9.2
	1160	5016.8±16.2		620	4290.5± 5.1		380	4007.0± 9.2
	1180	5075.4±16.2		640	4344.4± 5.0		400	4092.1± 9.2
	1200	5110.2±16.2		660	4406.8± 6.2		420	4175.3± 9.2
	1220	5123.6±16.2		680	4456.1± 6.4		440	4264.2± 8.7
	1240	5196.5±16.2		700	4502.4± 6.8		460	4334.6± 8.9
	1260	5243.9±16.2		720	4574.1± 6.9		480	4406.7± 8.7
	1280	5237.8±16.2		740	4627.1± 7.2		500	4475.4±11.3
	1300	5299.1±16.2		760	4676.0± 7.3		520	4549.0±11.3
	1320	5305.2±14.0[b]		780	4728.6± 7.5		540	4635.9±11.3
				800	4785.3± 7.5		560	4691.3±11.3
3	180	2666.9±10.4		820	4844.4± 7.5		580	4749.5±11.3
	200	2779.4±10.4		840	4898.6± 7.5		600	4815.4±11.3
	220	2884.9±10.4		860	4951.9± 7.5		620	4881.9±11.3
	240	2969.0±10.4		880	5008.9± 7.5		640	4946.3±11.3
	260	3049.2±10.4		900	5072.8± 7.5		660	4997.9±11.3
	280	3145.0±10.4		920	5114.8± 7.5		680	5068.6±11.3
	300	3235.9±10.4		940	5167.0± 7.5		700	5124.0±11.3
	320	3318.8±10.4		960	5199.8± 7.5		720	5198.0±11.3

Note: All values derived from 1987 data except where noted.

[a] n = Radial Order, ℓ = Spherical Harmonic Degree, ν = Frequency (μHz).

[b] Value derived from 1988 data.

Table 3.2
Solar p-Mode Frequencies[a]

n	ℓ	ν	n	ℓ	ν	n	ℓ	ν
5	180	3340.0±16.0	5	520	5080.0±11.3	6	420	5065.2±11.6
	200	3480.2±16.0		540	5126.6±11.3		440	5172.2±11.6
	220	3614.8±16.0		560	5219.6±11.3			
	240	3729.2±16.0		580	5314.0±11.3	7	180	3937.5±17.1
	260	3833.4±16.0					200	4110.2±17.1
	280	3943.4±16.0	6	180	3632.3±13.0		220	4289.4±17.1
	300	4075.7±16.0		200	3797.5±13.0		240	4399.1±17.1
	320	4161.1±16.0		220	3963.7±13.0		260	4533.4±17.1
	340	4279.1±16.0		240	4081.8±13.0		280	4706.2±17.0
	360	4357.2±16.0		260	4212.1±13.0		300	4815.1±17.0
	380	4448.2±16.0		280	4314.4±13.0		320	4940.1±17.0
	400	4543.1± 9.2		300	4442.8±13.0		340	5062.5±17.0
	420	4641.9± 9.2		320	4561.5±11.6		360	5155.6±17.0
	440	4738.6± 8.7		340	4665.0±11.6			
	460	4827.5± 8.9		360	4760.6±11.6	8	180	4230.0±17.1
	480	4873.1± 8.7		380	4869.2±11.6		200	4423.7±17.1
	500	4967.0±11.3		400	4974.2±11.6		220	4600.2±17.1

Note: All values derived from 1987 data except where noted.

[a] n = Radial Order, ℓ = Spherical Harmonic Degree, ν = Frequency (μHz).

[b] Value derived from 1988 data.

Figure Captions

Figure 3.1: A schematic of the typical optical bench setup used at Big Bear Solar Observatory (BBSO) for the collection of Dopplergrams. See the text for a description of the different components. These optics were used on both the 25 cm (10 in) vacuum refractor and the 66 cm (26 in) vacuum reflector at BBSO. The commonly used videomagnetograph (VMG) system is essentially the same except that the circular polarizer is removed from the optical path.

Figure 3.2: A schematic of the data acquisition system used in the collection of Dopplergrams at BBSO. See the text for a description of the operation of the system.

Figure 3.3: A typical Dopplergram collected by the BBSO VMG system. The image size is approximately $136'' \times 100''$.

Figure 3.4: A schematic diagram illustrating the calculation of a k_x-k_y-ω diagram from a time series of Dopplergrams.

Figure 3.5: A schematic illustration of the mode structure of the oscillations as seen in k_x-k_y-ω space. The different surfaces correspond to different values of the radial quantum number n. The slight nonaxisymmetry in the surfaces is due to solar rotation. Taken from Hill (1988).

Figure 3.6: An ℓ-ν power spectrum diagram for the 1987 data. Power can be seen out to $\ell \sim 1800$. For this diagram we have used a scale factor of $d\ell/dk = 21.344$.

Figure 3.7: An ℓ-ν power spectrum diagram for the 1988 data. Power can be seen out to $\ell \sim 1900$. For this diagram we have used a scale factor of $d\ell/dk = 42.921$. Since the seeing was better for the 1988 data set, power can be seen out to higher ℓ. Also note that since the 1988 time series was half as long as the 1987 time series, the temporal frequency resolution for 1988 is twice as large as for 1987.

Figure 3.8: The background power fit coefficients ν_B, σ_B, A_B, and C, from the nonlinear, least-squares fit of the averaged power spectra, $S_k(\nu)$, to Eq. (3.6). Note that for $k \gtrsim 54$ ($\ell \gtrsim 1100$), the fits suffer from convergence problems. The bold lines are linear fits to ν_B and σ_B, for $k \lesssim 54$.

Figure 3.9: The same background fit coefficients, except that ν_B and σ_B are no longer free parameters in the fit, and are set to vary linearly with k. Note that A_B and C vary in a much smoother fashion now.

Figure 3.10: Typical power spectra from the 1987 data set (shown in Fig. 3.6) and their Gaussian ridge fits (i.e., to Eq. 3.6 in the text). Also shown are the ridge identifications (f and p_i), along with the Gaussian component of the background noise (B).

Figure 3.11: A schematic ℓ-ν diagram showing the raw ν_i determined from the Gaussian ridge fits. The error bars are given by the ridge widths, σ_i. The data shown are from the 1987 data set.

Figure 3.12: (a) Ratio of the background Gaussian amplitude, A_B, to the maximum ridge amplitude, $A_{i,\max}$. (b) A similar plot for velocity power, P_B and $P_{i,\max}$. Velocity power is proportional to $\sigma_j A_j$.

Figure 3.13: A comparison of the intermediate-ℓ "standard" frequencies in Libbrecht, Woodard, and Kaufman (1990) with the measured, raw ν_i from the Gaussian ridge fits, for different values of the scale factor $d\ell/dk$. The point at which a straight line fit to the averaged frequency differences crosses the $d\ell/dk$-axis is the optimal value of the scale factor. A value of $d\ell/dk = 21.304 \pm 0.013$ was found for the 1987 data (shown here).

Figure 3.14: A schematic ℓ-ν diagram showing the overlap region between the full-disk, intermediate-ℓ frequencies from Libbrecht, Woodard, and Kaufman (1990) ($\cdots$), and the ν_i from the 1987 Gaussian ridge fits ($\times$), corrected for the systematic

effects described by Eq. (3.7).

Figure 3.15: A schematic ℓ-ν diagram showing both the 1987 (+) and 1988 (×) mode frequency determinations. This figure can be used as a guide for determining which frequencies in Table 3.2 are from 1987 and which are from 1988.

Figure 3.16: A schematic ℓ-ν diagram showing the final mode frequency determinations and their uncertainties (given in Table 3.2). Also plotted is the theoretical expectation for the f-mode frequencies, $\omega^2 = gk$, or, equivalently, $\nu = 3158\sqrt{\ell/1000}$ μHz. Note that at high ℓ, the measured f-mode frequencies are significantly below the theoretical expectation.

Figure 3.17: The differences between the 1987 and 1988 frequencies plotted as a function of ℓ. The average difference is $\langle\Delta\nu\rangle = 10.8 \pm 5.0$ μHz and was found to be not significant. See the text for further discussion.

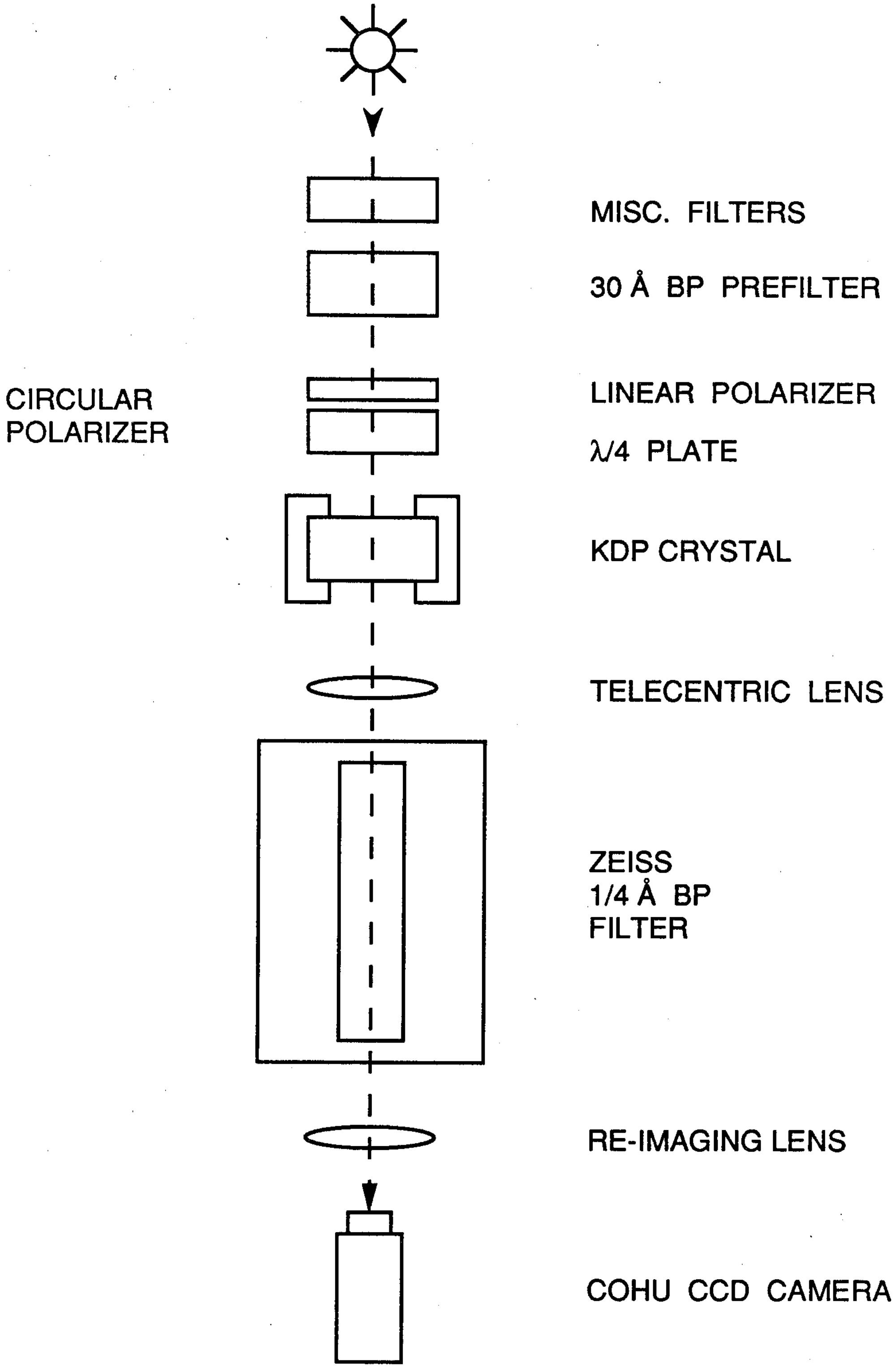
MISC. FILTERS
30 Å BP PREFILTER
CIRCULAR POLARIZER
LINEAR POLARIZER
λ/4 PLATE
KDP CRYSTAL
TELECENTRIC LENS
ZEISS 1/4 Å BP FILTER
RE-IMAGING LENS
COHU CCD CAMERA

Fig. 3.1

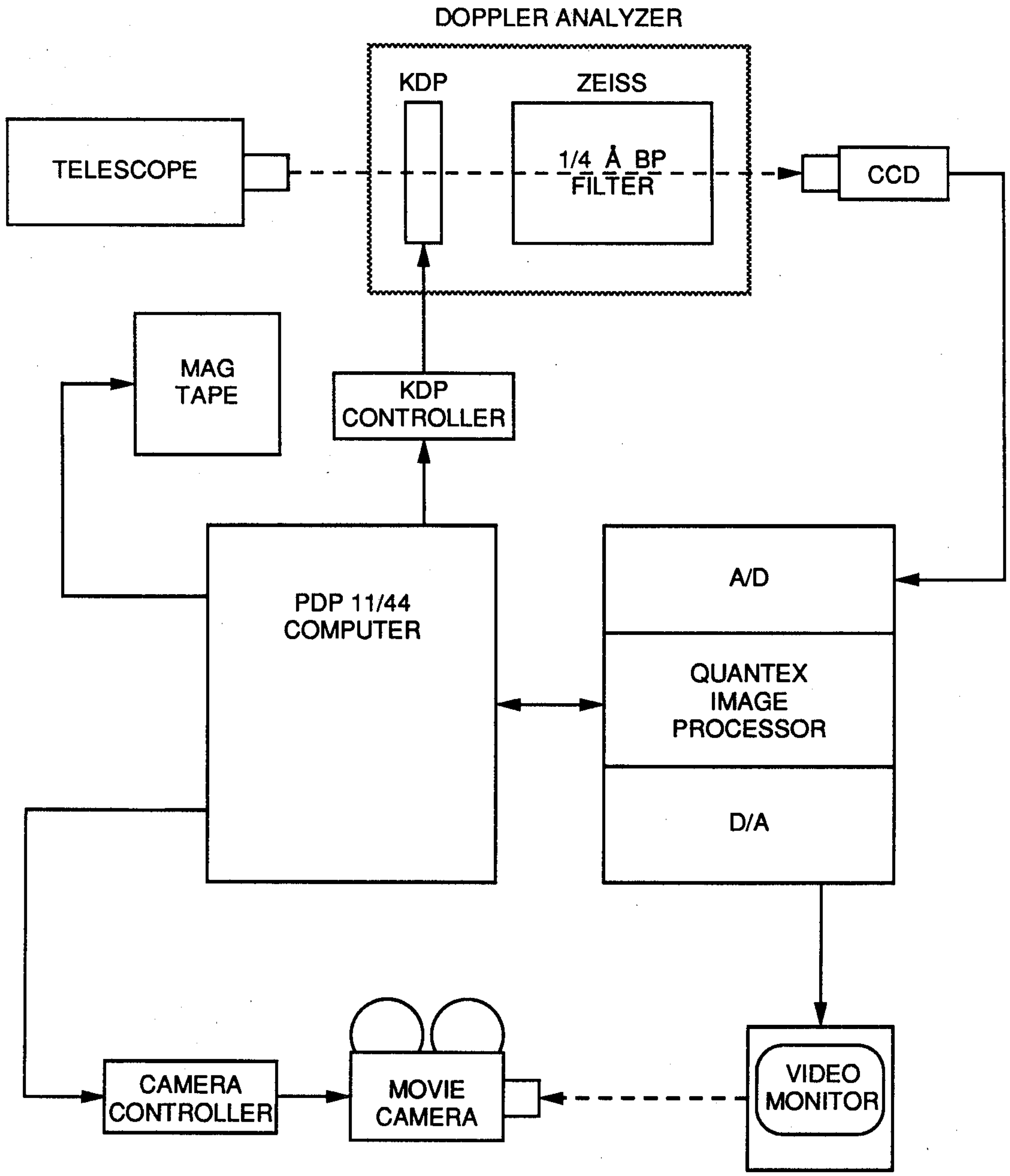
DOPPLER ANALYZER
KDP
ZEISS
TELESCOPE
1/4 Å BP FILTER
CCD
MAG TAPE
KDP CONTROLLER
PDP 11/44 COMPUTER
A/D
QUANTEX IMAGE PROCESSOR
D/A
CAMERA CONTROLLER
MOVIE CAMERA
VIDEO MONITOR

Fig. 3.2

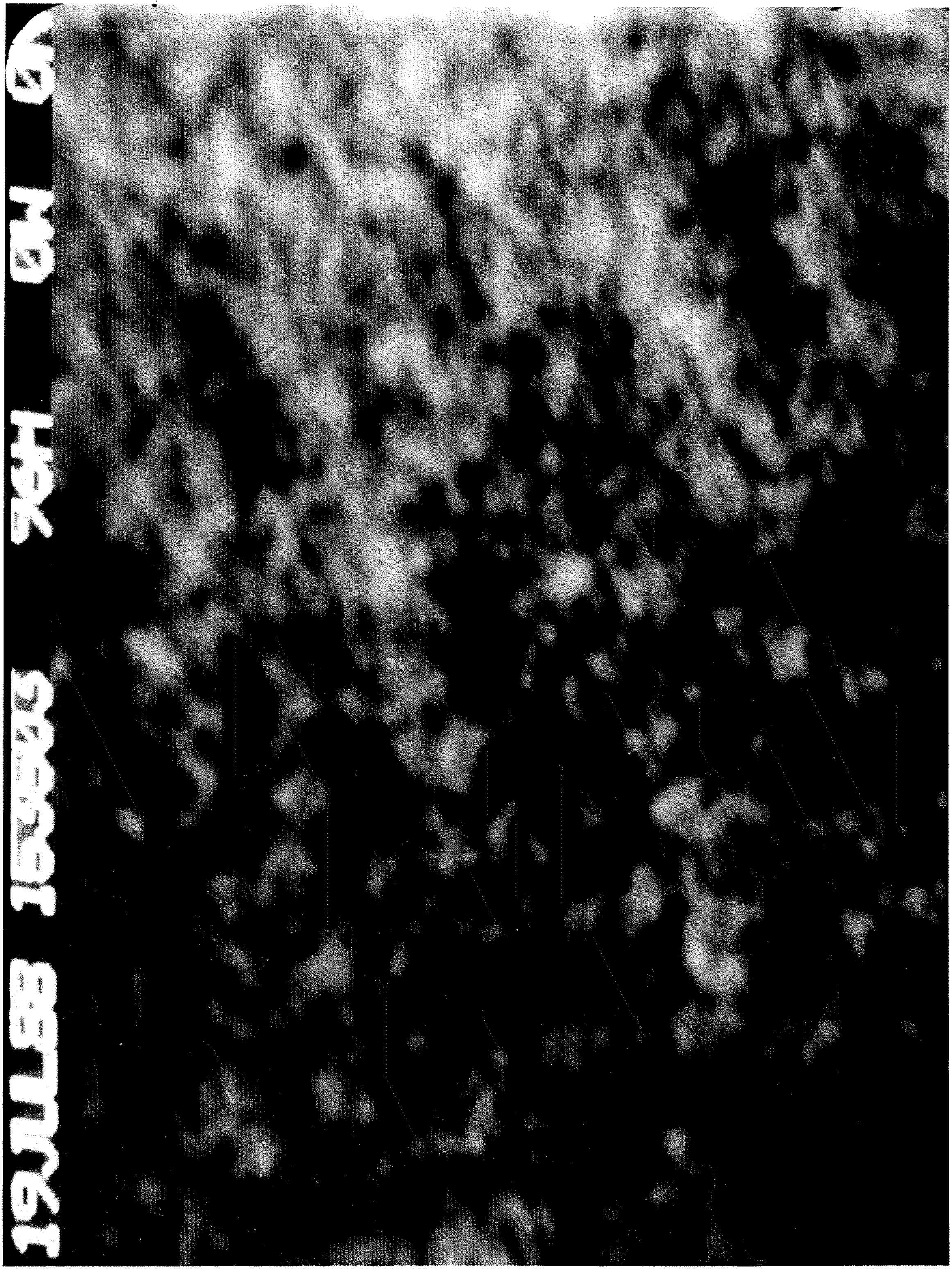

Fig. 3.3

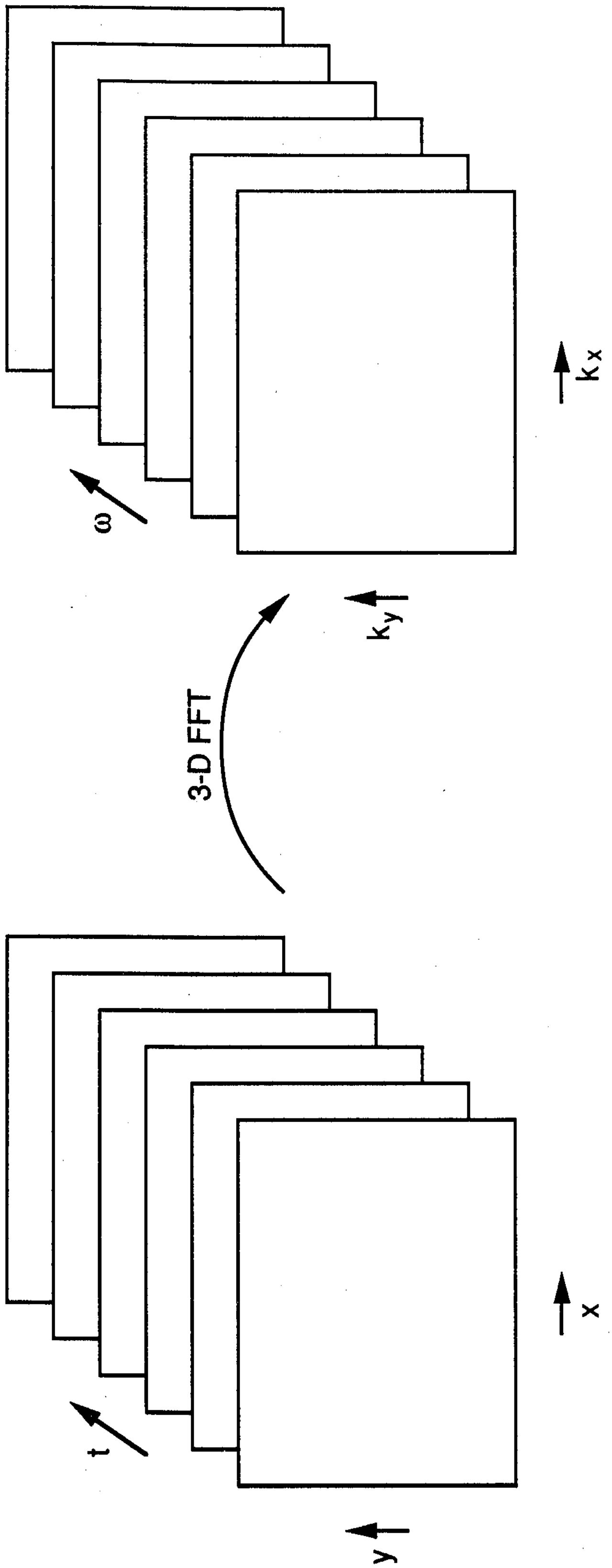

Fig. 3.4

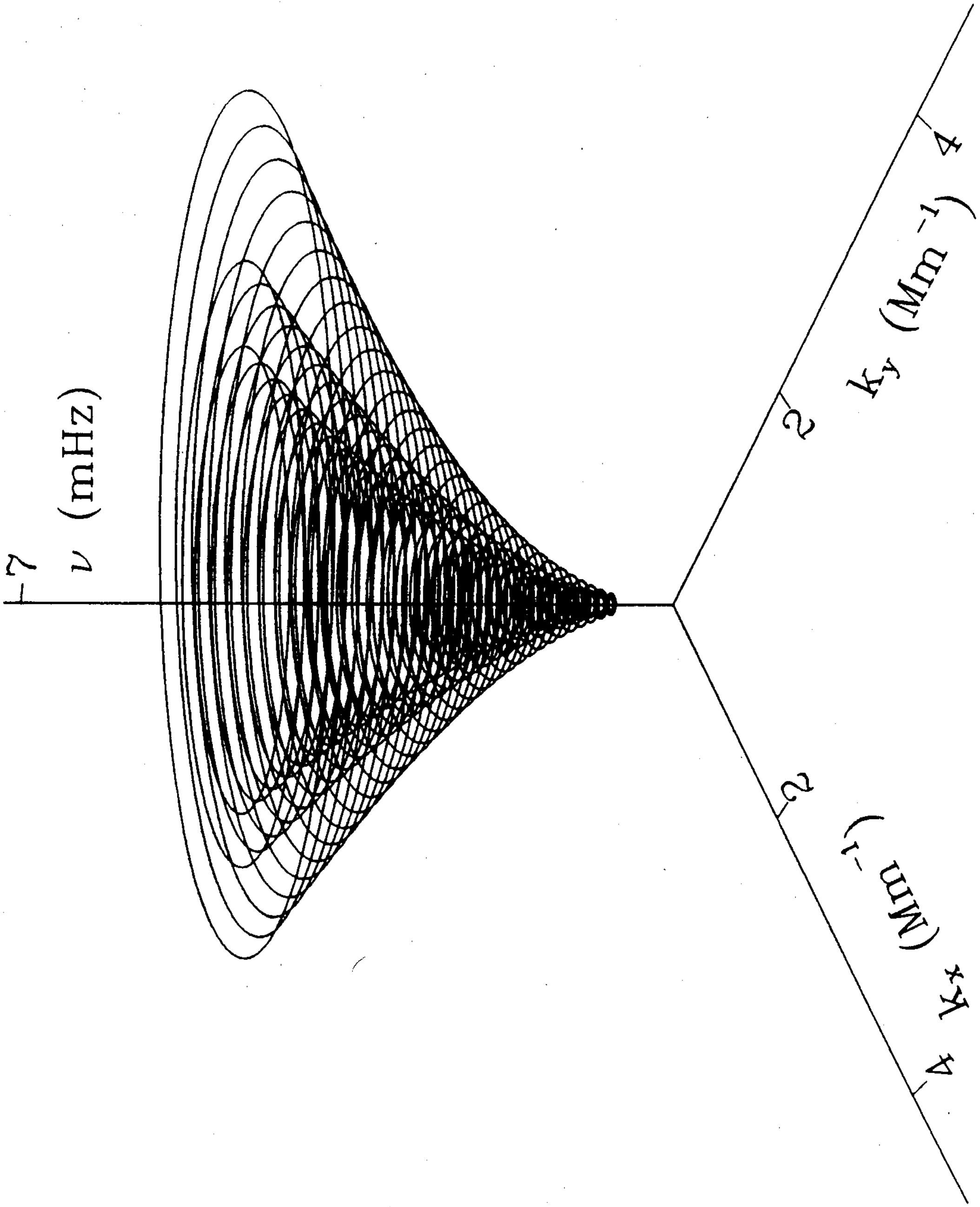

Fig. 3.5

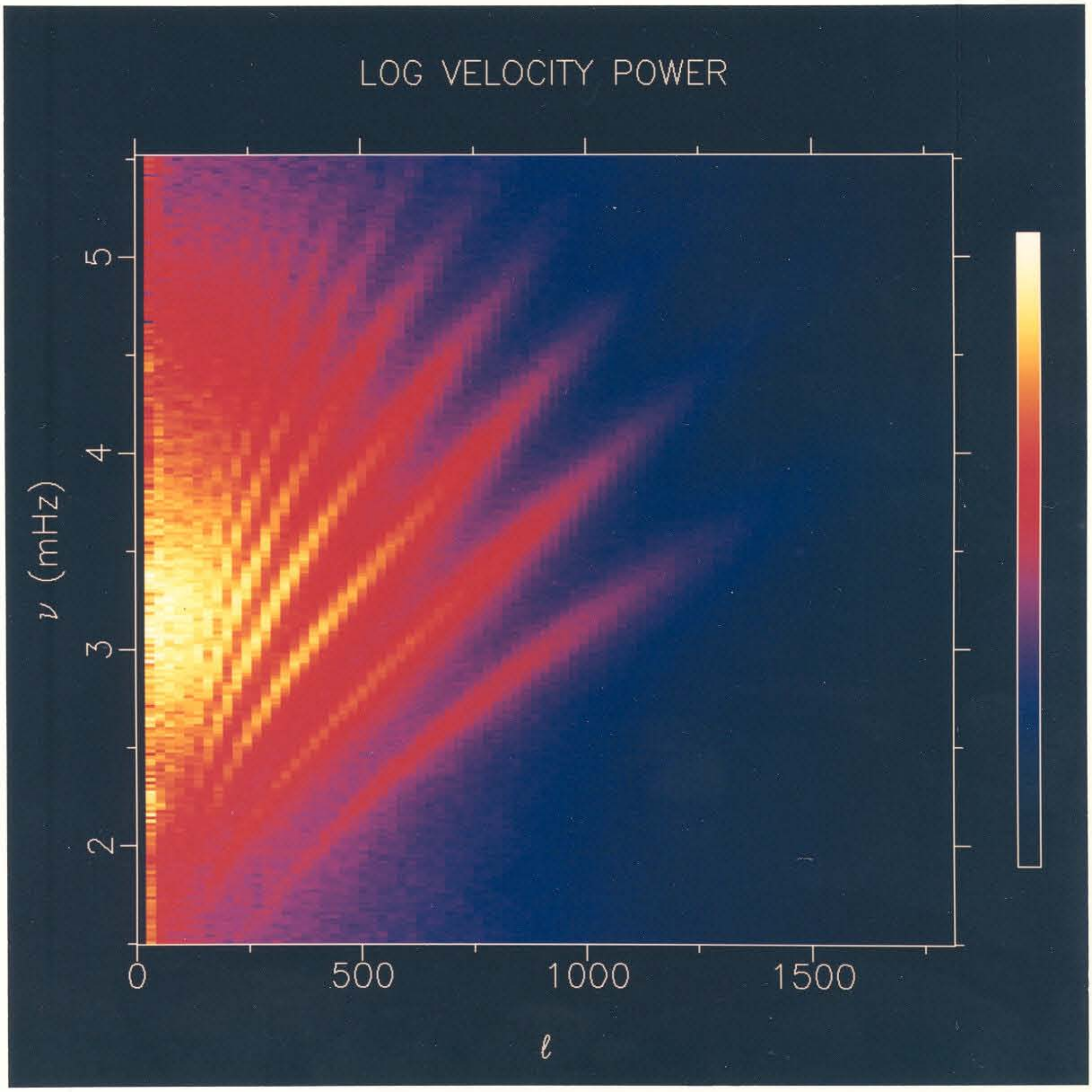

Fig. 3.6

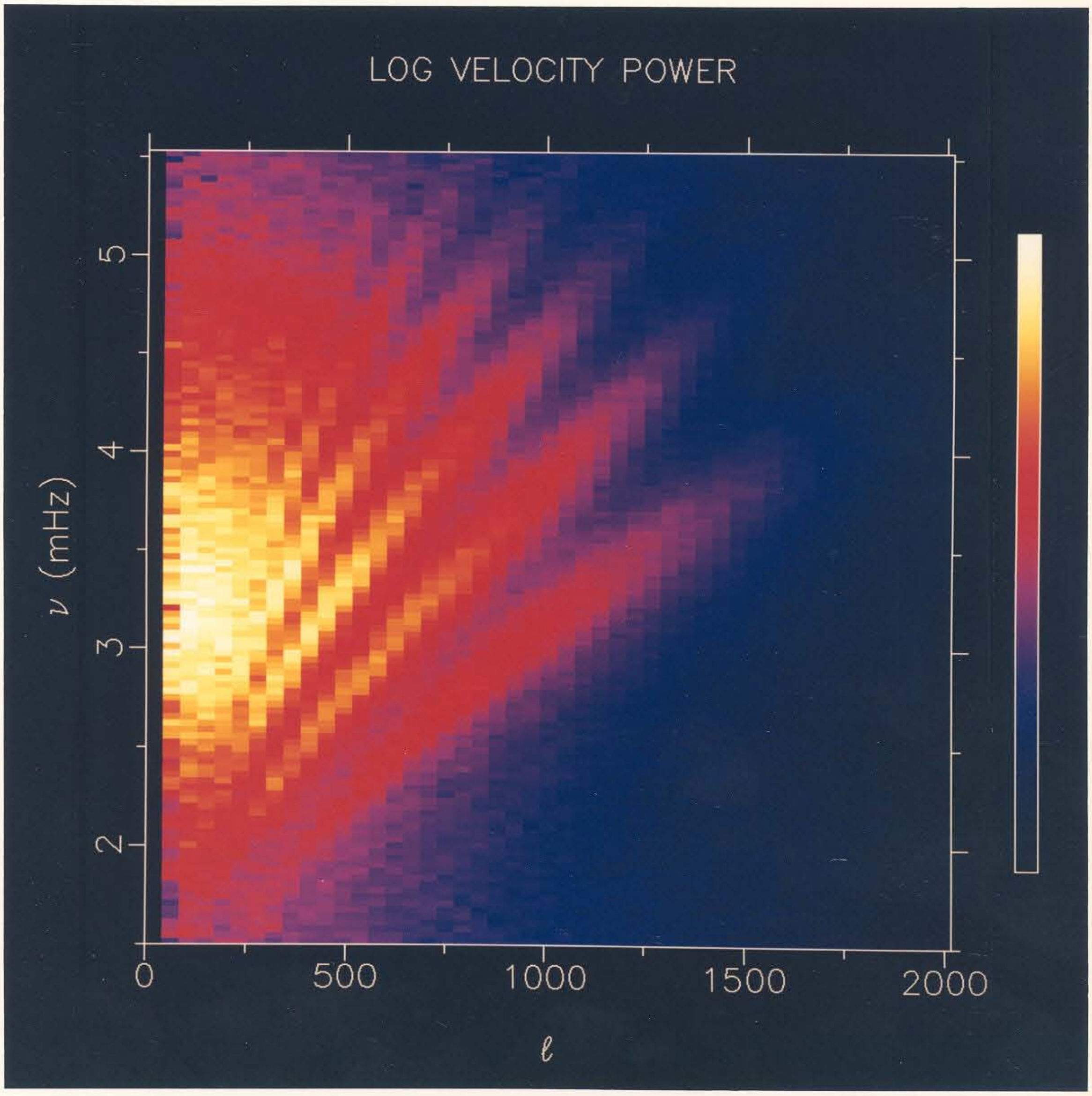

Fig. 3.7

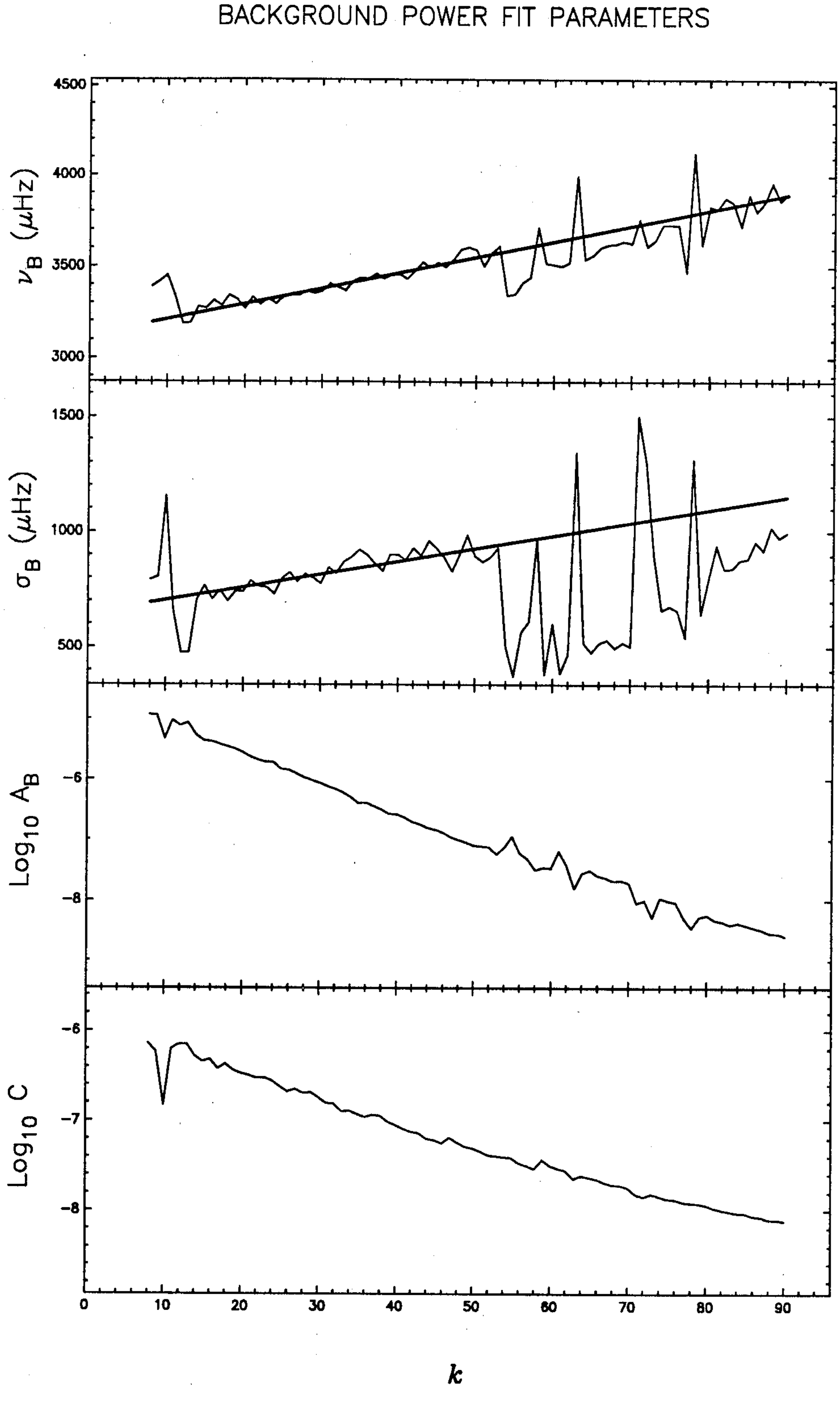
BACKGROUND POWER FIT PARAMETERS
ν_B (μHz)
4500
4000
3500
3000
σ_B (μHz)
1500
1000
500
Log$_{10}$ A$_B$
-6
-8
Log$_{10}$ C
-6
-7
-8
0
10
20
30
40
50
60
70
80
90
k

Fig. 3.8

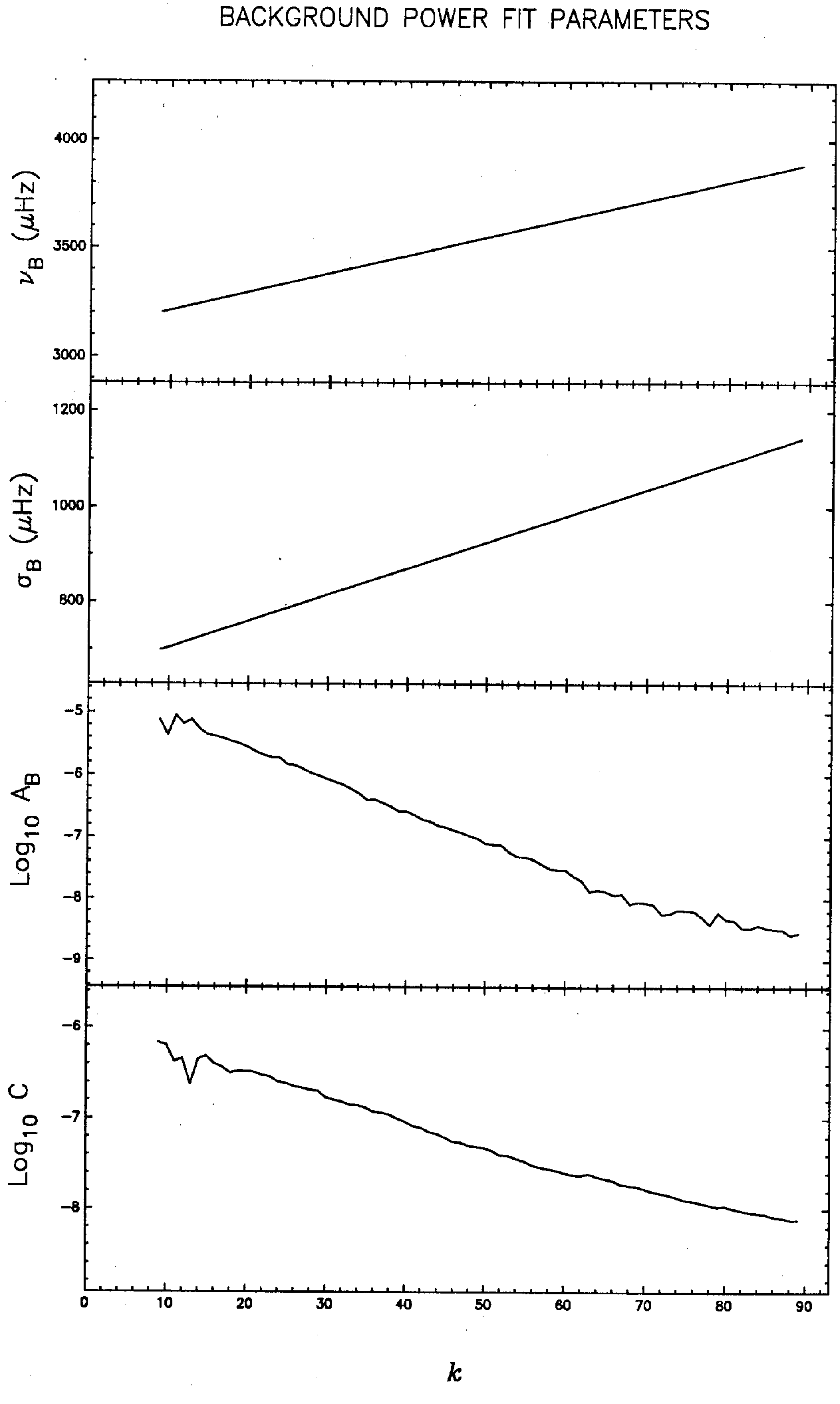
BACKGROUND POWER FIT PARAMETERS
ν_B (μHz)
4000
3500
3000
σ_B (μHz)
1200
1000
800
$\text{Log}_{10}\ A_B$
-5
-6
-7
-8
-9
Log_{10} C
-6
-7
-8
0
10
20
30
40
50
60
70
80
90
k

Fig. 3.9

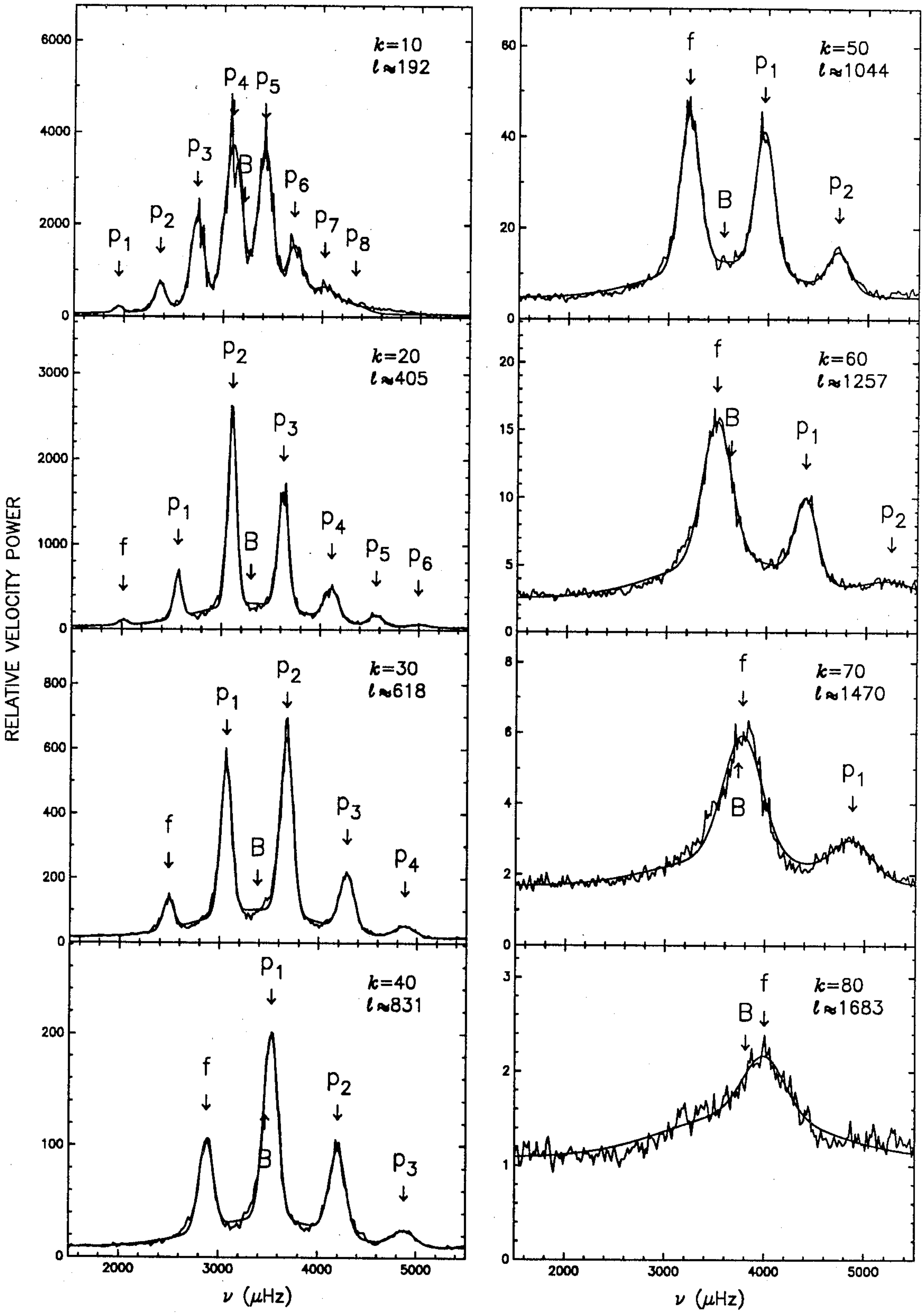
RELATIVE VELOCITY POWER
ν (μHz)
k=10
l≈192
k=20
l≈405
k=30
l≈618
k=40
l≈831
k=50
l≈1044
k=60
l≈1257
k=70
l≈1470
k=80
l≈1683
f
B
p1
p2
p3
p4
p5
p6
p7
p8
2000
3000
4000
5000

Fig. 3.10

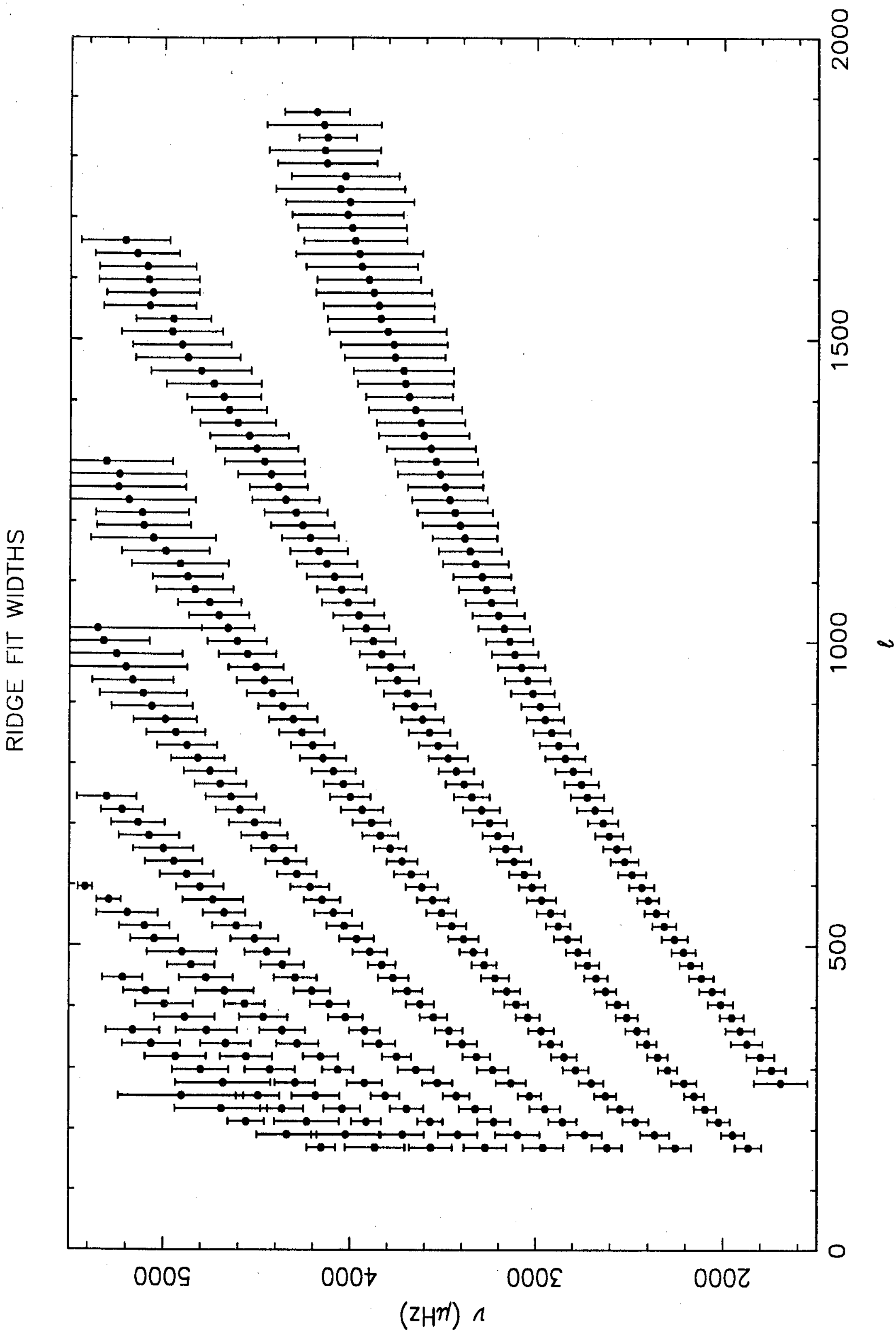
RIDGE FIT WIDTHS
ℓ
0
500
1000
1500
2000
ν (μHz)
2000
3000
4000
5000

Fig. 3.11

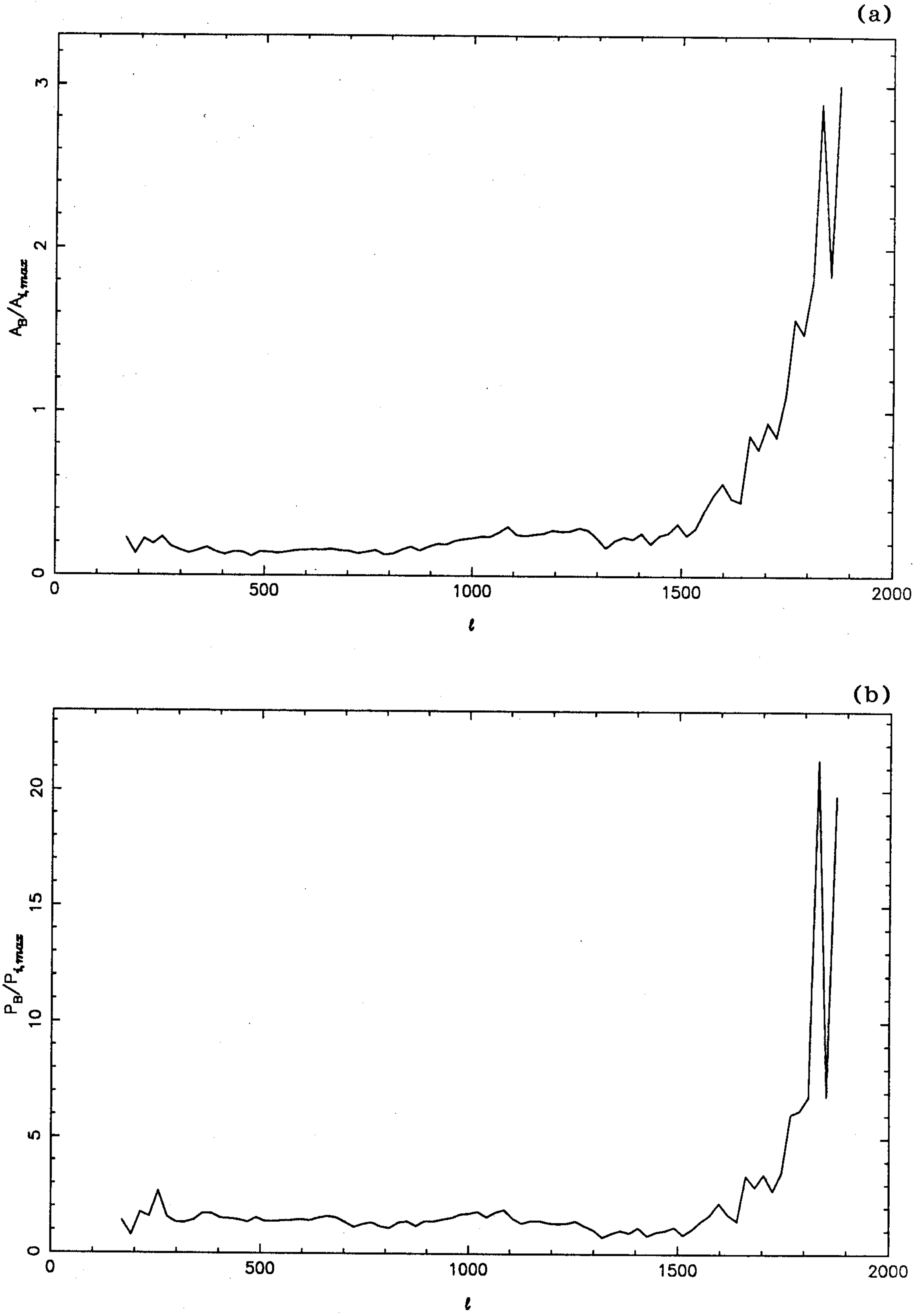
(a)
A_B/A_{l,max}
0
1
2
3
0
500
1000
1500
2000
ℓ
(b)
P_B/P_{l,max}
0
5
10
15
20
0
500
1000
1500
2000
ℓ

Fig. 3.12

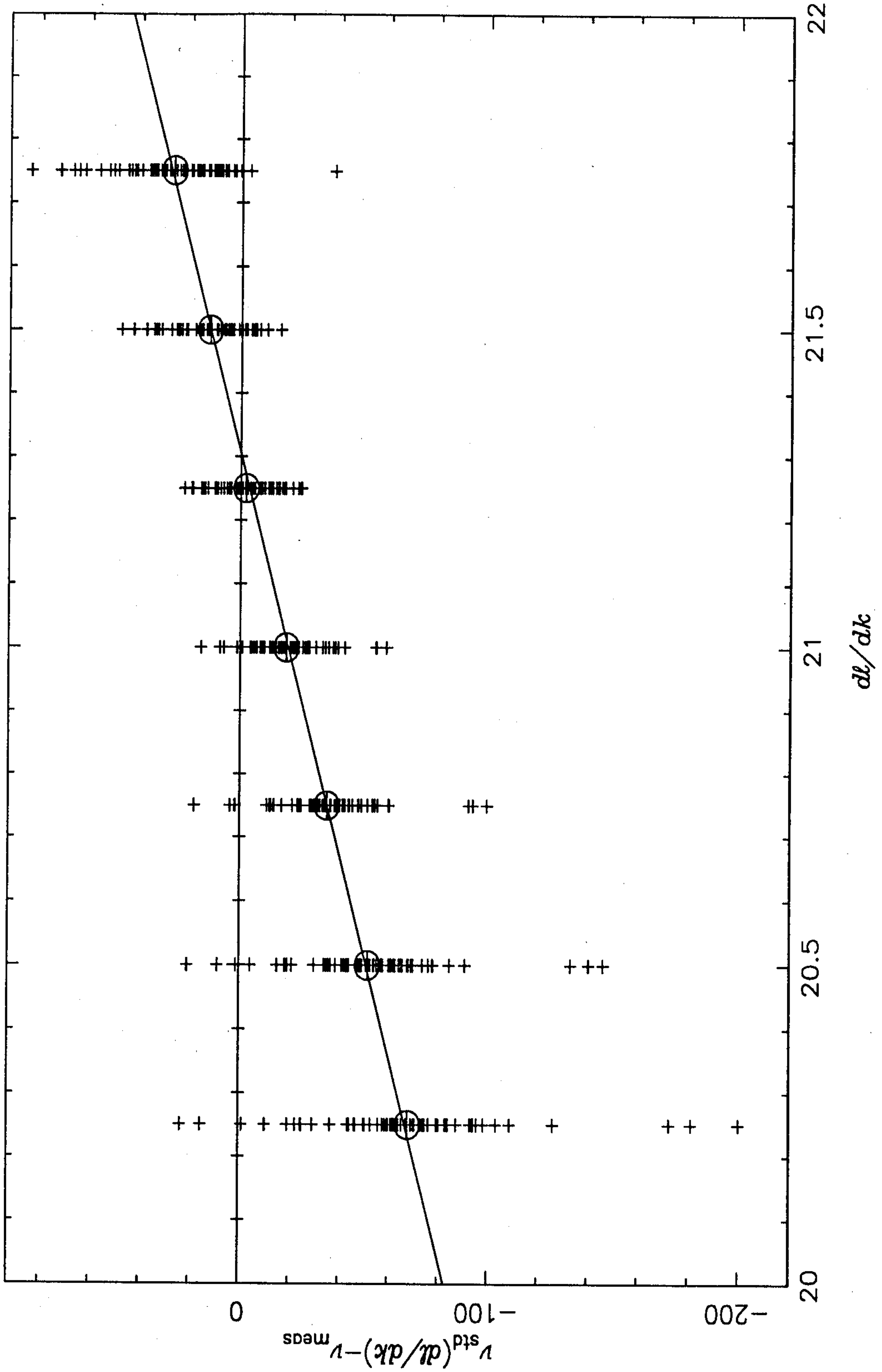

Fig. 3.13

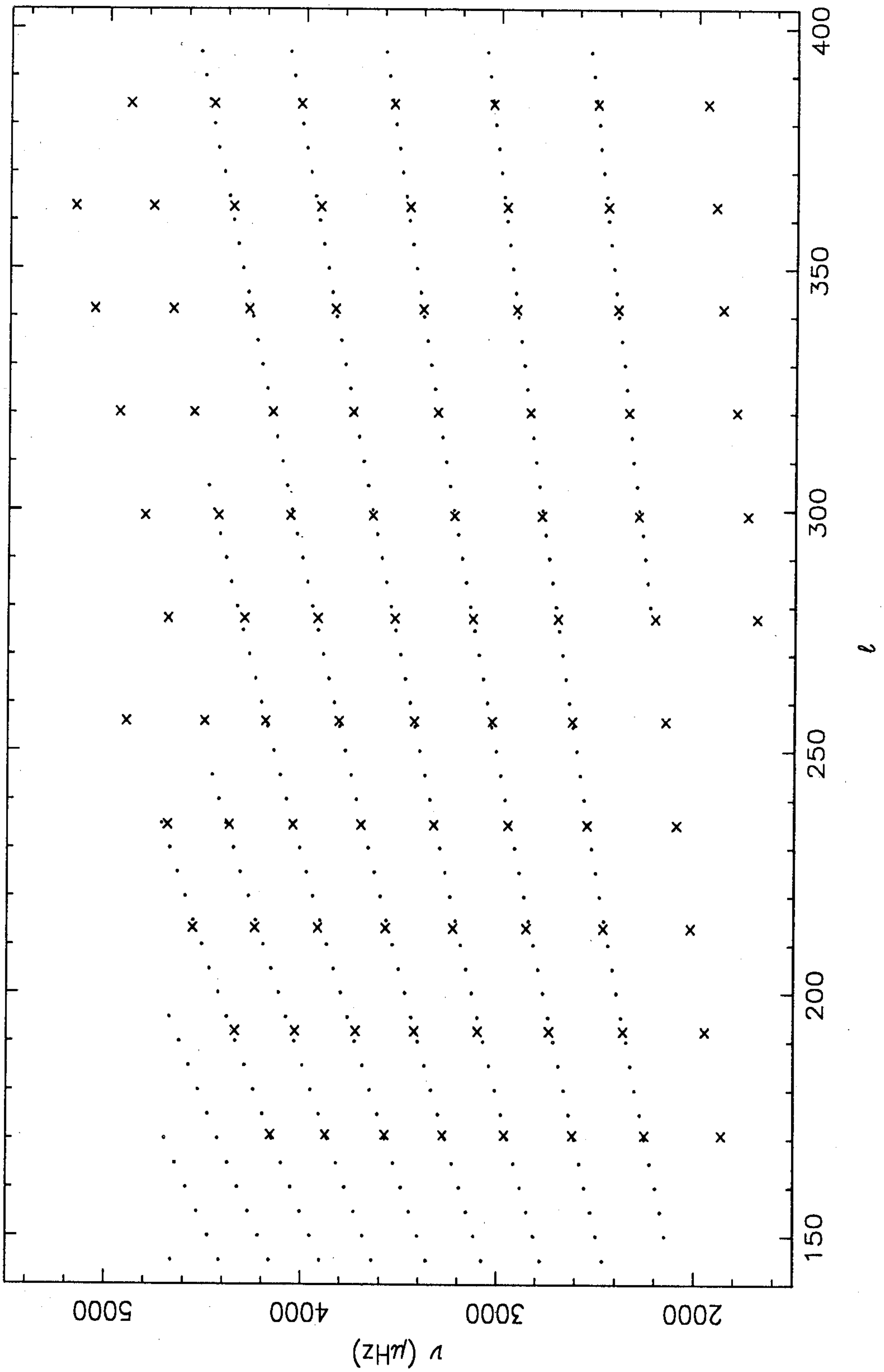

Fig. 3.14

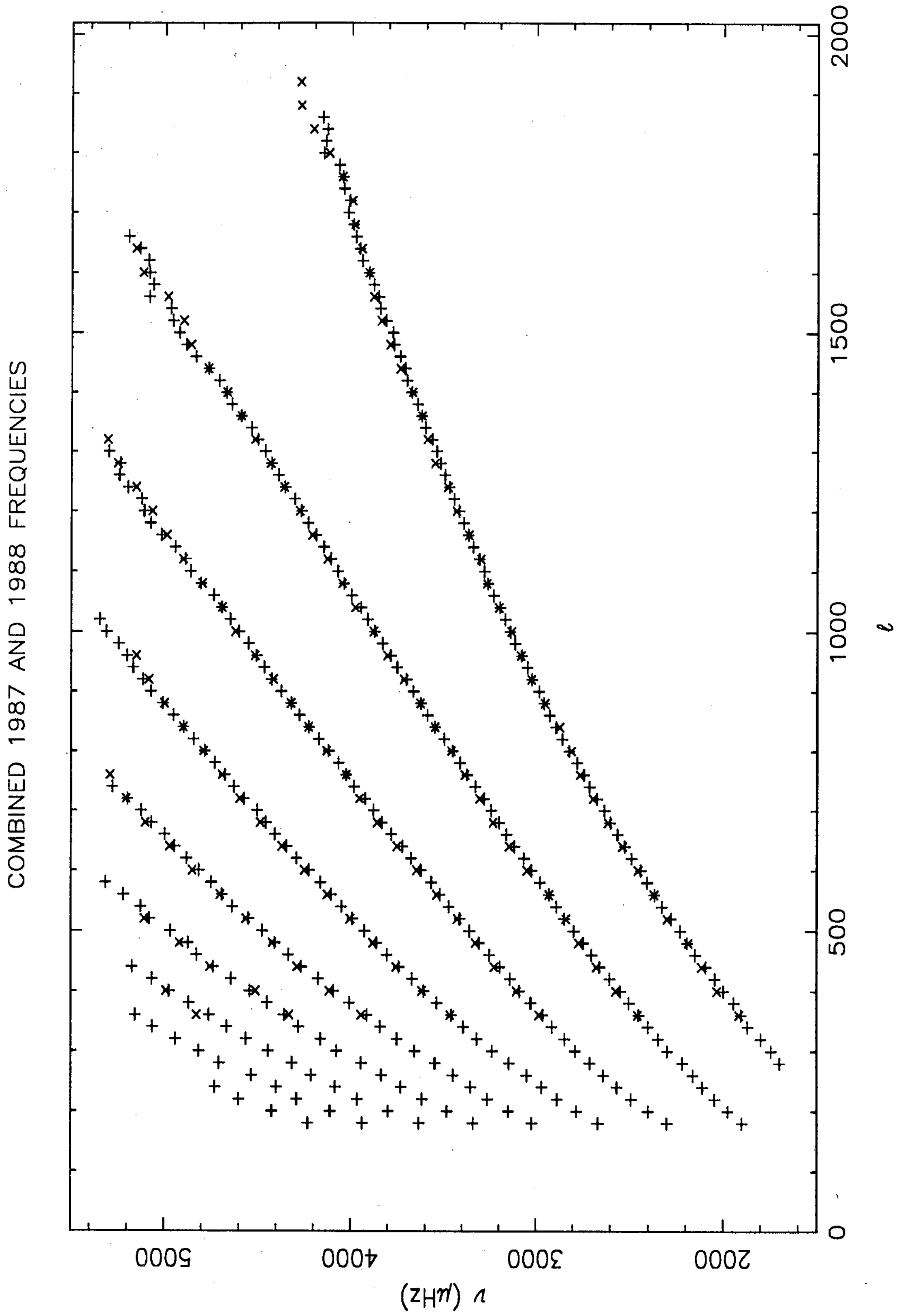
COMBINED 1987 AND 1988 FREQUENCIES
ℓ
0
500
1000
1500
2000
ν (μHz)
2000
3000
4000
5000

Fig. 3.15

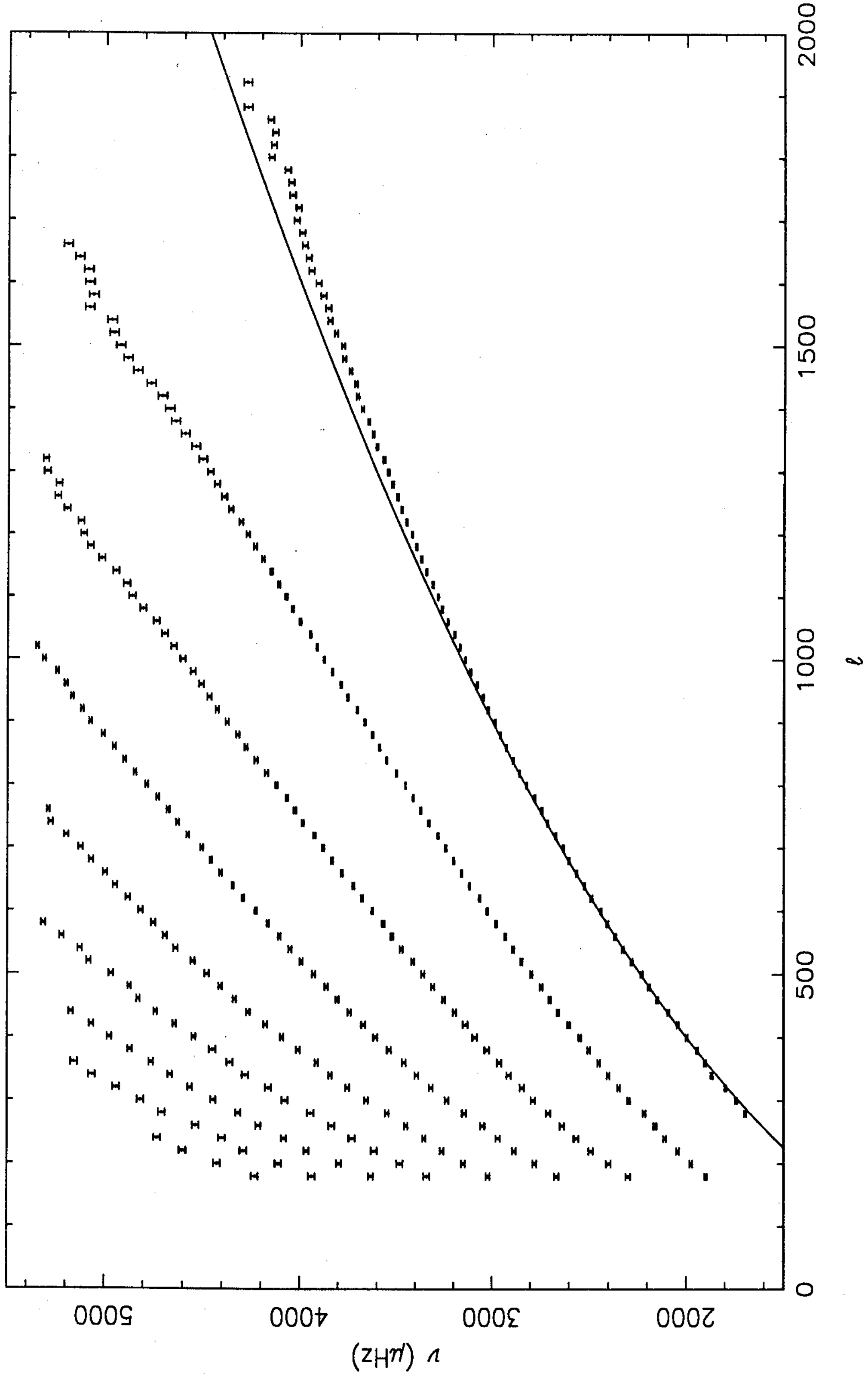

Fig. 3.16

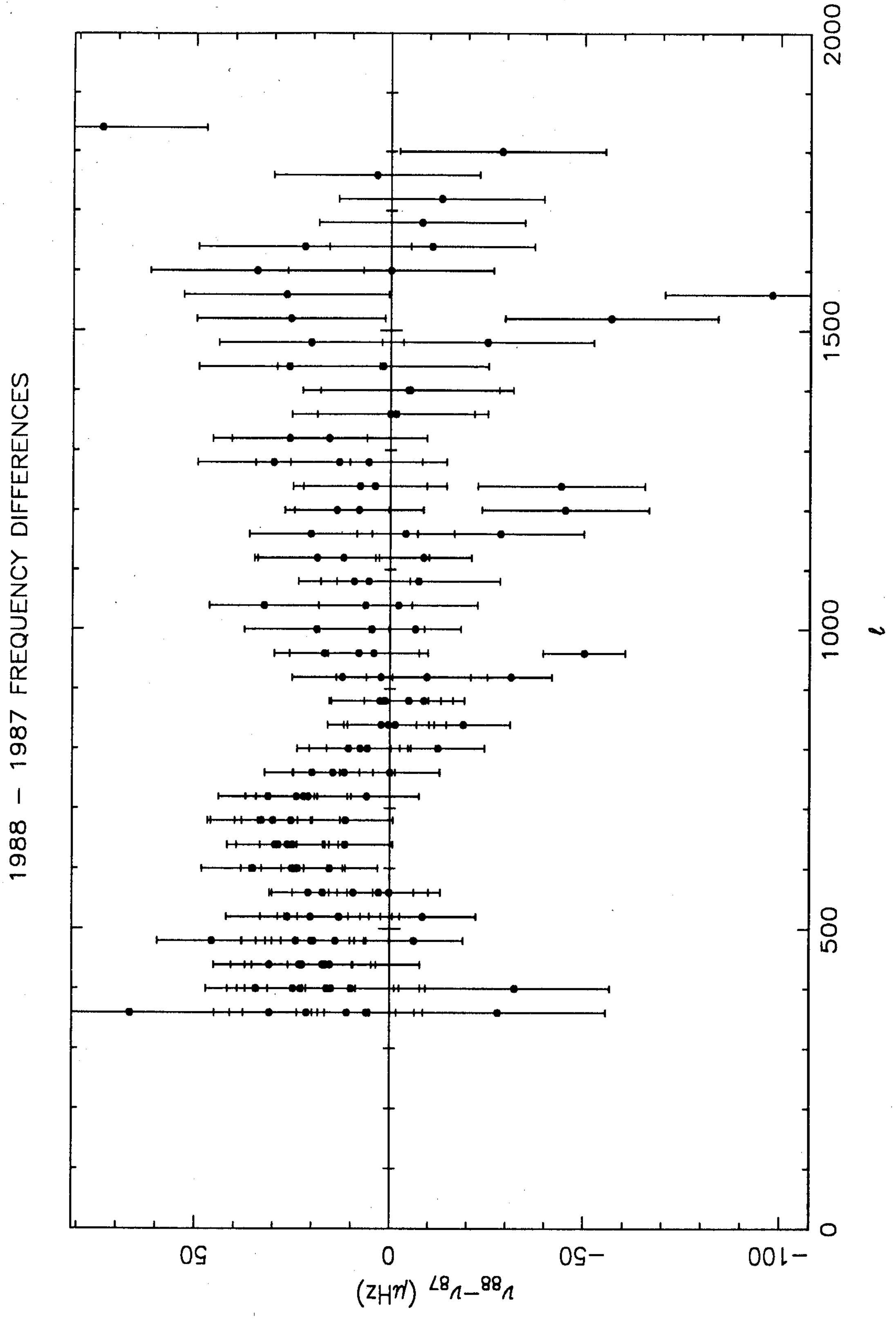
1988 – 1987 FREQUENCY DIFFERENCES
$\nu_{88}-\nu_{87}$ (μHz)
50
0
−50
−100
ℓ
0
500
1000
1500
2000

Fig. 3.17

CHAPTER 4

Amplitude Measurements

4.1 Introduction

Much work has been done in calculating the frequencies of the Sun's normal modes of vibration, and the frequencies of observed p-modes have been theoretically reproduced to within 0.5%. However, very little progress has been made in predicting the amplitudes and linewidths of the oscillations. This is a direct consequence of our lack of understanding of the excitation and damping mechanisms. As described in § 2.4, there are two main candidates for excitation mechanisms. One is that the modes are overstable because of the κ-mechanism (see Libbrecht 1988a for a review and references therein). The other more likely theory (due to Goldreich, Keeley, and Kumar) is that the modes are being stochastically excited by turbulent convection in the convection zone (Goldreich and Keeley 1977b; Goldreich and Kumar 1988, 1990). Possible damping mechanisms include radiative damping and turbulent viscous damping. (See Libbrecht 1988a and Libbrecht 1988c for reviews of this subject). One prediction of the Goldreich/Keeley/Kumar theory is that the modes are in energy equipartition with the eddies of the turbulent convection.

Some work has been done in measuring mode amplitudes and linewidths, and in particular Libbrecht (1988b) has measured mode amplitudes and linewidths for $\ell \leq 60$. Almost no accurate measurements exist for p-modes with $\ell > 60$. Libbrecht *et al.* (1986) have attempted to measure high-ℓ mode amplitudes, but their results were inconclusive because of uncertainties produced by atmospheric seeing. This is unfortunate since high-ℓ modes propagate only in the top of the convection zone, where it is thought that most of the excitation and damping occurs.

The primary difficulty in measuring mode amplitudes at high ℓ is that atmospheric seeing smears out the small spatial features associated with these modes. In this work, we have made velocity observations at the center of the solar disk, and have simultaneously measured the atmospheric modulation transfer function (MTF) in an attempt to correct for the effects of atmospheric seeing. The atmosphere can be thought of as a low-pass spatial filter. By looking at the solar limb, which, before being distorted by seeing, has a known spatial profile, we can determine the MTF of this low-pass filter. This MTF can then be used to correct the spatial power spectrum of the solar photospheric velocity field. Much of the work described in this chapter is based on, and is an extension of, work presented by Kaufman (1988).

4.2 Description of Data

In devising a method to measure the seeing we have carefully considered the words of Coulman (1985) in his article *Fundamental and Applied Aspects of Astronomical "Seeing"*:

> The reputation of a given telescope at a given site is too often a matter of opinion. Although it can be argued that objective assessment would be facilitated if astronomers regularly made and recorded quantitative measurements of image quality, it must be remembered that any appreciable sacrifice of astronomical observing time is quite unacceptable.

The data used in this work are the same as those used for the frequency measurements described in Chapter 3, with the addition of the seeing measurements that we now describe. The seeing data were collected using the same optical system and data acquisition system described in § 3.3. Throughout the course of a given observing day, at approximately 15-minute intervals, the telescope was slewed to the east limb of the Sun by the operator. The positioning of the telescope was not precise as it was moved in the "image search" mode, which uncouples the position of the telescope from the position of the telescope guider. The image search mode has the advantage that the telescope can be moved quickly, and that the previous position of the telescope (i.e., the center of the solar disk) is "stored" and therefore can be returned to quickly. Short-exposure (at video rates), 128 pixel-wide limb profiles were then acquired using the same system used to collect Dopplergrams, except that images taken in the red and blue wings were added, rather than subtracted. Each exposure resulted in the collection of four limb profiles taken from the positions shown in Fig. 4.1. It should be noted that these are not true, radial limb profiles. Corrections for this discrepancy are small and are dealt with later. Limb profiles were collected for a time approximately equal to the time it took to make one Dopplergram ($\sim$ 9 sec). This resulted in the collection of seven sets of four limb profiles every 15 minutes for the 1987 data set and nine sets of four every 15 minutes for the 1988 data set. The relevant parameters describing the two limb-profile data sets are shown in Table 4.1 (and also Table 3.1). This entire process was completed in less than a minute, and the telescope was then moved back to the center of the solar disk, so that the next Dopplergram could be made. The collection of Dopplergrams was never interrupted by the collection of limb profiles.

A typical example of one complete sample of raw limb profiles is shown in Fig. 4.2. Fig. 4.3a shows plots of one individual limb snapshot from the four different sample positions shown in Fig. 4.1. Fig. 4.3b shows an overlay of all of the limb profiles from a given sample for the four different sample positions. Note that blurring of the limb can be seen in all of these figures and that image motion is clearly indicated in Figs. 4.2 and 4.3b.

4.3 Modeling the Effect of Seeing on Solar Images

Two factors contribute to the measured seeing. The most fundamental is image blurring (or "soft seeing"). Since the Dopplergrams are integrated velocity images, image motion (or "hard seeing") also contributes to the image degradation. Note that image motion can be produced both by the atmosphere and by telescope shake. We do not differentiate between the two, since their effects on the image quality are the same. Also, we do not attempt to explain, in detail, the sources of the different types of seeing. Our goal is only to measure the MTF produced by the different types of seeing and to use it to correct the more important velocity data set.

Table 4.1

Limb Profile Observational Parameters

Date	1987 July 23	1988 July 19
Time (UT)	14:45–00:59	14:18–20:28
No. of profiles per sample	28	36
No. of samples	41	40
Total no. of profiles	1148	1440
Horizontal image scale, S_H	0.536″/pixel	0.273″/pixel
No. of pixels	128	128
Profile size	68.6″	34.9″
Qualitative seeing	fair	good

In this work, we have modeled the effects of atmospheric seeing on the profile of the limb (or the spatial characteristics of the solar surface velocity field) as being given by the convolution of a point spread function (PSF) and the spatial profile of the true limb (or true velocity field). That is, the observed limb profile, $\mathcal{L}(x)$, is related to the true (or theoretical) limb profile, $L(x - x_0)$ (which has been smeared, or blurred, by a model PSF; $S(x)$) by

$$\mathcal{L}(x) = \int_{-\infty}^{+\infty} L(x' - x_0) S(x - x')\, dx', \tag{4.1}$$

where x is the horizontal image coordinate, and x_0 is an arbitrary offset of the limb position. The PSF used in this work is the sum of two Gaussians given by

$$S(x) = \frac{1}{1+\alpha}[S_1(x) + \alpha S_2(x)], \tag{4.2}$$

where $S_i(x)$ is a standard, normalized Gaussian function of width σ_i:

$$S_i(x) = \frac{1}{\sqrt{2\pi\sigma_i^2}} e^{-x^2/2\sigma_i^2}. \tag{4.3}$$

We have assumed that $\sigma_2 \gg \sigma_1$, and $\alpha < 1$, i.e., that the PSF is composed of a narrow, large-amplitude Gaussian and a wide, small-amplitude Gaussian. The latter Gaussian is probably due to scattered light in the optics. The choice of Eq. (4.2) as our PSF is dealt with in more detail in Chapter 5. The theoretical limb profile, $L(x)$, is that of Pierce and Waddell (1961) with an arbitrary multiplicative intensity parameter, I_0:

$$L(\mu) = I_0 \left\{ a + b\mu + c\left[1 - \mu \ln\left(1 + \frac{1}{\mu}\right)\right]\right\}, \tag{4.4a}$$

where $a = 0.81999$, $b = 0.34918$, $c = -0.55132$ (chosen for $\lambda = 6400$ Å), and $\mu = \cos\theta$, where θ is the angle between the direction to the observer and the normal to the solar surface. Alternatively, this can be expressed in terms of $x = R_\odot \sin\theta$ as

$$L(x) = I_0 \left\{ a + b\sqrt{1 - \frac{x^2}{R_\odot^2}} + c\left[1 - \sqrt{1 - \frac{x^2}{R_\odot^2}} \ln\left(1 + \frac{1}{\sqrt{1 - \frac{x^2}{R_\odot^2}}}\right)\right]\right\}. \tag{4.4b}$$

The dashed curve in Fig. 4.4 shows this limb-darkening curve in the vicinity of the limb. Of course, the profile of the undistorted limb is not truly known, but, because our pixel size (0.27–0.54″) is larger than the apparent scale height of the solar atmosphere ($H = 100$ km $\approx 0.14''$), we can say that the profile is known to the accuracy of our measurements. Also, there were a number of possible choices for the form of the true limb profile. Most limb models agree quite nicely at any appreciable distance from the limb—the differences appear only when $x \approx R_\odot$ ($\mu \approx 0$). In summary, the choice of the form of the true limb profile is not too critical so long as limb darkening is adequately modeled. Fig. 4.5 shows a typical example of the PSF used here, and the solid curve in Fig. 4.4 shows an example of our true limb profile smeared by this PSF.

4.4 Measuring the Seeing: Limb Fitting

Each observed limb profile, $\mathcal{L}_\odot(x)$, was fit to the smeared limb model

$$\mathcal{L}_\odot(x) \to \int_{-\infty}^{+\infty} L_\odot(x' - x_0) S(x - x')\, dx', \tag{4.5}$$

where $L_\odot(x)$ is given by

$$L_\odot(x) = \begin{cases} L(x) & \text{if } x < R_\odot; \\ 0 & \text{if } x \geq R_\odot, \end{cases} \tag{4.6}$$

and where $L(x)$ is given by Eq. 4.4b. The following five parameters were fit for: $I_0, \sigma_1, \sigma_2, \alpha$, and x_0. The nonlinear, least-squares fits were accomplished using the Levenberg-Marquardt method described in Press *et al.* (1986). Calculating the fit was not a trivial task because integrals of the form

$$I_n = \int_{-\infty}^{+\infty} L_\odot(x' - x_0) S_i(x - x') \left(\frac{x - x'}{\sqrt{2}\,\sigma_i} \right)^n dx', \qquad n = 0, 1, 2 \tag{4.7}$$

were needed to evaluate the fit, and these integrals cannot be evaluated analytically. Numerical integration of the integrals was unsatisfactory because of the rapid change in $L(x)$ at the limb. Because of this, very fine grids, and hence, large amounts of CPU time, were needed to accurately evaluate the integrals. By using the Fourier transform convolution theorem to aid in evaluating the integrals, we found that accuracy could be maintained while minimizing CPU time. A typical fit to Eq. (4.5) is shown in Fig. 4.6.

Of the five parameters that have been fit for, the second through fourth are functions of image blurring ("soft seeing"), and the last is related to image motion ("hard seeing"). For a given sample of 28 or 36 limb profiles, the fit parameters were averaged, and corrections were then made for small $\cos\theta$ effects resulting from the nonradial nature of the limb profiles on the four sets of averaged parameters. The five averaged and corrected parameters from one limb sample position (for the 1987 data set), $I_0, \sigma_1, \sigma_2, \alpha$, and σ_{x_0} are shown, as a function of time, in Fig. 4.7. It should be noted that any of the parameters σ_1, σ_2, or α taken separately, as a function of time, are not indicative of the seeing. These parameters must be viewed collectively (through the MTF) to fully understand the seeing. Finally, the averaged and corrected parameters were, again, averaged over the four limb positions. Image motion was included as time-integrated image blurring by allowing

$$\sigma_i^2 \rightarrow \sigma_i^2 + \sigma_{x_0}^2, \tag{4.8}$$

where σ_{x_0} is the RMS deviation from the mean of x_0. This process resulted in four parameters that describe the seeing at a given moment. Typical values for these parameters were found to be $\sigma_1 \sim 1.7''$, $\sigma_2 \sim 18''$, $\sigma_{x_0} \sim 0.5''$, and $\alpha \sim 0.3$. These combine to give the PSF a full width at half maximum (FWHM) of $\sim 4''$ as shown in Fig. 4.5. Note that atmospheric blurring and motion, telescope shake, telescope optics, and image focus contribute to this PSF.

4.5 The Modulation Transfer Function (MTF)

The MTF is the Fourier transform of the PSF. Therefore, the amplitude MTF (as a function of spherical harmonic degree, ℓ) is

$$\mathrm{MTF}(\ell) = \frac{1}{1+\alpha}\left[e^{-(\sigma_1^2+\sigma_{x_0}^2)\ell^2/2R_\odot^2} + \alpha e^{-(\sigma_2^2+\sigma_{x_0}^2)\ell^2/2R_\odot^2}\right]. \tag{4.9}$$

With the limb profile fit parameters as a function of time, we were able to produce $\mathrm{MTF}(\ell, t)$, the MTF as a function of time, for the two data sets as shown in Figs. 4.8a and b. The MTFs, averaged over the entire day, are shown in Figs. 4.9a and b. From these plots, one can see that the morning seeing was better in 1988 than in 1987, and that at the lower-ℓ values, the seeing worsened throughout the course of both days. Furthermore, 1988 had better overall seeing than 1987. All of these conclusions agree with the qualitative observations of the experienced BBSO observing staff that were made at the time the data were collected. The MTFs with 15-minute sample intervals were interpolated using a cubic spline to get MTFs with regular one-minute sample intervals. These were used in the seeing correction.

4.6 Correcting the k_h-ω Diagram with the MTF

The correction for the effects of seeing occurs during the calculation of the k_h-ω diagram. For the most part, the corrected k_h-ω diagram is calculated in the same manner as described in § 3.6. Starting with the "perfect" data set described in § 3.5, a two-dimensional spatial Fourier transform was performed on each image, thereby turning the data set into a k_x-k_y-t diagram. We then assumed that the MTF, which was measured in the horizontal, or x, direction, is also valid in the vertical direction because the atmospheric seeing qualities are assumed to be locally isotropic. At each point at k_h, given by Eq. (3.3), on each time slice of the k_x-k_y-t diagram, we divided by the appropriate value of MTF(ℓ, t). This is the seeing correction. As in § 3.6, a best-fit linear background was subtracted from each corrected time series of spatial-frequency components, and temporal Fourier transforms were performed on each time series. This procedure resulted in a k_x-k_y-ω diagram that has been corrected for the effects of atmospheric seeing, and is illustrated schematically in Fig. 4.10. Next, we calculated the power spectral density from the k_x-k_y-ω diagram.

The seeing-corrected k_x-k_y-ω diagram was then corrected for the effects of solar rotation using the value of $\dot{\nu}_\odot$ found in § 3.6 for the uncorrected data sets. Finally, we integrated the k_x-k_y-ω diagram along circles of constant k_h to get a k_h-ω diagram. Fig. 4.11 shows the uncorrected and corrected k_h-ω diagrams for 1987; Fig. 4.12 shows them for 1988. There are two important points to note in these figures. Firstly, in the corrected k_h-ω diagrams, the power in the oscillations does not drop off as strongly with ℓ as it does in the uncorrected diagrams. This is a result of the seeing correction. Secondly, at high ℓ, the power increases dramatically. This is due to the breakdown of the seeing correction. That is, at very high ℓ, the MTF has very small values (~ 0.1 at $\ell = 1200$), and the effect of any errors in the MTF is magnified when the spatial power spectra are divided by the MTF. Furthermore, note that ridges can be seen out to slightly higher ℓ in the 1988 corrected k_h-ω diagram than in 1987. This correlates with the better seeing in the 1988 data set.

4.7 Power Measurements: Ridge Fitting

The velocity power in each ridge was measured using the same ridge-fitting technique described in § 3.7. The background parameters ν_B and σ_B were fixed using the same values used in making the seeing-uncorrected fits. The velocity power in the ith ridge, $P_{v,i}$, is the integral of the appropriate Gaussian or

$$P_{v,i} = A_i\sqrt{\pi\sigma_i^2}, \tag{4.11}$$

where A_i and σ_i are identified in Eq. (3.4). Ridge frequencies were also measured, but they were not corrected for the systematic effects described in § 3.7. For each ridge, the measured powers were smoothed, as a function of ℓ, to remove high-frequency components. Similar power measurements for the uncorrected data sets were also made. From here on we shall be concerned with displaying the power measurements in a useful fashion, and with interpreting the results.

4.8 Contour Plots of Power in the ℓ-ν Plane

A useful way of looking at mode power would be a way that gives an overall picture of the excitation and damping mechanisms, irrespective of the frequency spectrum in the ℓ-ν plane. That is, the loci of the mode frequencies in the ℓ-ν plane are determined only by the solar model, and, for small changes in the solar model, a different frequency spectrum will result, even assuming that the same excitation and damping mechanisms are at work. Given this point of view, mode powers are best viewed in terms of a power contour plot in the ℓ-ν plane. Unfortunately, the generation of such a plot is somewhat difficult, primarily because of the nonuniform distribution of data points in the ℓ-ν plane. We shall describe here the procedure used in creating the power contour plots, shown in Figs. 4.13, and 4.14, for the two data sets. The numbers demarcating the ridge positions in these figures are the smoothed velocity power measurements described above. For the purposes of evaluating the effect of the seeing correction, both the uncorrected and corrected contour plots are shown in these figures.

The first step in generating contours was to create boundary conditions at $\ell_{\min}$, $\ell_{\max}$, $\nu_{\min} = 1.5$ mHz, and $\nu_{\max} = 5.5$ mHz (i.e., the four ℓ and ν extremes of the ℓ-ν diagram). This was necessary so that contours could be generated outside the convex envelope described by the available points in the ℓ-ν plane. In other words, since the heart of any contour-plotting algorithm is some method of interpolation, it was necessary to provide data at the extreme regions of the ℓ-ν plane so that the interpolation could be carried out (as opposed to an extrapolation). However, we should point out that our solution to this problem was, in fact, to extrapolate (intelligently) into these regions, albeit using methods different from those that generate the interpolations for the contours. As such, we created boundary conditions by extrapolating the available powers out to the borders of the ℓ-ν plane. Specifically, we assumed that the velocity power could be written as a separable function of ℓ and ν; i.e.,

$$P_v(\nu, \ell) \approx P_{\max} N(\nu) \Lambda(\ell), \tag{4.12}$$

where $N, \Lambda \in [0, 1]$ as in Libbrecht *et al.* (1986). We then calculated $\Lambda(\ell)$ by averaging the data over all ν and smoothing the result. $N(\nu)$ was calculated by averaging the data over the the first few available ℓ-values and doing a polynomial fit to the resulting average. The polynomial fit was used to generate $P_v(\nu, \ell_{\min})$ at all frequency grid points. $P_v(\nu_{\min}, \ell)$ and $P_v(\nu_{\max}, \ell)$ were generated using $\Lambda(\ell)$ scaled to the appropriate power values from the above polynomial fit. Finally, $P_v(\nu, \ell_{\max})$ was generated using interpolated values from a linear fit to the logarithm of the $\ell = \ell_{\max}$ data points (including the ones created at $\nu_{\min}$ and $\nu_{\max}$). These boundary data points, along with the actual data points, were used as inputs for generating the interpolations for the contours.

The method used for bivariate interpolation of a nonuniform distribution of data points is described in Lawson (1977). Briefly, this method involves first partitioning the data points into a triangular grid. Triangles are selected using the so-called max-min angle criterion; that is, for any convex quadrilateral, divide it into two triangles such that the minimum interior angle of the two triangles is maximized. Next, a bivariate linear interpolation is performed in the triangular region. Using this method, a uniform grid of points can be generated. The particular implementation of this algorithm used here is the one contained in the NCAR Graphics subroutine CONRAN (Clare, Kennison, and Lackman 1987). Although this subroutine does both interpolation and contour plotting, we used only the interpolation portion because of the unsuitable nature of the contour plots. It was necessary to delve into the NCAR software and extract the interpolated points so that they could be used for other purposes. The actual contour plotting was accomplished using standard methods for a rectangular grid of points. The final results are shown in Figs. 4.13a and b for 1987, and in 4.14a and b for 1988. Note that the contours for the uncorrected data sets are not shown for frequencies below the f-mode frequencies. This is a result of a failure of the interpolation algorithm to generate meaningful interpolations in these regions. However, this is not a great loss, since the corrected data sets are the ones of interest. Also, note that the inter-ridge velocity power depicted by the contours should not be interpreted literally. These contours serve only to give a rough picture of the excitation and damping mechanisms, irrespective of the exact solar model used to generate the mode frequency spectrum.

4.9 Peak Velocity Power and Frequency of Peak Velocity Power

The peak velocity power as a function of ℓ, $P_{v,\mathrm{max}}(\ell)$, and the associated frequency of the peak, $\nu_{\mathrm{max}}(\ell)$, were found from the interpolated data used to make the contour plots. That is, for each ℓ, the maximum power and associated frequency were located. In terms of the approximation given in Eq. (4.12), $P_{v,\mathrm{max}}(\ell) = P_{\mathrm{max}}\Lambda(\ell)$, however, this approximation was not used in measuring $P_{v,\mathrm{max}}(\ell)$. The frequency of the peak power cannot be described in terms of this approximation, since it assumes that the frequency of the peak power is, by definition, not a function of ℓ. Figs. 4.15a and b show $P_{v,\mathrm{max}}(\ell)$ for the two data sets. Also shown are the same quantities as derived from the seeing-uncorrected data sets so that the effects of the seeing correction can be seen. Figs. 4.16a and b show $\nu_{\rm max}(\ell)$, as derived from the seeing-corrected data only, for the two different years. By fitting a straight line to $\nu_{\rm max}(\ell)$ we find that

$$\nu_{\rm max}(\ell) = 3140 + 0.316\ell \ \mu{\rm Hz} \tag{4.13a}$$

for 1987, and for 1988 we get

$$\nu_{\rm max}(\ell) = 3198 + 0.266\ell \ \mu{\rm Hz}. \tag{4.13b}$$

We know of no explanation for any functional dependence of $\nu_{\rm max}$.

The kink in the 1988 $P_{v,{\rm max}}(\ell)$ curve at $\ell \approx 475$ is due to an imperfection in the interpolation algorithm described in § 4.8. The problem occurred in the choice of boundary conditions at $\ell_{\rm min}$. A peak in the velocity power (as a function of ν) occurred at a slightly higher value of ℓ. However, the corresponding peak was missing in the $\ell = \ell_{\rm min}$ cut through the ℓ-ν plane because no mode was present at that point. Therefore, we underestimated the value of the peak velocity power at $\ell_{\rm min}$ and slightly misidentified the position of the peak. This error in the boundary points affects the interpolation, which, in turn, affects the peak power measurement.

4.10 Velocity Power as a Function of Frequency

Since $\nu_{\rm max}$ is a function of ℓ, it is reasonable to look for other ℓ-dependent effects in the velocity power as a function of frequency. In other words, if we resort to the approximation given by Eq. (4.12), we want to look for possible ℓ-dependencies in $N(\nu)$. (Of course, any ℓ-dependencies in $N(\nu)$ render unnecessary the approximation given by Eq. (4.12).) This information is already contained in the contour plots shown in Figs. 4.13 and 4.14, although the effects may not be immediately obvious. Instead, we show the velocity power as a function of frequency (averaged over different ranges in ℓ) in Figs. 4.17a and b, for the two different years. These curves are based on the smoothed velocity power measurements described in § 4.7, i.e., the data used in generating the contour plots described in § 4.8. The velocity power measurements were binned in frequency and averaged over three different ranges in ℓ: $100 \leq \ell \leq 400$, $400 \leq \ell \leq 700$, and $700 \leq \ell \leq 1000$. The averaging over a relatively narrow range in ℓ has the effect of producing semi-continuous curves. If not for the averaging, the curves would be sparsely populated with data points because of the ridge structure in the ℓ-ν plane. The ℓ-dependency in ν_{max} is clearly seen as a shift in the peaks of the different curves. Other than the shift in the peaks of the curves, there appears to be no other major ℓ-dependent effects in the velocity power as a function of frequency; i.e., the different curves have essentially the same slopes in the low- and high-frequency regimes. The astute reader will, however, notice a slight difference in the high-frequency slopes, but this is probably due to a poor signal-to-noise ratio in this regime.

Overall, these measurements agree with similar measurements made by Libbrecht *et al.* (1986). This is a valid comparison even though their measurements were made using data that was not corrected for the effects of seeing. Atmospheric seeing only affects the results in terms of the spatial frequency dependence, not the temporal frequency dependence. It should be noted that this is not the most ideal way of looking at the data because averaging over ℓ tends to smear out features in the curves. These plots are presented only for the simplicity with which they can be viewed.

4.11 Low-ℓ Velocity Power Measurements

Other measurements by Libbrecht *et al.* (1986) show that $P_{v,\mathrm{max}}(\ell)$ appears to have a peak at $\ell \approx$ 100–300, or at least a plateau below this range. Unfortunately, this is exactly where our velocity power data derived from ridge fitting ends. We therefore investigated other means of measuring $P_{v,\mathrm{max}}(\ell)$ at lower values of ℓ. We shall describe here those methods and the results of our investigation.

We focused on the data contained in the $S_k(\nu)$ power spectra, i.e., the original k_h-ω diagram. However, before the low-ℓ (or low-k) data could be used, two major corrections had to be performed. First, we subtracted the known background (described by A_B, ν_B, σ_B, and C in Eq. 3.4) from the $S_k(\nu)$. Since we had these background parameters only down to $\ell_{\rm min}$, and since we wanted to go down as low as possible in ℓ, it was necessary to extrapolate the background parameters down to $\ell = d\ell/dk$ (or, $k = 1$). As will be seen below, we could not go down to $\ell = 0$ ($k = 0$). As seen in Fig. 3.8, we found it reasonable to use extrapolations of linear fits for ν_B and σ_B, and extrapolations of linear fits to the logarithms of A_B and C. Values of these four background parameters derived from the fits were actually used for the first few power spectra above $k_{\rm min}$. With these extrapolated values, linear-fit values, and values from the actual ridge fitting in hand, we subtracted the Gaussian background and the constant background offset from the k_h-ω diagram. One should be reminded to treat any $\ell \leq \ell_{\rm min}$ result from this procedure with a certain degree of suspicion because of the use of the extrapolated background parameters.

The second correction needed before $P_{v,{\rm max}}(\ell)$ could be calculated was a result of the subtraction of a best-fit planar background from each Dopplergram (as described in § 3.5). This subtraction has the effect of filtering the spatial-frequency power spectrum of each Dopplergram, and, hence, the spatial-frequency response of the k_h-ω diagram. In correcting for this effect, we have considered only the one-dimensional analog, i.e., the frequency response of a best-fit linear subtraction from a sinusoid with frequency k. We have derived the modulation transfer function for such a filter in Appendix II. The MTF for the spatial-frequency component index k (of the k_h-ω diagram) as a function of spatial frequency index j is

$$\mathrm{MTF}_k(j) = \left(1 - \frac{6}{\pi^2 jk}\right)\delta_{jk} + \frac{18}{\pi^4 j^2 k^2}. \qquad (4.14)$$

Since this MTF is a two-dimensional function, there is a leakage from one spatial-frequency component of the k_h-ω diagram to another. That is, after subtracting a best-fit line from a sinusoid of frequency k, which has a delta function power spectrum, the result no longer has a delta function power spectrum. The resulting spectrum is contaminated with power from nearby sinusoids. Fig. 4.18a shows the diagonal, or $j = k$, term of the MTF. The MTF is essentially unity, except for the first few components. Plotting the ratio of the first off-diagonal to diagonal terms, or $\mathrm{MTF}_{k+1}(k)/\mathrm{MTF}_{k+1}(k+1)$, in Fig. 4.18b, we see that the off-diagonal terms are essentially negligible. Therefore, we have approximated the actual nondiagonal MTF with a diagonal MTF consisting of the original diagonal terms, or

$$\mathrm{MTF}_k(k) = 1 - \frac{6}{\pi^2 k^2} + \frac{18}{\pi^4 k^4}. \tag{4.15}$$

Therefore, the second correction to the k_h-ω diagram consists of dividing the kth spatial-frequency component by $\mathrm{MTF}_k(k)$.

With the k_h-ω diagram now completely corrected for background and systematic effects, we are able to begin the low-ℓ velocity power measurements. The analysis is, again, based on the approximation that the velocity power in the k_h-ω diagram is separable in k_h and ω, as in Eq. (4.12). Given this approximation, we note that the average power in a given frequency band, as a function of ℓ, should have the same functional dependence as $P_{v,\max}(\ell)$. Therefore, $P_{v,\max}(\ell)$ can be calculated by integrating the velocity power over a given range in frequency (in this case $2.0\,\mathrm{mHz} \leq \nu \leq 4.0\,\mathrm{mHz}$), and then dividing by the number of ridges in this range. The number of ridges in the given frequency range was determined by counting, using the frequency data set in Libbrecht, Woodard, and Kaufman (1990). However, this counting procedure results in a noncontinuous, integrally varying function. To overcome this drawback, we fit a 7th-order polynomial to the ridge count. Results of the counting procedure and the fit are shown in Fig. 4.19. Fitting a polynomial to the ridge count also has the added benefit that it compensates for the fact that partial ridges were included in the integration over frequency. That is, the ridges in the k_h-ω diagram have finite widths, and integrating over a fixed range in frequency may select only fractions of certain ridges. Fractional values of the fitted ridge count then compensate for fractional ridges in the frequency integral. An arbitrary scaling factor of about 2 was needed to make the low-ℓ power agree with the high-ℓ power. Figs. 4.20a and b show $P_{v,\max}(\ell)$ for 1987 and 1988, respectively, as calculated by the high-ℓ ridge-fitting method and the low-ℓ integration method. Also shown are the same quantities for the data without the seeing correction. One can see that there is very good agreement in the region of overlap between the two methods. Also, at very low ℓ the seeing-uncorrected and seeing-corrected data converge, as one would expect, since the atmospheric MTF is approximately 1 in this region. Furthermore, and most importantly, we see that the data from both years exhibit the expected peaks at $\ell \approx 100$–300.

4.12 Comparison of 1987 and 1988 Results

In comparing the velocity power results from the two different years, we see that the two $P_{v,\mathrm{max}}(\ell)$ curves exhibit the same gross characteristics, but that the specifics are different. Fig. 4.21 shows $P_{v,\mathrm{max}}(\ell)$ for 1987 and 1988 plotted together. Here, we have used the low-ℓ values from the analysis described in § 4.11 and the high-ℓ values from the analysis described in § 4.9. (For the 1988 curve, we have replaced the first four points of the high-ℓ ridge-fit section of $P_{v,\mathrm{max}}(\ell)$ with four points from the low-ℓ integrally produced $P_{v,\mathrm{max}}(\ell)$. This lessens the effect of the systematically produced kink at $\ell \approx 475$ described in § 4.9.) The two curves have been scaled such that the areas under the curves between $\ell = 40$ and $\ell = 400$ are the same. This comparison range was chosen because first, there are essentially no data below $\ell = 40$ (actually, below $\ell \approx 20$ for 1987 and $\ell \approx 40$ for 1988), and second, it is at low ℓ that we would expect $P_{v,\mathrm{max}}(\ell)$ to be most free from any possible systematic effects induced by the seeing correction. Furthermore, as ℓ increases, the seeing correction will, at some point, break down, presumably at a lower value of ℓ for 1987 than for 1988, since the seeing was worse in 1987. A value of $\ell = 400$ was judged to be a good compromise between wanting high ℓ for good comparison, and avoiding the region in which the seeing correction might break down.

Excluding any possible solar cycle effects, we would expect $P_{v,\mathrm{max}}(\ell)$ to be the same for both 1987 and 1988. However, there are distinct differences. Both curves exhibit the same positive slope at low ℓ, but the curves are offset in this region. In each case, $P_{v,\max}(\ell)$ then peaks out, albeit at different values of ℓ: $\ell \approx 170$ for 1987 and $\ell \approx 300$ for 1988. Finally, the two curves gradually decay to about the same value at $\ell \approx 800$. However, at this point the 1987 curve exhibits a rapid increase. This is a result of the poorer seeing in 1987, and, hence, the seeing correction breaks down at an earlier ℓ. If we had shown higher values of ℓ, the 1988 curve would also show the same rapid increase, except that it would begin at a higher value of ℓ. In fact, for $\ell \gtrsim 1100$, the 1988 curve does start to show a mild increase, i.e., the beginnings of the seeing-correction breakdown.

Given that the data from the two years exhibit enough relative similarities, and that some of the key differences can be explained, we have found it advantageous to average the results from the two years. Fig. 4.22 shows $P_{v,\max}(\ell)$ averaged over the two years. To do this, we first used a cubic spline to interpolate the two individual curves onto an integrally spaced grid with a spacing of $\Delta\ell = 10$. These two data sets were then averaged to get the curve in Fig. 4.22, except that beyond $\ell = 810$, we did not use the average, and instead used only the data from 1988. The error band is a constant width out to $\ell = 810$, at which point it increases exponentially to $\ell = 1200$, where it has a value 50% greater than the constant value. The constant error was determined by first smoothing the standard deviations of the averages, and then averaging the smoothed errors to get the final value.

4.13 Discussion

If we assume that the modes are excited by stochastic interactions with turbulent convection, then the energy in a mode is given by Eq. (2.27), which is repeated here:

$$E = M_v P_v. \tag{4.16}$$

Furthermore, if we assume that the oscillations are in energy equipartition with the exciting convective eddies, and if we also assume that the convective eddy energy is constant in the frequency range of interest, then E will be constant, and hence, $P_v \propto M_v^{-1}$. In Fig. 4.22, we have also plotted $M_v^{-1}(\ell)$ for $\tau_{5000} = 0.05$. This was created from mode masses calculated by Kumar (1990), using a model from Christensen-Dalsgaard and Berthomieu (1991). These mode masses were interpolated in the ν direction using a cubic spline, and then masses corresponding to frequencies of the measured peak velocity power (i.e., $\nu_{\max}$ given in Eq. (4.13a)) were selected to give the curve in Fig. 4.22. We see that there is very good agreement between our observations and $M_v^{-1}(\ell)$ for $\ell \lesssim 200$. Kumar, Franklin, and Goldreich (1988) have calculated this result, assuming that the oscillations are in energy equipartition with the turbulent convection.

If the energy in a given mode is $E_{n\ell m}$, then the energy in a given multiplet is $E_{n\ell} = \sum_m E_{n\ell m} \approx (2\ell + 1)E_{n\ell 0}$, and the peak energy as a function of ℓ is $E_{\max}(\ell) = \max(E_{n\ell})$. $E_{\max}(\ell)$ is, of course, directly related to $P_{v,\max}(\ell)$. In Fig. 4.23, we show the peak energy, $E_{\max}(\ell)$, assuming that the energy is given by Eq. (4.16). Since we have measured only the relative velocity power, we have scaled these results to full-disk Dopplergram, $\ell = 20$, $\nu = 3.20$ mHz mode energy measurements in Libbrecht (1988b). Kumar and Goldreich (1989) find that $E_{\max}(\ell)$ will decrease at higher values of ℓ; however, the exact quantitative dependence is determined by the assumed damping mechanism, or mechanisms.

The total energy in all modes of degree ℓ, $E_\ell = \sum_n E_{n\ell}$, can be calculated using the approximation in Eq. (4.12), $E_{\max}(\ell)$, $N(\nu)$, and a table of mode frequencies. Using the frequencies in Libbrecht, Woodard, and Kaufman (1990), Fig. 4.24 shows E_ℓ, calculated for the range $1.5\,\mathrm{mHz} \le \nu \le 5.5\,\mathrm{mHz}$, and that the total energy in all oscillations peaks at $\ell \sim 170$.

Finally, the total energy in solar p- and f-modes, $E_{\mathrm{tot}} = \sum_\ell E_\ell$, can be found by integrating the curve in Fig. 4.24. However, as a prerequisite to that, we show the cumulative total energy, $E_{\mathrm{cum}}(\ell) = \sum_{\ell'=0}^{\ell} E_{\ell'}$, in Fig. 4.25. Since $E_{\mathrm{cum}}(\ell)$ does not quite converge to a constant value, there is, clearly, some remaining energy in the modes above $\ell = 1200$. However, extrapolating $E_{\mathrm{cum}}(\ell)$ out to higher ℓ, we can conclude that $E_{\mathrm{tot}} \gtrsim 6 \times 10^{33}$ ergs. Therefore, the total energy contained in solar

p-modes is about equal to the total energy radiated by the Sun in 1.5 seconds.

Figure Captions

Figure 4.1: A schematic showing the positions on the solar disk where the limb profiles were collected. Short exposure (at video rates), 128 pixel-wide limb profiles were taken at these four positions.

Figure 4.2: Typical example of one complete sample of limb profiles from the four positions shown in Fig. 4.1. There are nine profiles from each of the four positions, giving a total of 36 limb profiles. These data are from 1988. Image blurring and image motion are visible in this picture.

Figure 4.3: (a) Plots of the individual limb snapshots from the four different positions shown in Fig. 4.1. This corresponds to one scan line in Fig. 4.2. (b) An overlay of all of the limb profiles from a given sample for the four positions shown in Fig. 4.1. As in Fig. 4.2, image blurring and image motion are both depicted here.

Figure. 4.4: The theoretical, or true, limb profile and a blurred limb profile. The dashed curve shows the true limb-darkening curve, $L_\odot(x)$, given by Eq. (4.6), in the vicinity of the limb. The solid curve shows the blurred limb-darkening curve, $\mathcal{L}_\odot(x)$, given by Eq. (4.1) and the point spread function (PSF) given in Eq. (4.2).

Figure 4.5: A typical example of the PSF given by Eq. (4.2). The PSF consists of a narrow, large-amplitude Gaussian, and a wide, small-amplitude Gaussian.

Figure 4.6: A typical limb profile (thin line) and the fit (thick line). The fit is to Eq. (4.5).

Figure 4.7: The averaged, corrected limb fit parameters from one of the four limb sample positions (shown in Fig. 4.1) for the 1987 data set, where the image scale is 0.536″/pixel. From the top down, the curves are: 1) I_0 (dashed line) measured in relative units (the morning-to-evening intensity variation is due to changes in the sky transparency that coincide with the motion of the Sun); 2) σ_2 (solid line)

measured in pixels; 3) σ_{x_0} (dot-dashed line) measured in pixels; 4) σ_1 (solid line) measured in pixels. 5) α (dashed line) measured in absolute dimensionless units. Taken separately, any of these five quantities as a function of time are not completely indicative of the seeing. The seeing can be interpreted only through the modulation transfer function (MTF).

Figure 4.8: The MTF shown as a function of spatial frequency (or spherical harmonic degree ℓ) and time. This is Eq. (4.9). (a) The MTF for 1987. (b) The MTF for 1988. The morning seeing in 1988 was better than in 1987, and for both years, the seeing worsened throughout the the course of the day.

Figure 4.9: The MTF averaged over the entire day. (a) The average MTF for 1987. (b) The average MTF for 1988. Overall, the seeing was better in 1988 than in 1987. This agrees with the qualitative observations of the experienced BBSO observing staff.

Figure 4.10: A schematic illustrating the calculation of the corrected k_x-k_y-ω diagram from a time series of Dopplergrams and the MTF.

Figure 4.11: The uncorrected and corrected ℓ-ν power spectra diagrams for the 1987 data. Note that the power drops off much more rapidly with ℓ in the uncorrected diagram than in the corrected diagram. The very rapid power increase at high ℓ in the corrected diagram is due to the breakdown of the seeing correction.

Figure 4.12: The uncorrected and corrected ℓ-ν power spectra diagrams for the 1988 data. Note that the seeing-correction breakdown occurs at a higher ℓ here than for the 1987 ℓ-ν power spectrum diagram (Fig. 4.11). This correlates with the seeing being better in the 1988 data set.

Figure 4.13: (a) A contour plot of mode velocity power in the ℓ-ν plane for the 1987 uncorrected data. The numbers demarcating the ridge positions are the actual mode velocity power measurements. The lack of contours below the f-mode ridge is

a result of the failure of the algorithm that generates the inter-ridge velocity powers. (b) Same as (a) except for the seeing-corrected data. See the text for more details on the generation of these contour plots.

Figure 4.14: (a) A contour plot of mode velocity power in the ℓ-ν plane for the 1988 uncorrected data. The numbers demarcating the ridge positions are the actual mode velocity power measurements. The lack of contours below the f-mode ridge is a result of the failure of the algorithm that generates the inter-ridge velocity powers. (b) Same as (a) except for the seeing-corrected data. See the text for more details on the generation of these contour plots.

Figure 4.15: The peak velocity power as a function of ℓ, $P_{v,\mathbf{max}}(\ell)$, for the corrected and uncorrected data sets. The solid curves show the corrected data, and the dashed curves show the uncorrected data. These curves are derived from the contour plots shown in Figs. 4.13 and 4.14. (a) $P_{v,\mathbf{max}}(\ell)$ for the 1987 data set. The rapid increase in the corrected $P_{v,\mathbf{max}}(\ell)$ at high ℓ is due to the breakdown of the seeing correction. (b) $P_{v,\mathbf{max}}(\ell)$ for the 1988 data set. The kink at $\ell \approx 475$ is due to an imperfection in the interpolation algorithm. See the text for more details.

Figure 4.16: The frequency of the peak velocity power as a function of ℓ, $\nu_{\mathbf{max}}(\ell)$ for the seeing-corrected data sets. The thick lines are straight-line fits, and are given in Eqs. (4.13a) and (4.13b). (a) $\nu_{\mathbf{max}}(\ell)$ for the 1987 data set. (b) $\nu_{\mathbf{max}}(\ell)$ for the 1988 data set.

Figure 4.17: The velocity power as a function of ν averaged over different ranges in ℓ. The data were averaged over the following ranges in ℓ: $100 \leq \ell \leq 400$ (□), $400 \leq \ell \leq 700$ (△), and $700 \leq \ell \leq 1000$ (◇). The displacement between the different curves is arbitrary. (a) Results from the 1987 data set. (b) Results from the 1988 data set.

Figure 4.18: The MTF for a best-fit linear subtraction filter, given by Eq. (4.14),

and shown as a function of frequency, k. The filter response is two-dimensional, and was used to correct the low-ℓ velocity power measurements. (a) The diagonal terms of the MTF, given in Eq. (4.15). (b) The first off-diagonal terms of the MTF. The off-diagonal terms are essentially negligible compared to the diagonal terms.

Figure 4.19: The number of ridges in the frequency range $2.0\,\mathrm{mHz} \leq \nu \leq 4.0\,\mathrm{mHz}$. The thin curve is the actual ridge count, based on a table of frequencies in Libbrecht, Woodard, and Kaufman (1990). The thick curve is a 7th-order polynomial fit to the ridge count. This is used in calculating the low-ℓ velocity power measurements.

Figure 4.20: The peak velocity power as a function of ℓ, $P_{v,\mathrm{max}}(\ell)$, for the corrected and uncorrected data sets, based on the high-ℓ ridge-fitting technique and the low-ℓ integration method. The corrected and uncorrected ridge-fitting results are depicted by the solid and dashed lines, respectively. The corrected and uncorrected integration results are depicted by the plus signs and the crosses, respectively. Note that there is very good agreement between the two methods. (a) $P_{v,\mathrm{max}}(\ell)$ for the 1987 data set. (b) $P_{v,\mathrm{max}}(\ell)$ for the 1988 data set. See Figs. 4.15a and b for more details.

Figure 4.21: $P_{v,\mathrm{max}}(\ell)$ for both the 1987 (dotted curve) and 1988 (dashed curve) data sets. The low-ℓ values come from the integration method, and the high-ℓ values come the ridge-fitting technique. The two curves are scaled such that the areas under the curves between $\ell = 40$ and $\ell = 400$ are the same.

Figure 4.22: $P_{v,\mathrm{max}}(\ell)$ averaged over the two data sets. Beyond $\ell = 810$, only the 1988 data were included, as the seeing correction for the 1987 data started to break down at this point. See the text for details on the error band. The dashed curve is $M_v^{-1}(\ell)$ for $\tau_{5000} = 0.05$, where $M_v(\ell)$ is the mode mass. This curve assumes that the oscillations are in energy equipartition with constant energy convective eddies.

Figure 4.23: The peak energy, $E_{\mathrm{max}}(\ell)$, assuming that mode energy is given by

Eq. (4.16). The data have been scaled to full-disk Dopplergram, $\ell = 20$, $\nu = 3.20$ mHz, mode energy measurements in Libbrecht (1988b).

Figure 4.24: The total mode energy in all modes of degree ℓ, E_ℓ, calculated over the frequency range $1.5\,\mathrm{mHz} \leq \nu \leq 5.5\,\mathrm{mHz}$. Note that E_ℓ peaks at $\ell \sim 170$.

Figure 4.25: The cumulative total energy, $E_{\mathrm{cum}}(\ell)$, calculated from E_ℓ. From this we conclude that the total energy in all modes, E_{tot}, is $E_{\mathrm{tot}} \gtrsim 6 \times 10^{33}$ ergs, or about the same as the amount of energy radiated by the Sun in 1.5 seconds.

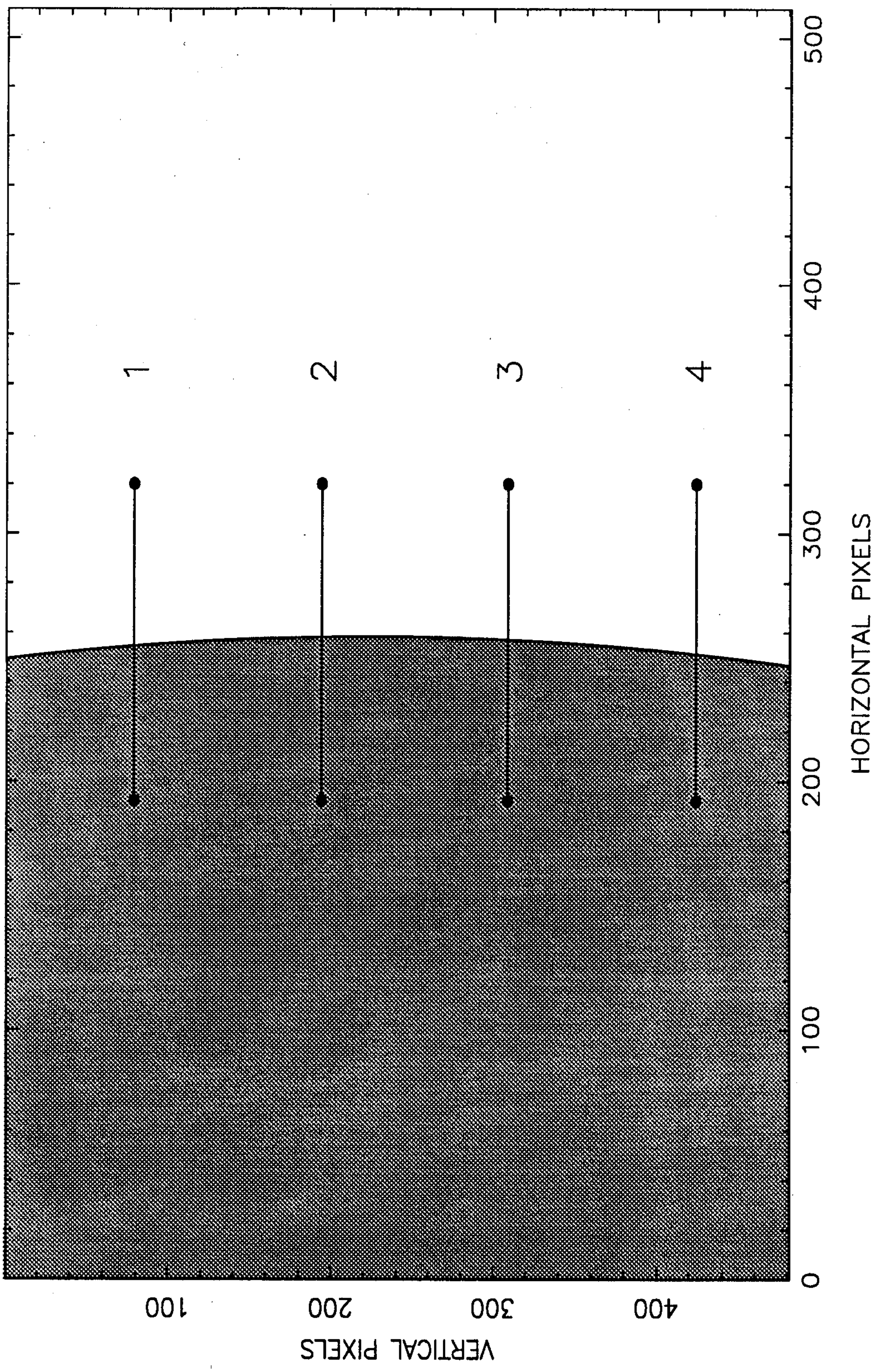
1
2
3
4
HORIZONTAL PIXELS
0
100
200
300
400
500
VERTICAL PIXELS
100
200
300
400

Fig. 4.1

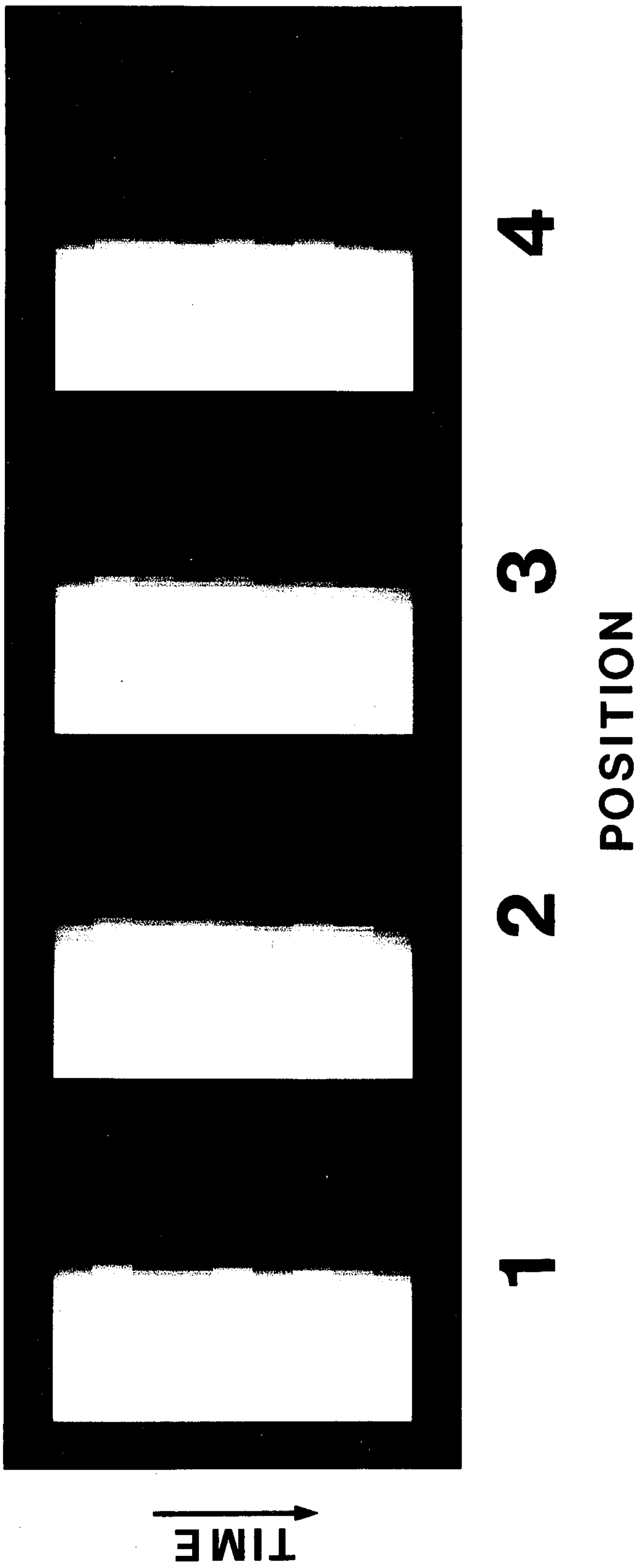

Fig. 4.2

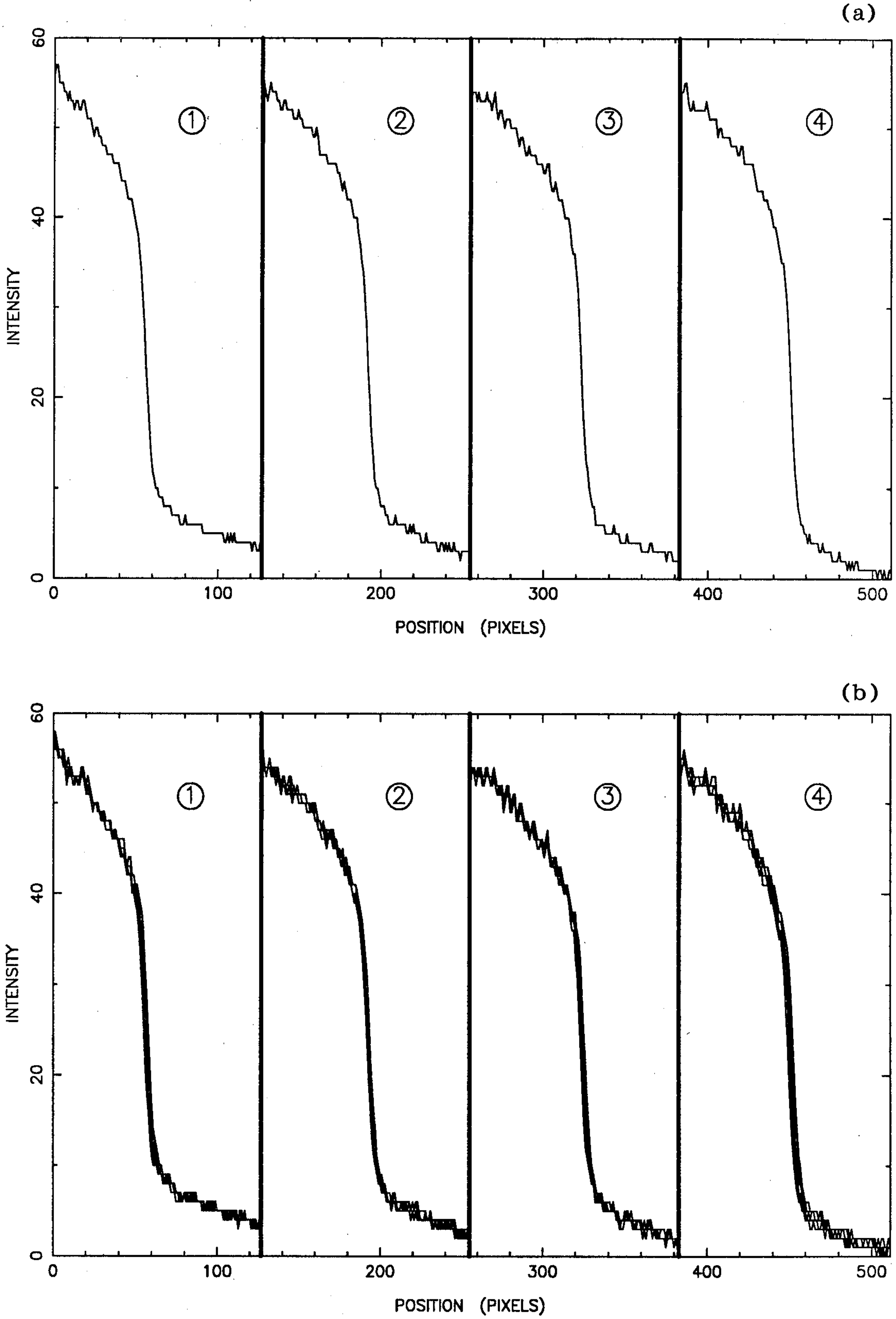
(a)
INTENSITY
0
20
40
60
①
②
③
④
POSITION (PIXELS)
0
100
200
300
400
500
(b)
INTENSITY
0
20
40
60
①
②
③
④
POSITION (PIXELS)
0
100
200
300
400
500

Fig. 4.3

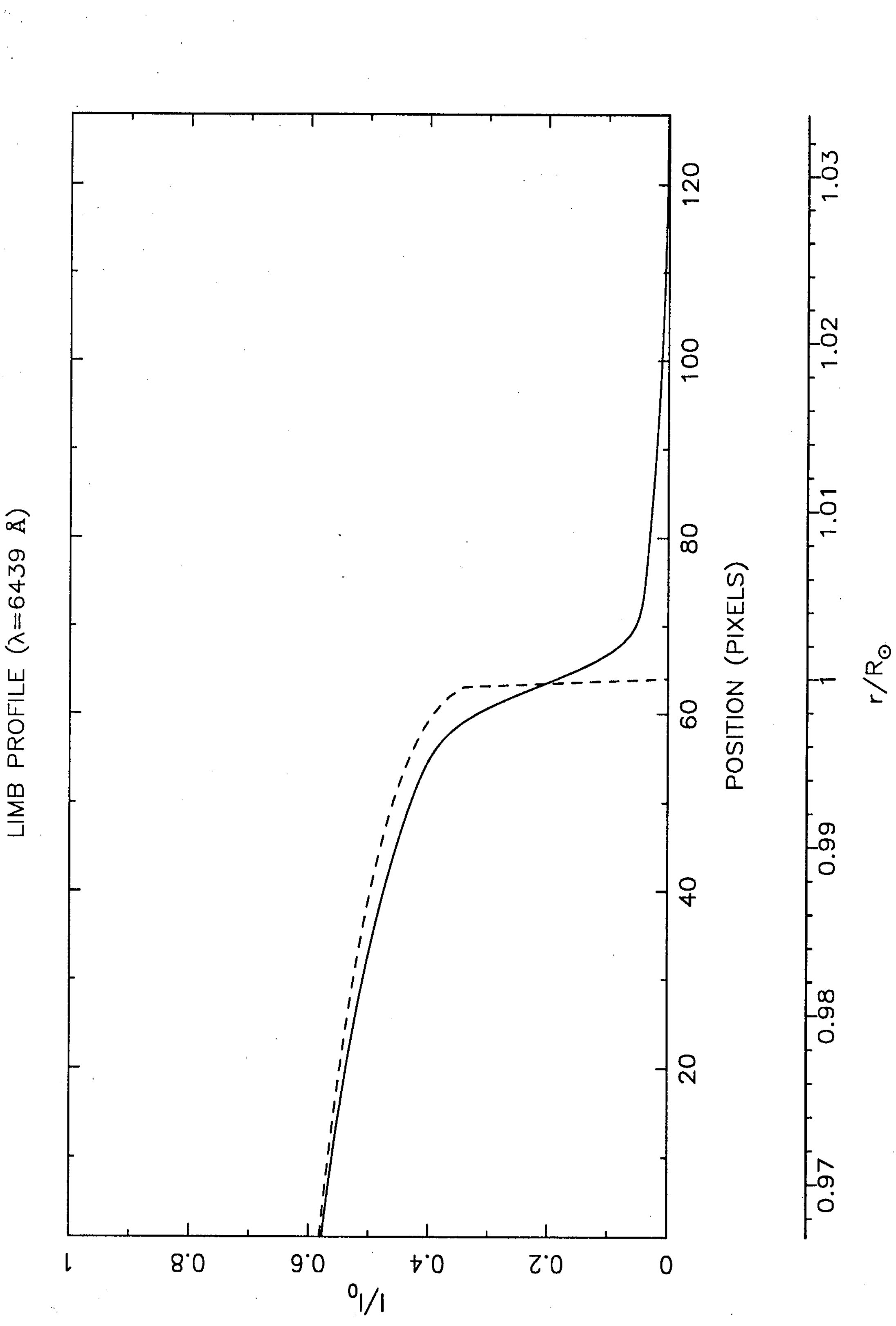
LIMB PROFILE (λ=6439 Å)
POSITION (PIXELS)
20
40
60
80
100
120
I/I0
0
0.2
0.4
0.6
0.8
1
r/R⊙
0.97
0.98
0.99
1
1.01
1.02
1.03

Fig. 4.4

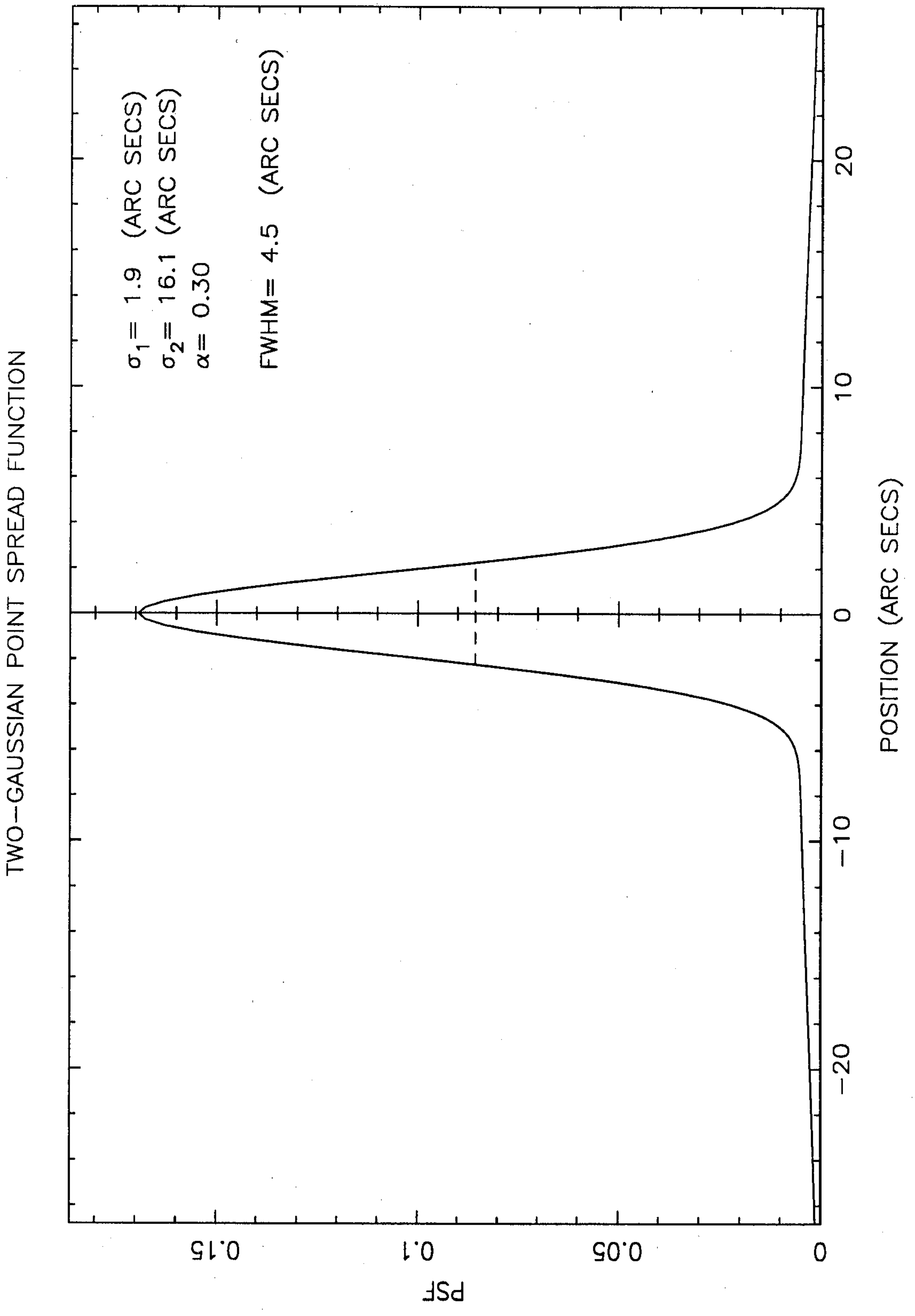
TWO-GAUSSIAN POINT SPREAD FUNCTION
σ_1= 1.9 (ARC SECS)
σ_2= 16.1 (ARC SECS)
α= 0.30
FWHM= 4.5 (ARC SECS)
POSITION (ARC SECS)
PSF
0
0.05
0.1
0.15
−20
−10
0
10
20

Fig. 4.5

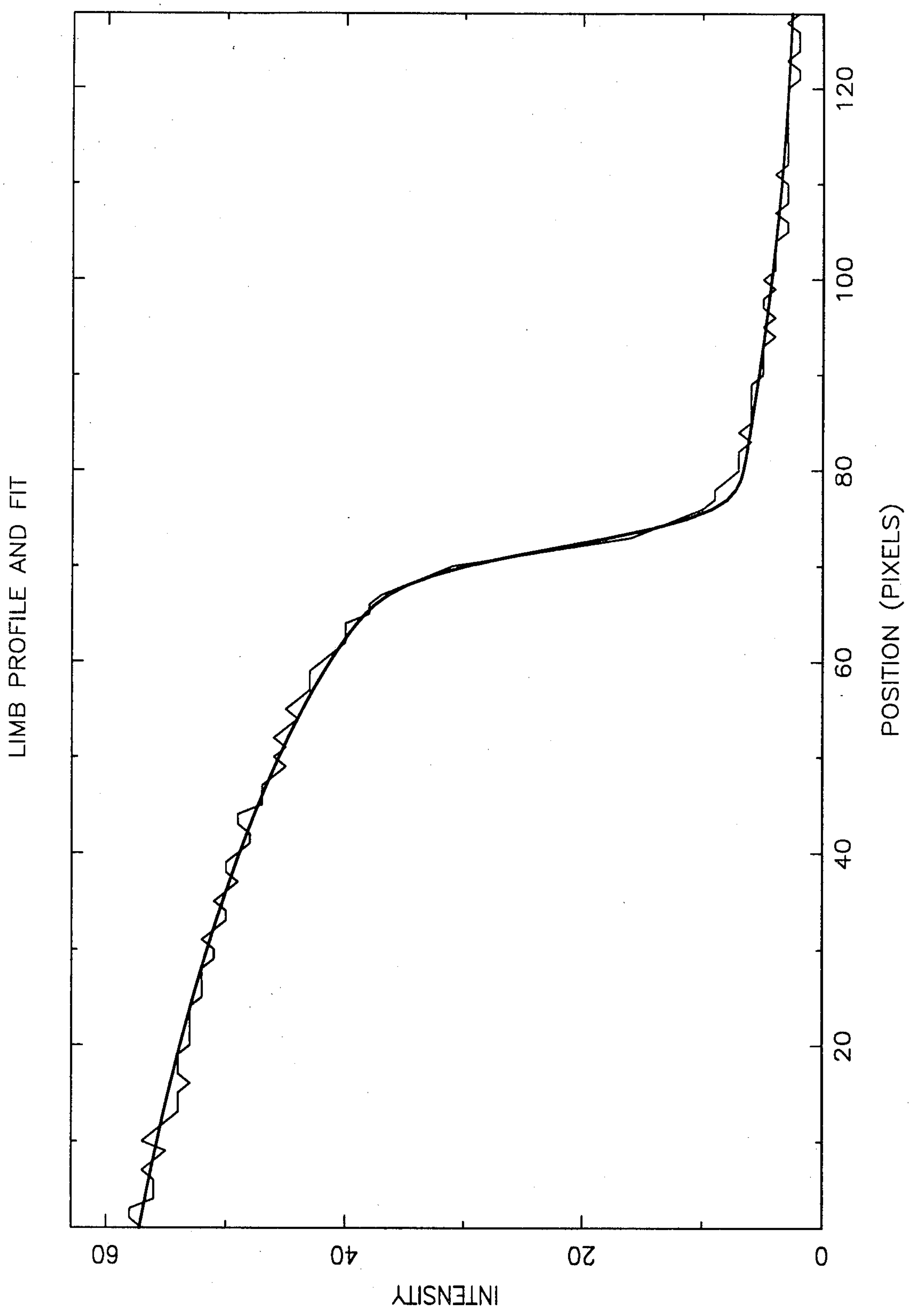
LIMB PROFILE AND FIT
POSITION (PIXELS)
INTENSITY
0
20
40
60
80
100
120
0
20
40
60

Fig. 4.6

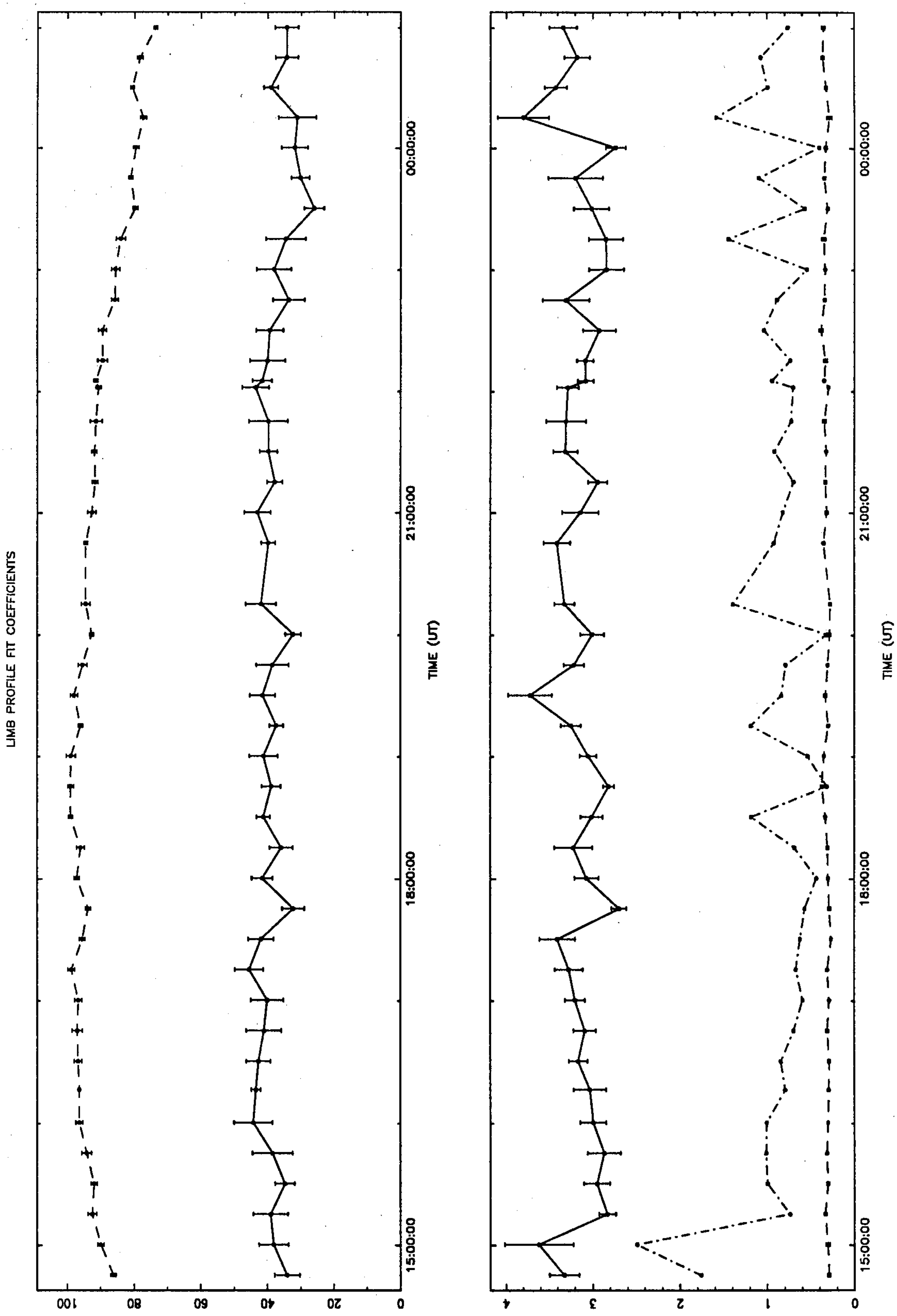
LIMB PROFILE FIT COEFFICIENTS
PIXELS
100
80
60
40
20
0
TIME (UT)
15:00:00
18:00:00
21:00:00
00:00:00
PIXELS
4
3
2
1
0
TIME (UT)
15:00:00
18:00:00
21:00:00
00:00:00

Fig. 4.7

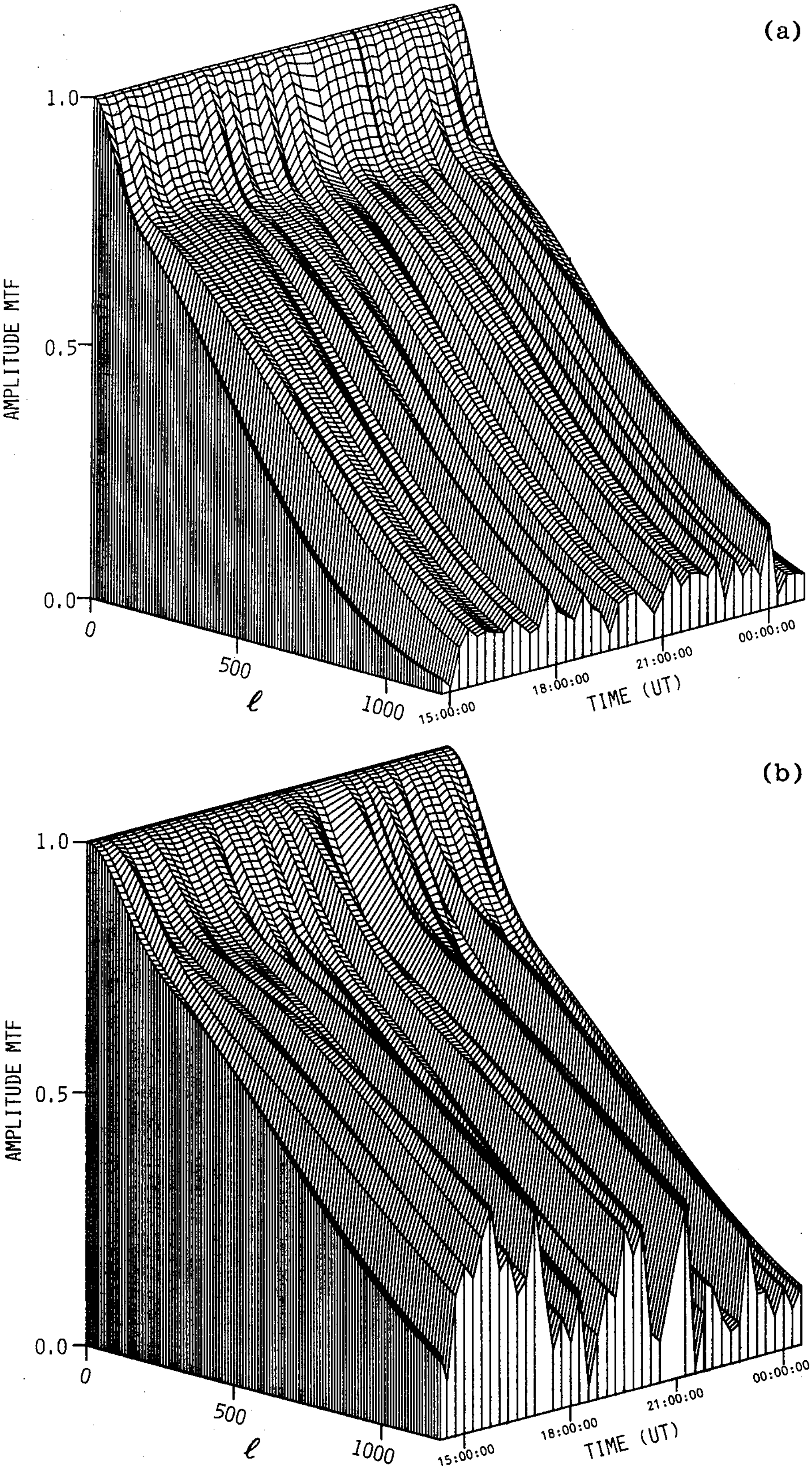
(a)
1.0
0.5
0.0
AMPLITUDE MTF
0
500
ℓ
1000
15:00:00
18:00:00
21:00:00
00:00:00
TIME (UT)
(b)
1.0
0.5
0.0
AMPLITUDE MTF
0
500
ℓ
1000
15:00:00
18:00:00
21:00:00
00:00:00
TIME (UT)

Fig. 4.8

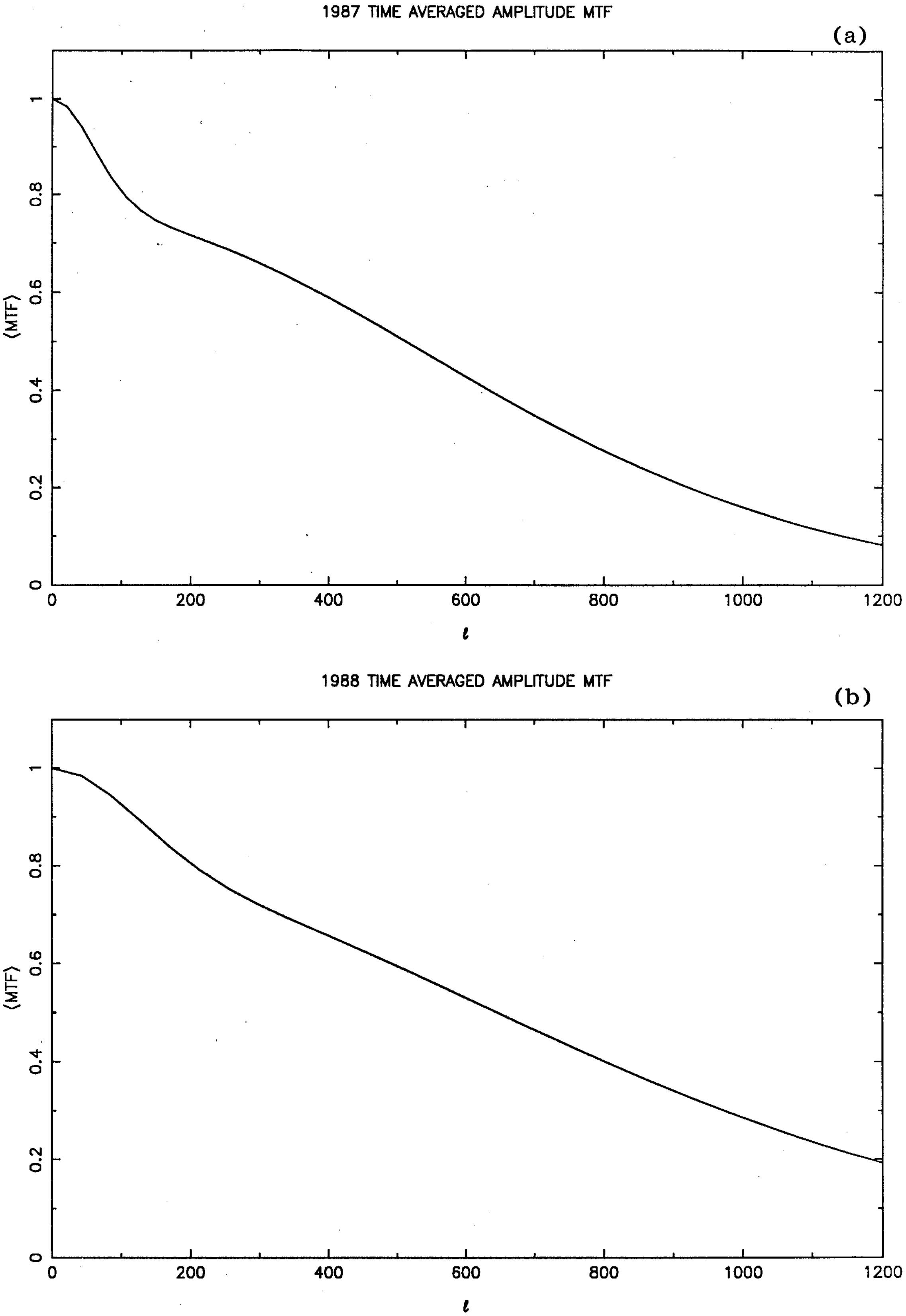
1987 TIME AVERAGED AMPLITUDE MTF
(a)
⟨MTF⟩
0
0.2
0.4
0.6
0.8
1
0
200
400
600
800
1000
1200
ℓ
1988 TIME AVERAGED AMPLITUDE MTF
(b)
⟨MTF⟩
0
0.2
0.4
0.6
0.8
1
0
200
400
600
800
1000
1200
ℓ

Fig. 4.9

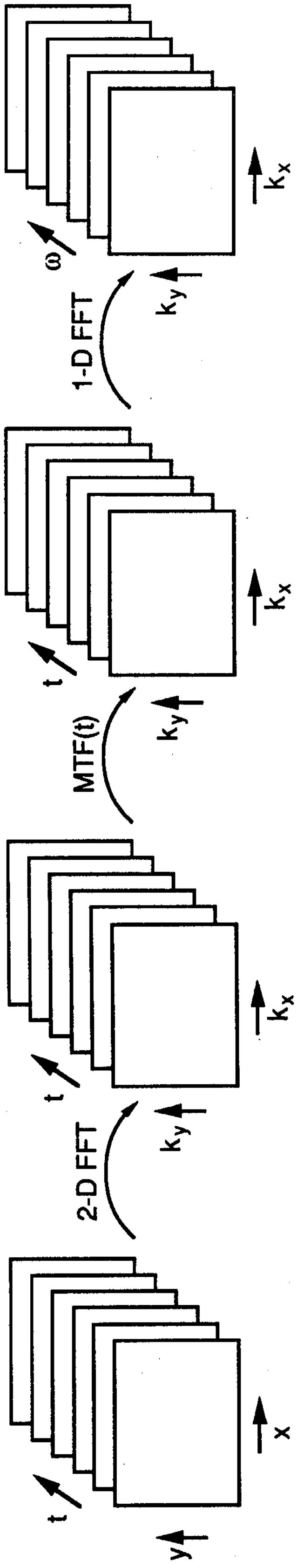

Fig. 4.10

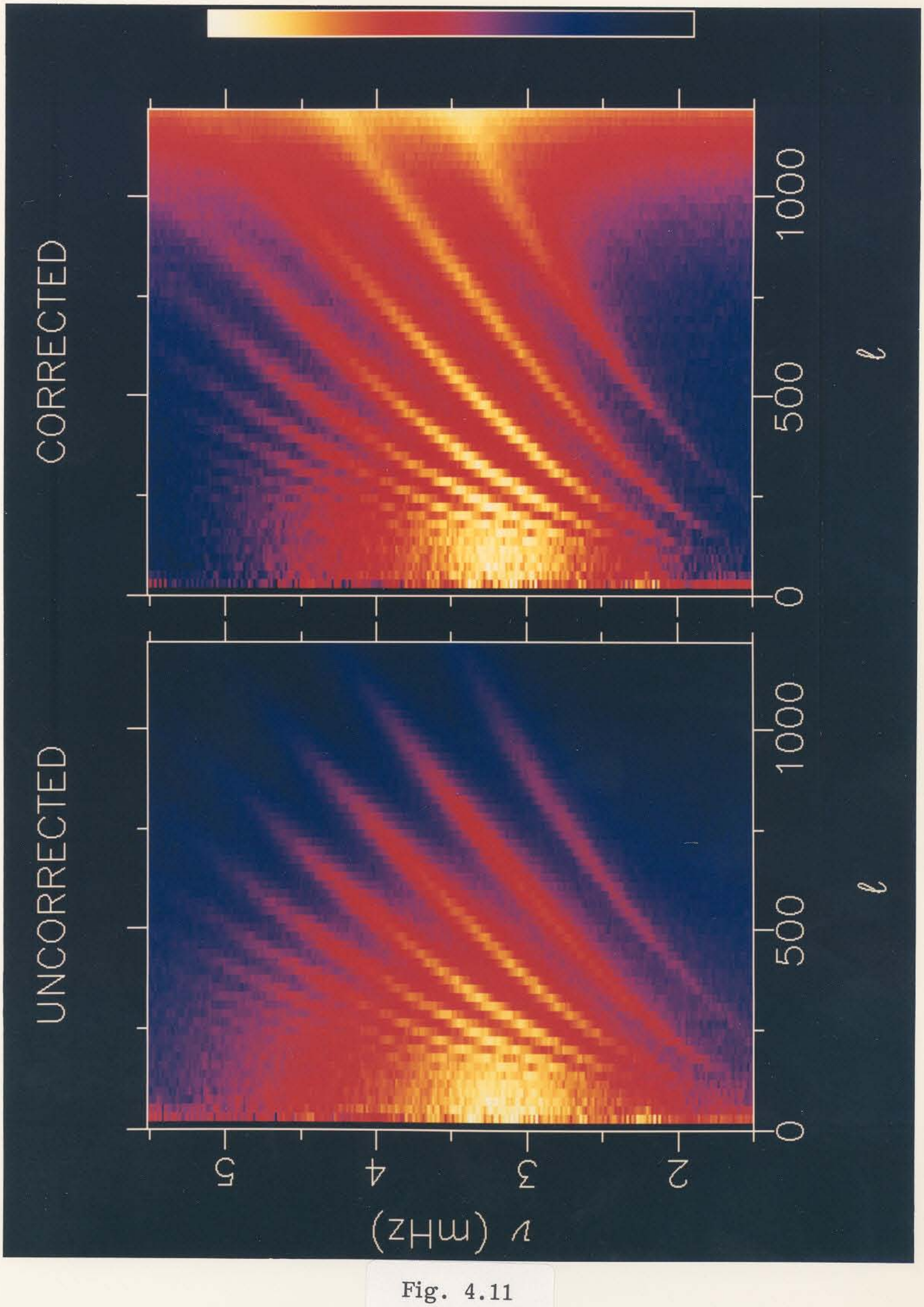
CORRECTED
UNCORRECTED
0
500
1000
ℓ
0
500
1000
ℓ
2
3
4
5
ν (mHz)

Fig. 4.11

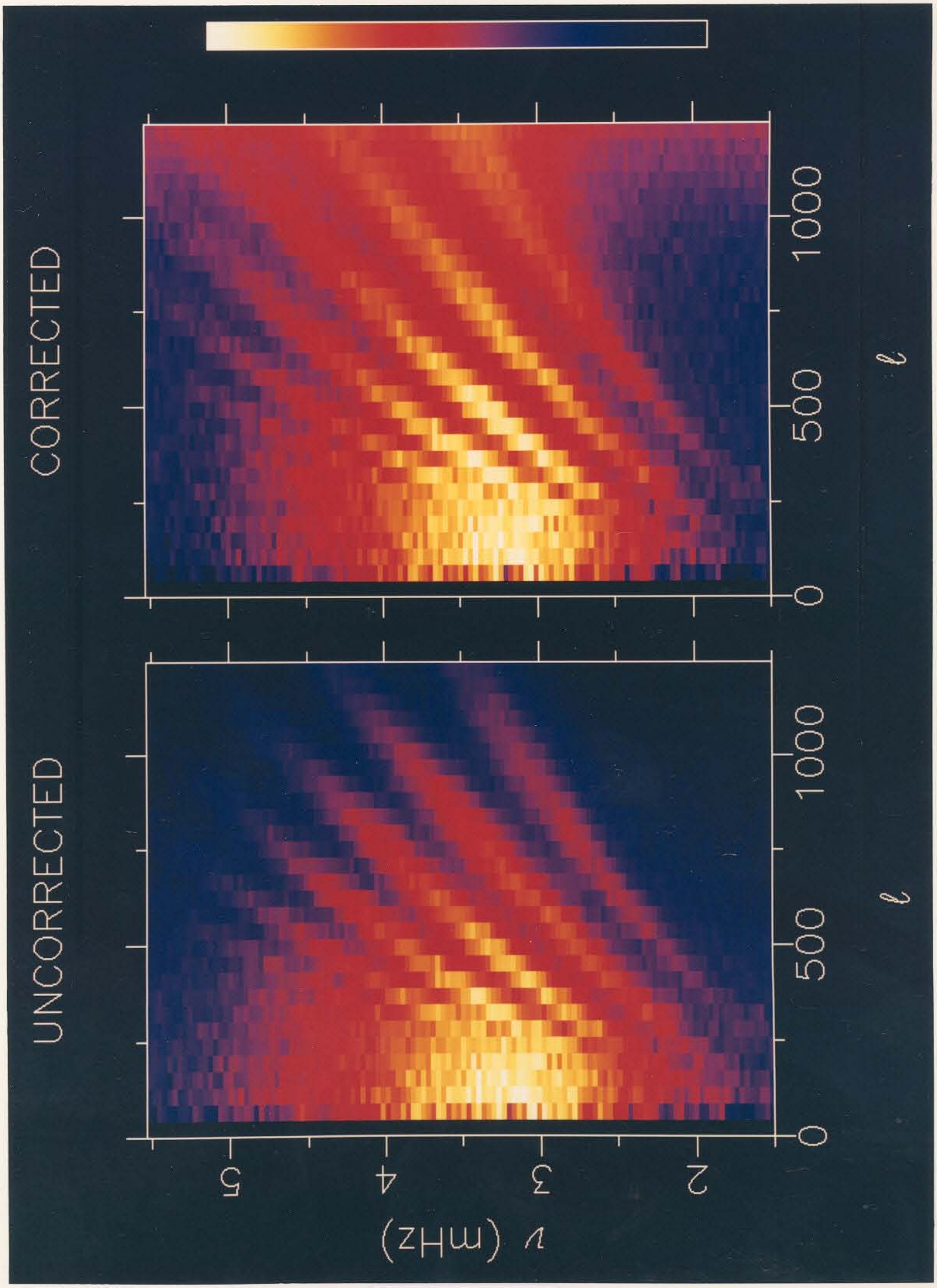

Fig. 4.12

1987 UNCORRECTED

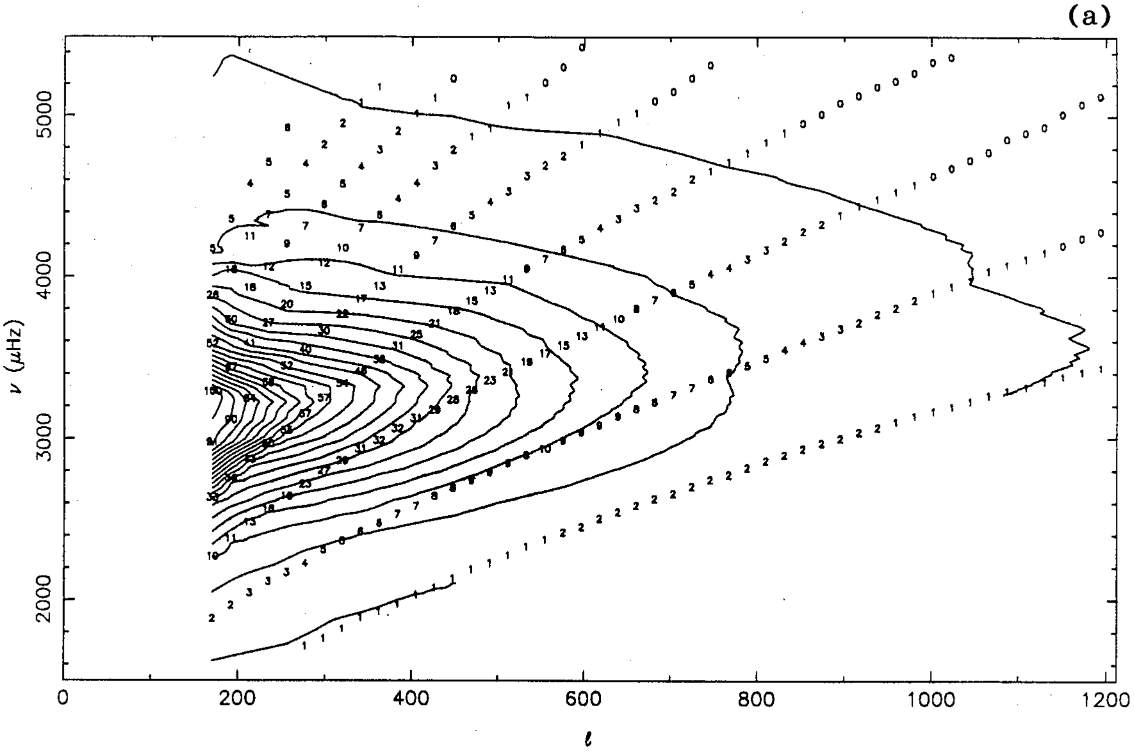

1987 CORRECTED

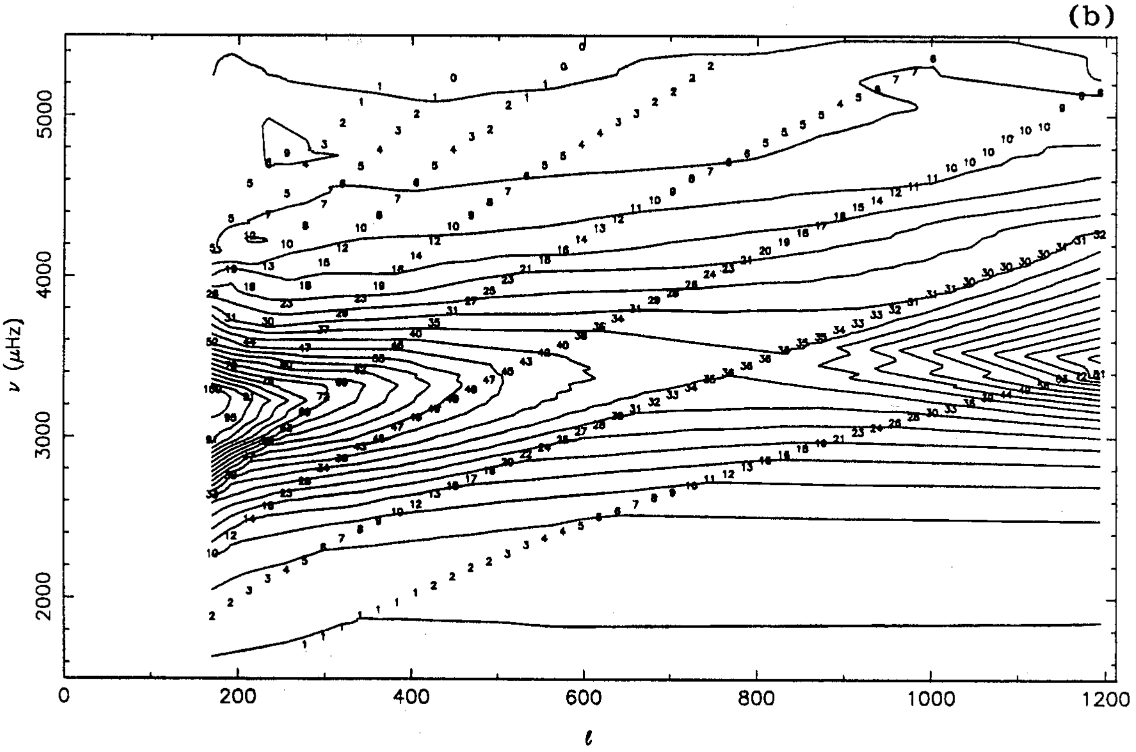

Fig. 4.13

1988 UNCORRECTED

(a)

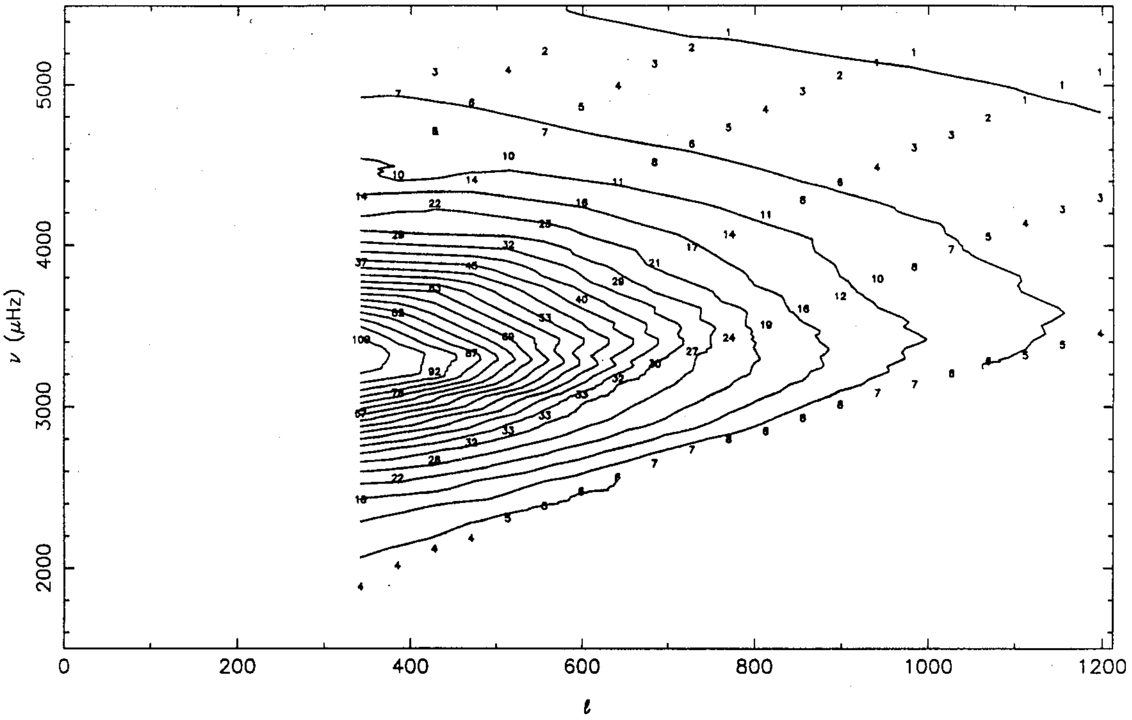

1988 CORRECTED

(b)

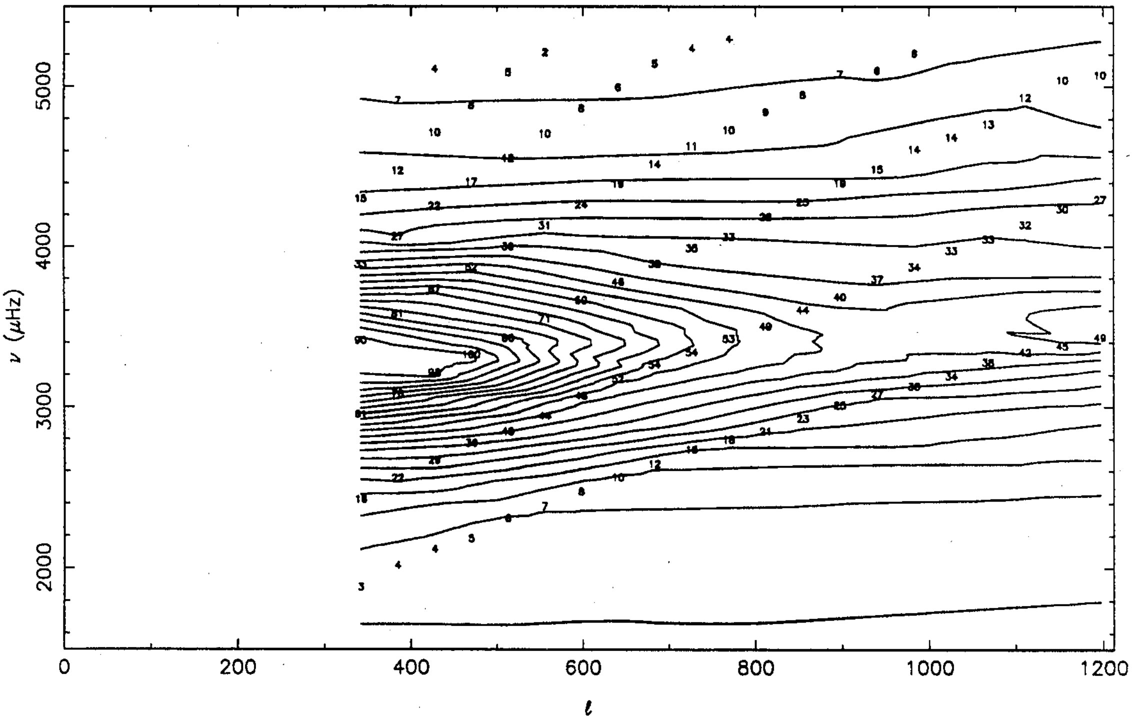

Fig. 4.14

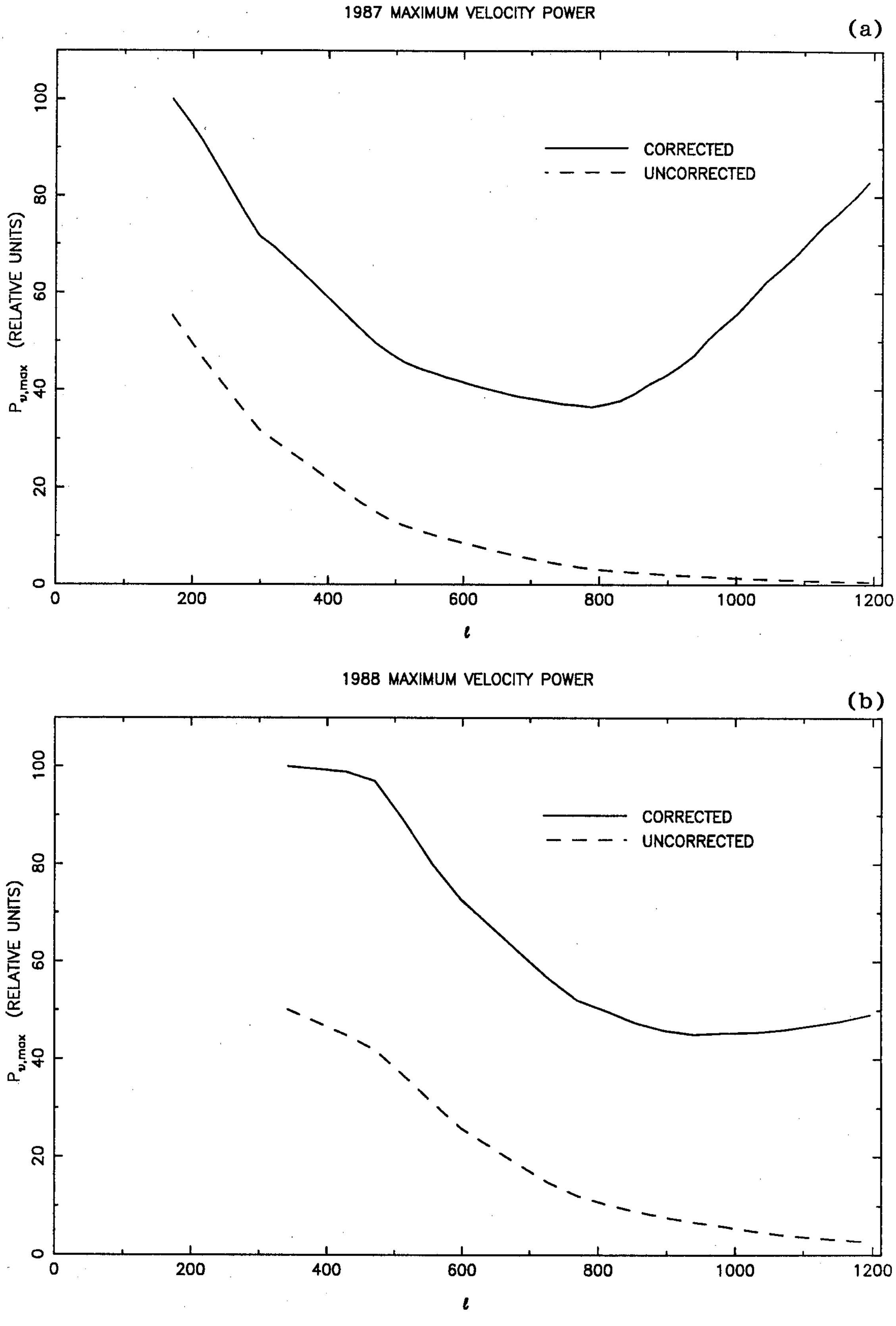
1987 MAXIMUM VELOCITY POWER
(a)
CORRECTED
UNCORRECTED
$P_{v,max}$ (RELATIVE UNITS)
0
20
40
60
80
100
0
200
400
600
800
1000
1200
ℓ
1988 MAXIMUM VELOCITY POWER
(b)
CORRECTED
UNCORRECTED
$P_{v,max}$ (RELATIVE UNITS)
0
20
40
60
80
100
0
200
400
600
800
1000
1200
ℓ

Fig. 4.15

1987 FREQUENCY OF MAXIMUM VELOCITY POWER

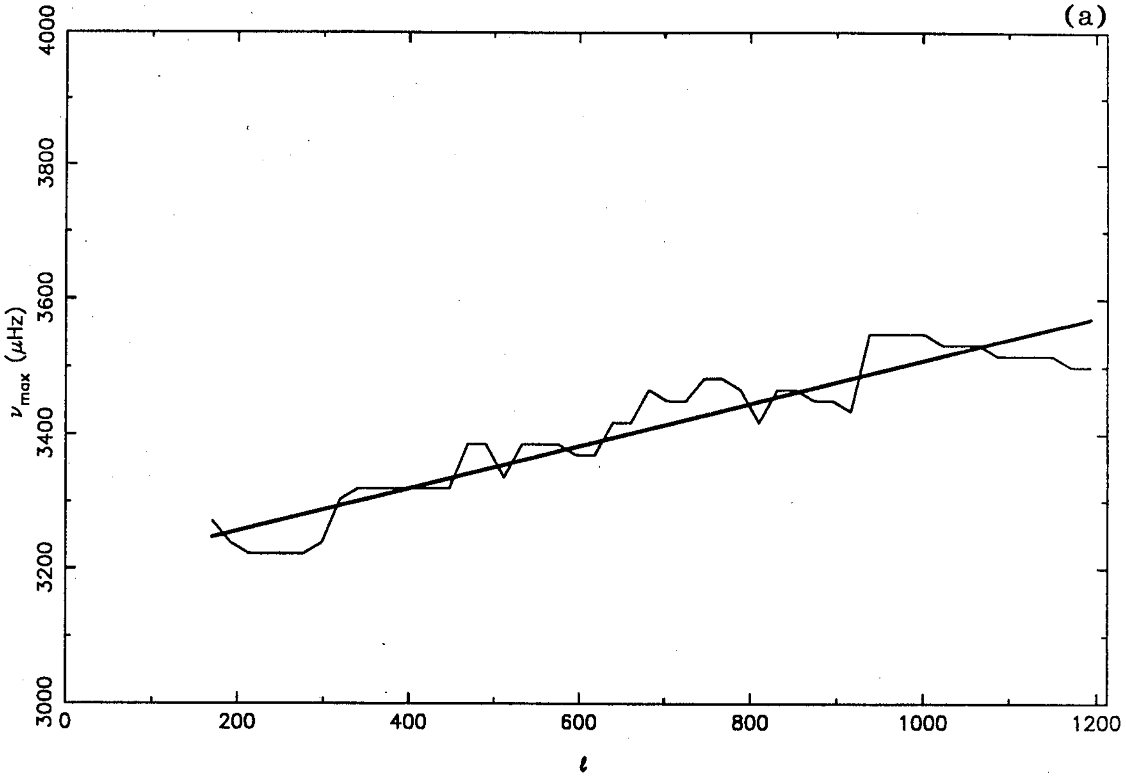

1988 FREQUENCY OF MAXIMUM VELOCITY POWER

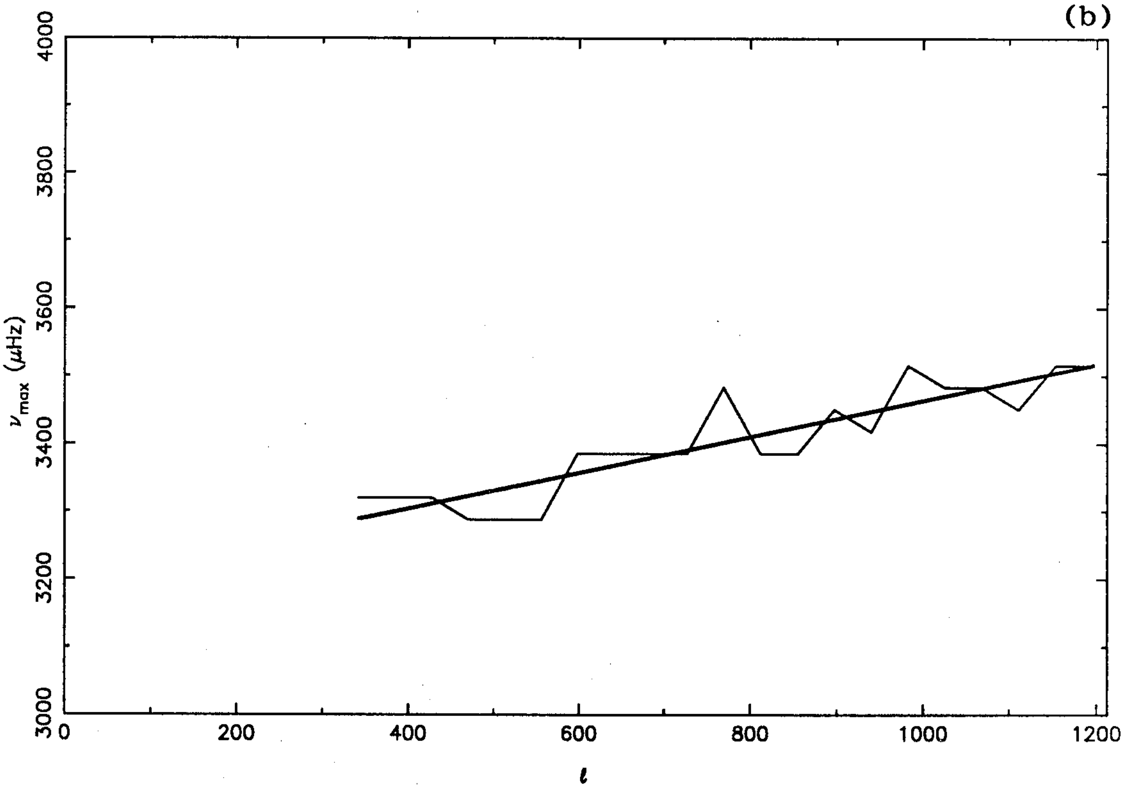

Fig. 4.16

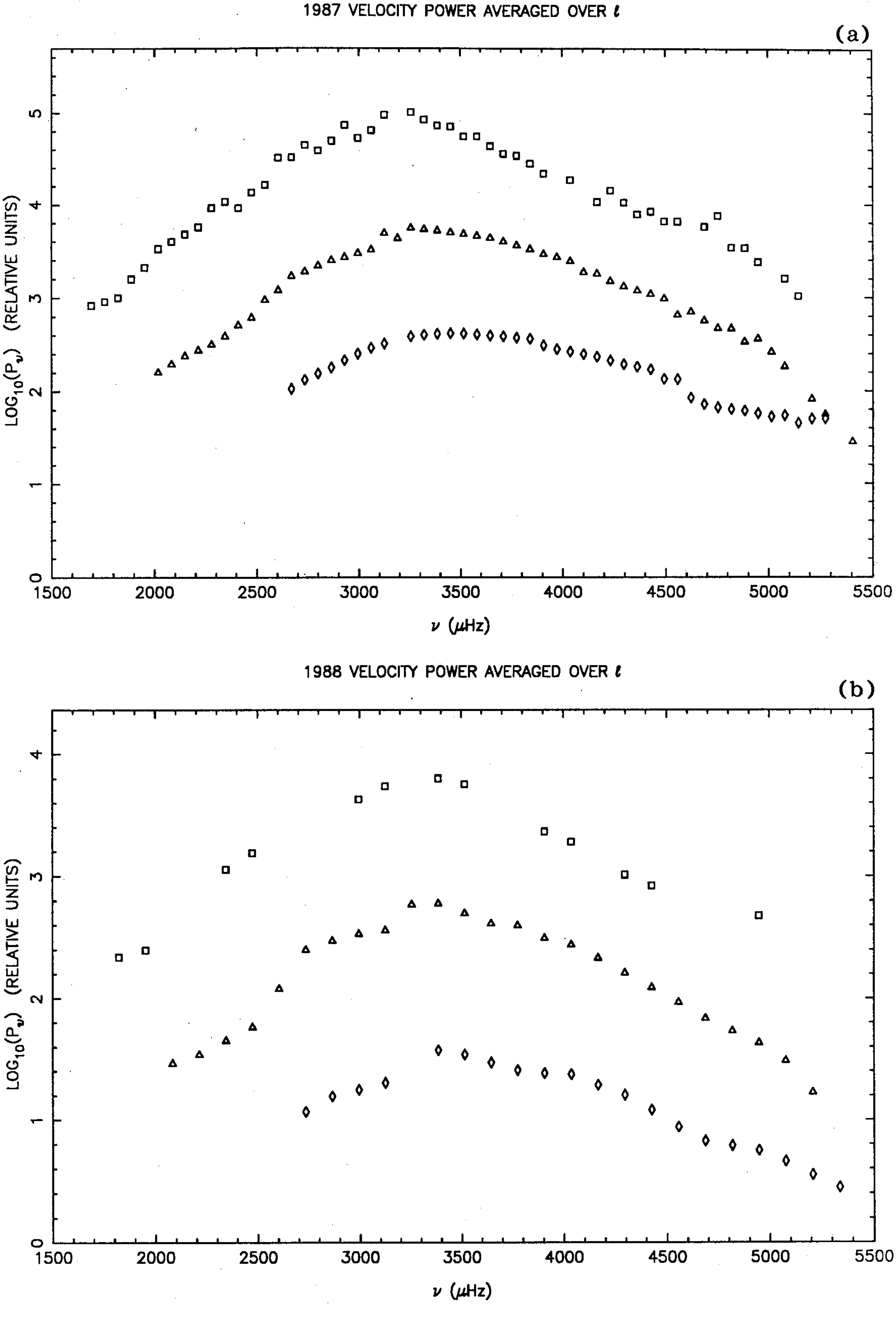
1987 VELOCITY POWER AVERAGED OVER ℓ
(a)
LOG$_{10}$(P$_\nu$) (RELATIVE UNITS)
0
1
2
3
4
5
1500
2000
2500
3000
3500
4000
4500
5000
5500
ν (μHz)
1988 VELOCITY POWER AVERAGED OVER ℓ
(b)
LOG$_{10}$(P$_\nu$) (RELATIVE UNITS)
0
1
2
3
4
1500
2000
2500
3000
3500
4000
4500
5000
5500
ν (μHz)

Fig. 4.17

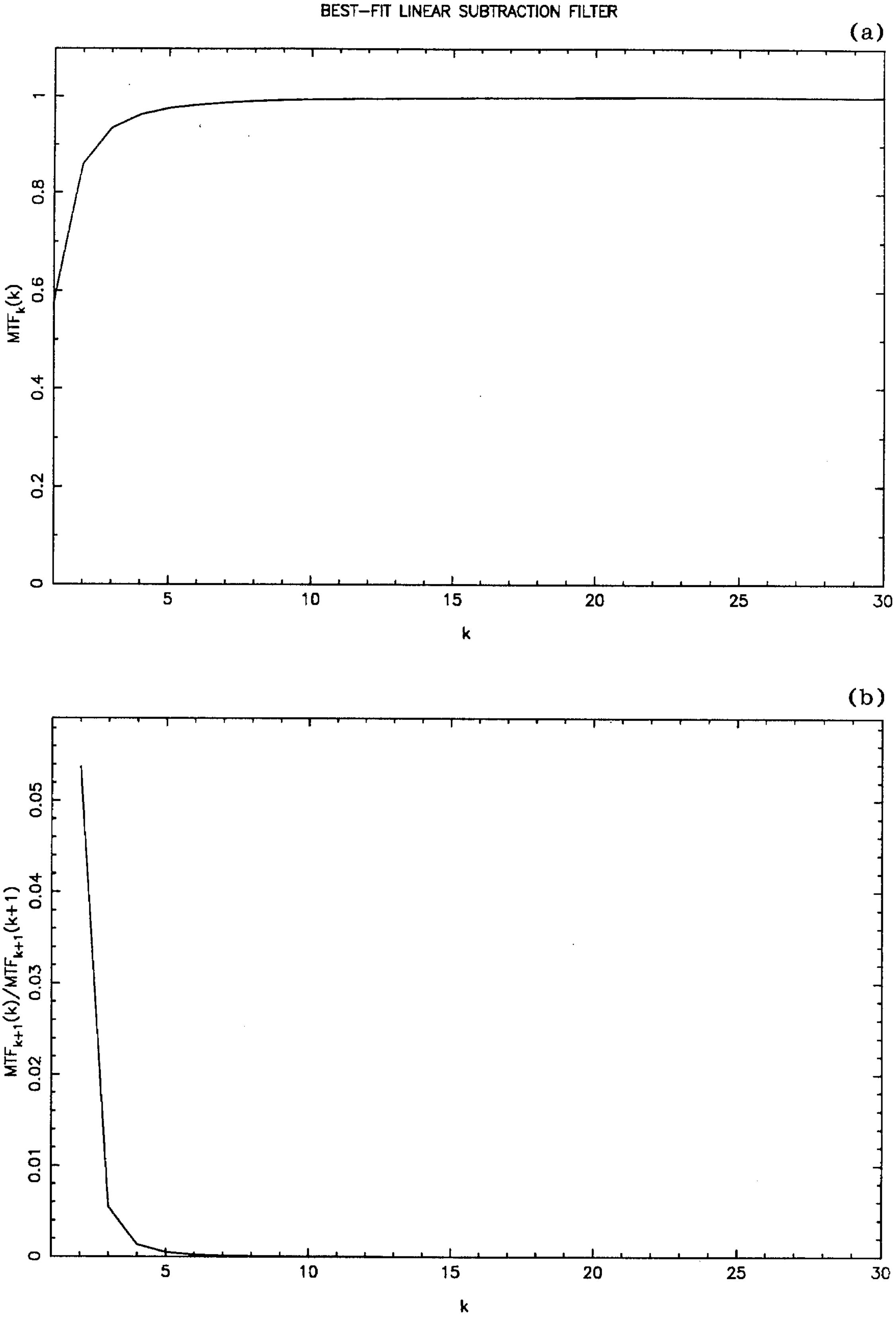
BEST-FIT LINEAR SUBTRACTION FILTER
(a)
$MTF_k(k)$
0
0.2
0.4
0.6
0.8
1
5
10
15
20
25
30
k
(b)
$MTF_{k+1}(k)/MTF_{k+1}(k+1)$
0
0.01
0.02
0.03
0.04
0.05
5
10
15
20
25
30
k

Fig. 4.18

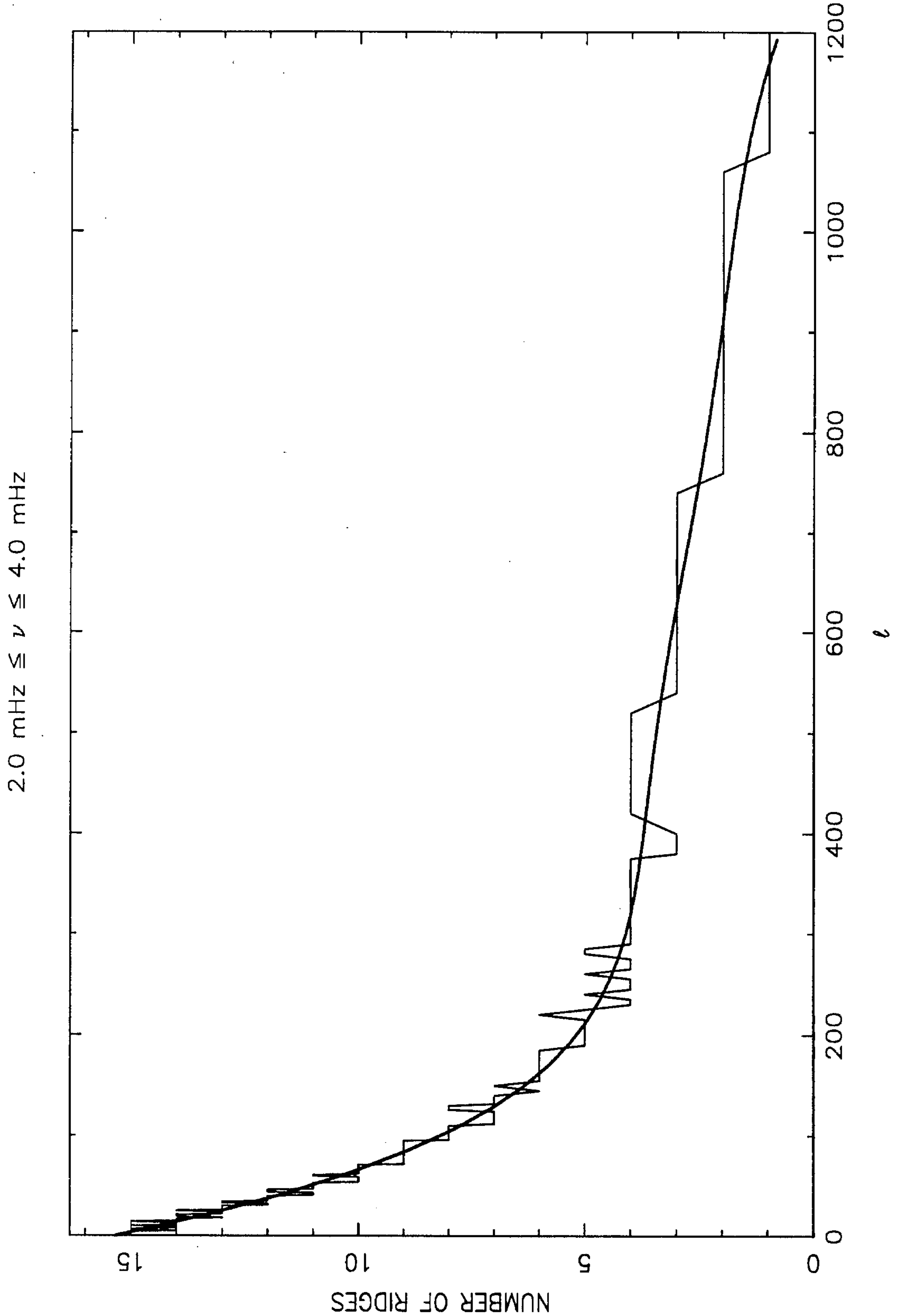
2.0 mHz ≤ ν ≤ 4.0 mHz
NUMBER OF RIDGES
0
5
10
15
ℓ
0
200
400
600
800
1000
1200

Fig. 4.19

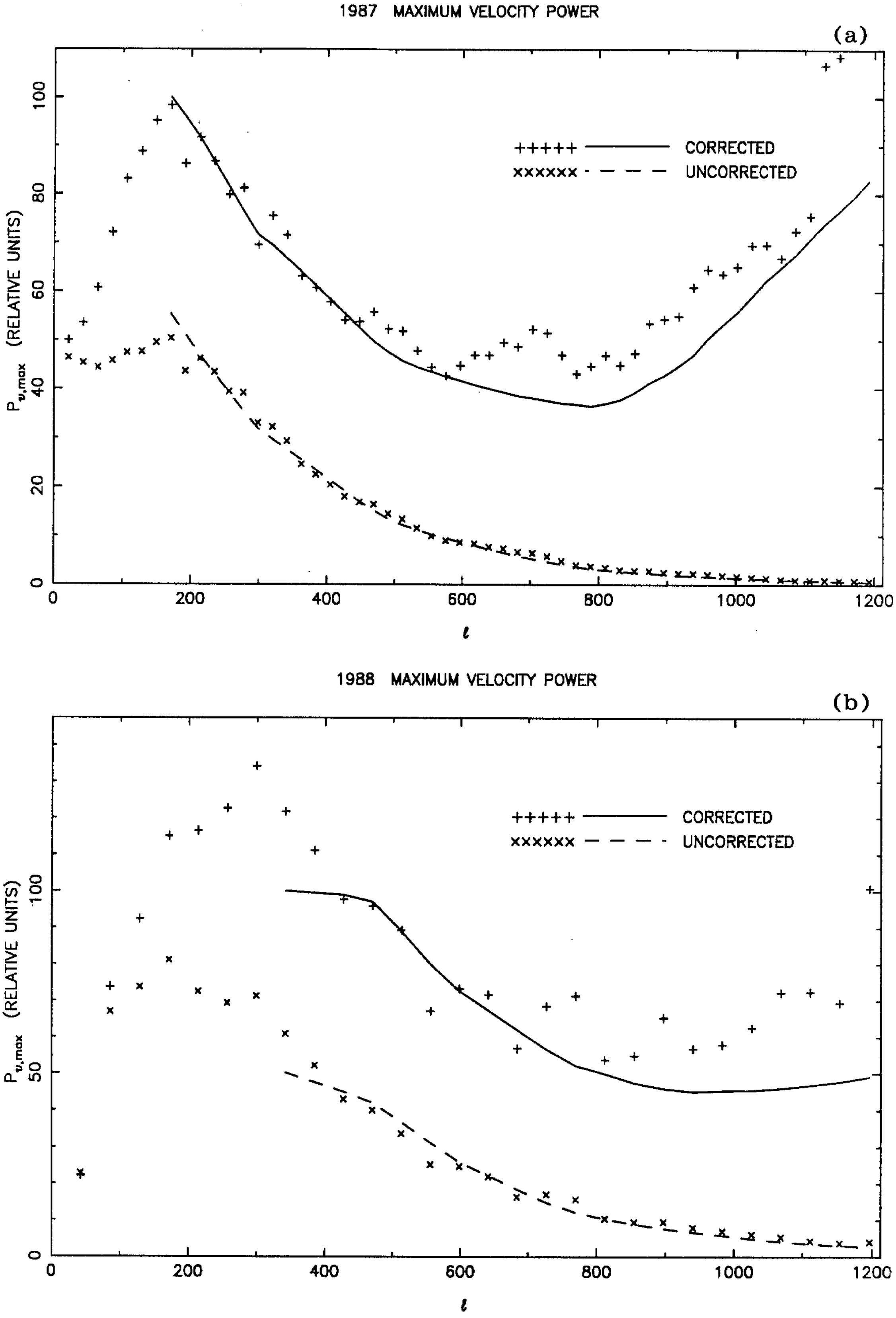
1987 MAXIMUM VELOCITY POWER
(a)
+++++ CORRECTED
xxxxxx UNCORRECTED
$P_{v,max}$ (RELATIVE UNITS)
0
20
40
60
80
100
0
200
400
600
800
1000
1200
ℓ
1988 MAXIMUM VELOCITY POWER
(b)
+++++ CORRECTED
xxxxxx UNCORRECTED
$P_{v,max}$ (RELATIVE UNITS)
0
50
100
0
200
400
600
800
1000
1200
ℓ

Fig. 4.20

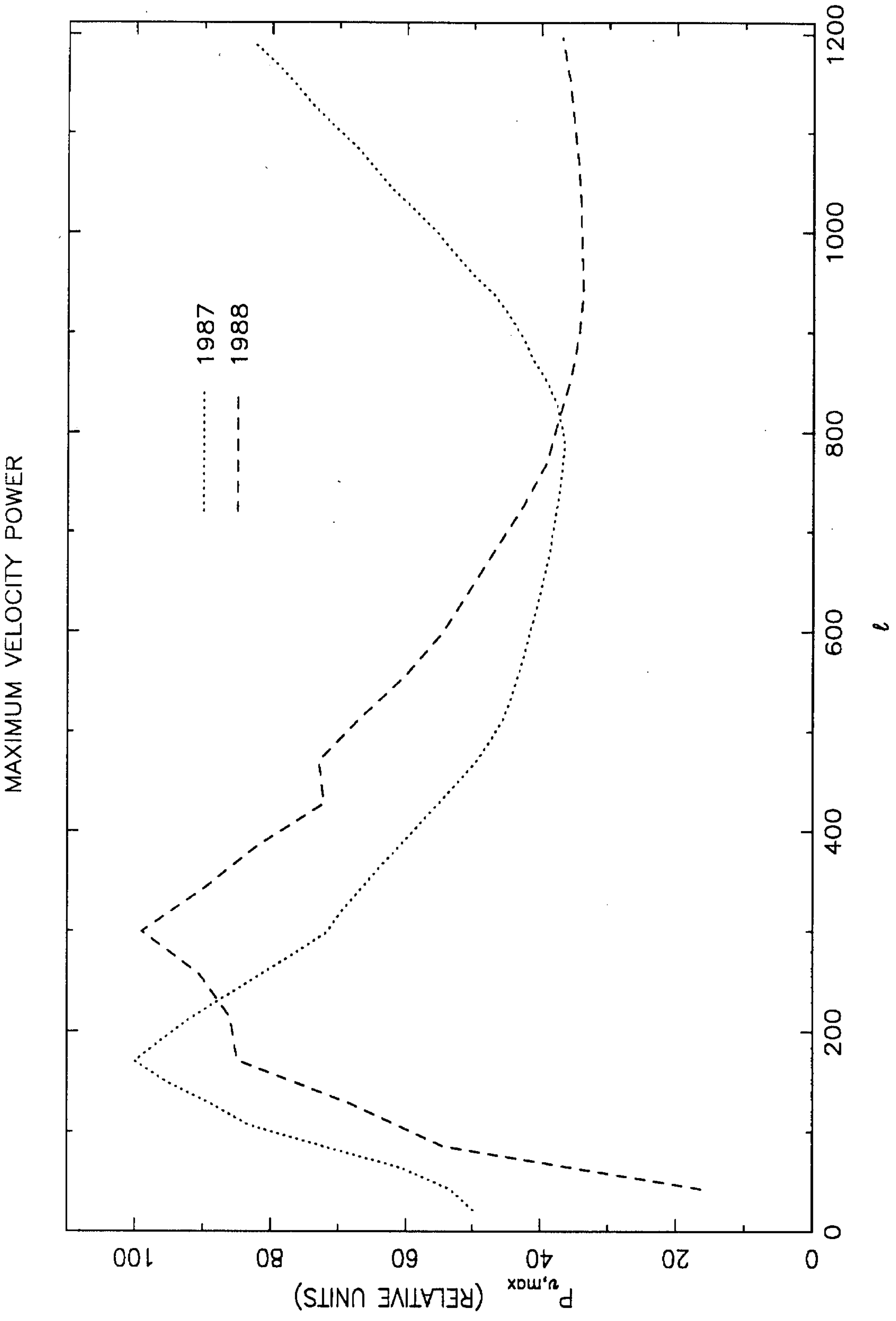
MAXIMUM VELOCITY POWER
1987
1988
$P_{v,max}$ (RELATIVE UNITS)
0
20
40
60
80
100
ℓ
0
200
400
600
800
1000
1200

Fig. 4.21

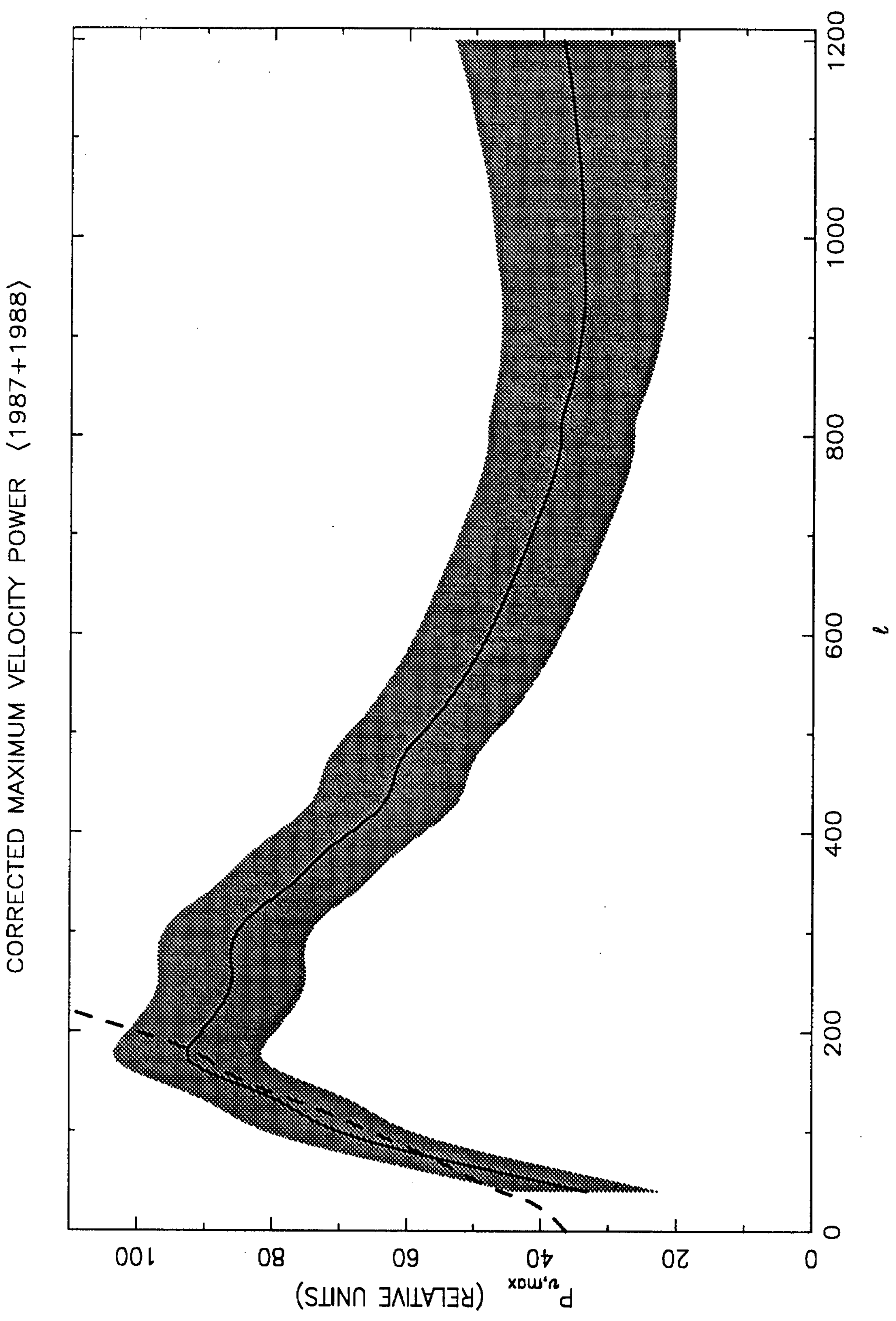
CORRECTED MAXIMUM VELOCITY POWER (1987+1988)
$P_{v,max}$ (RELATIVE UNITS)
0
20
40
60
80
100
l
0
200
400
600
800
1000
1200

Fig. 4.22

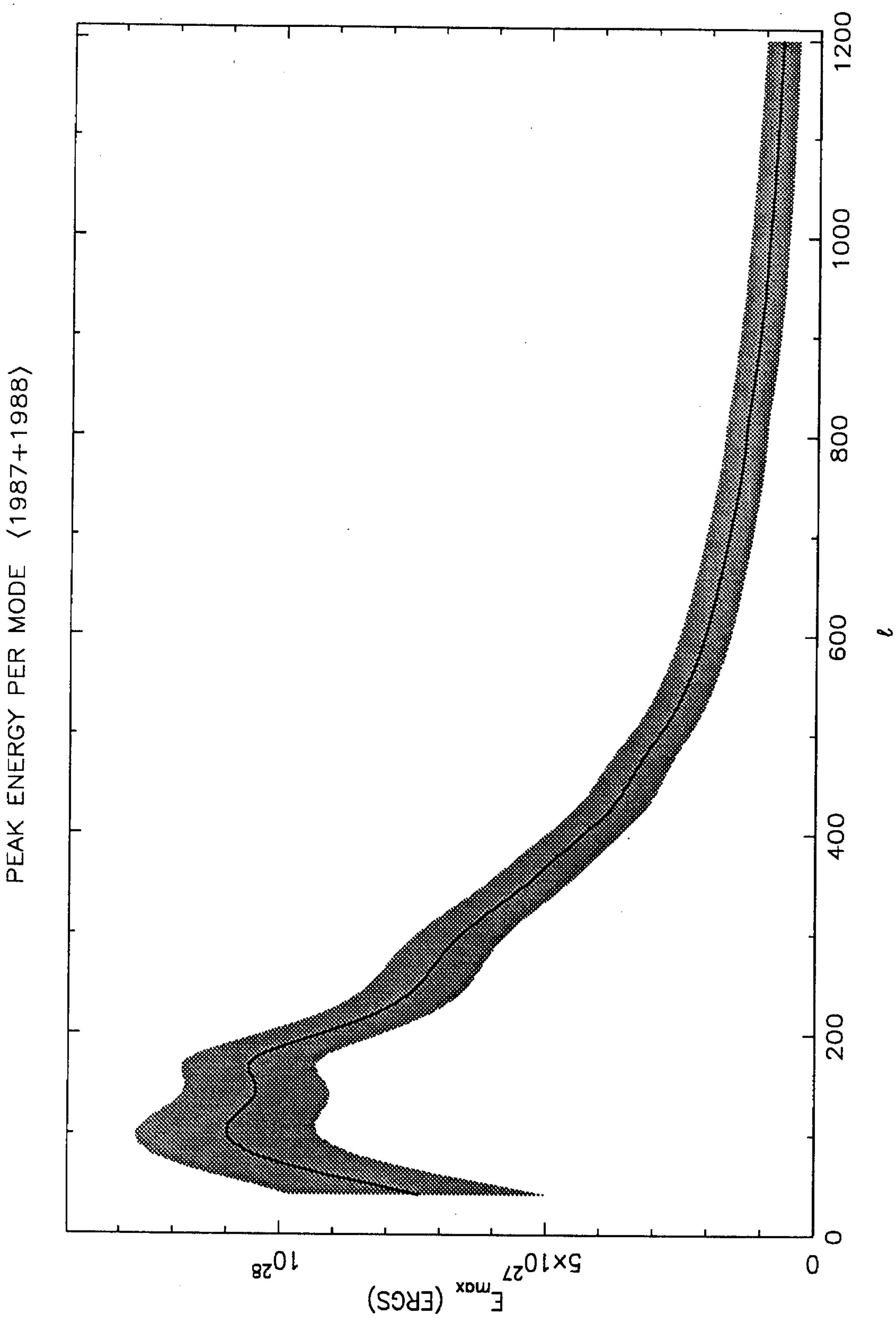
PEAK ENERGY PER MODE ⟨1987+1988⟩
E_{max} (ERGS)
0
5×10^{27}
10^{28}
0
200
400
600
800
1000
1200
ℓ

Fig. 4.23

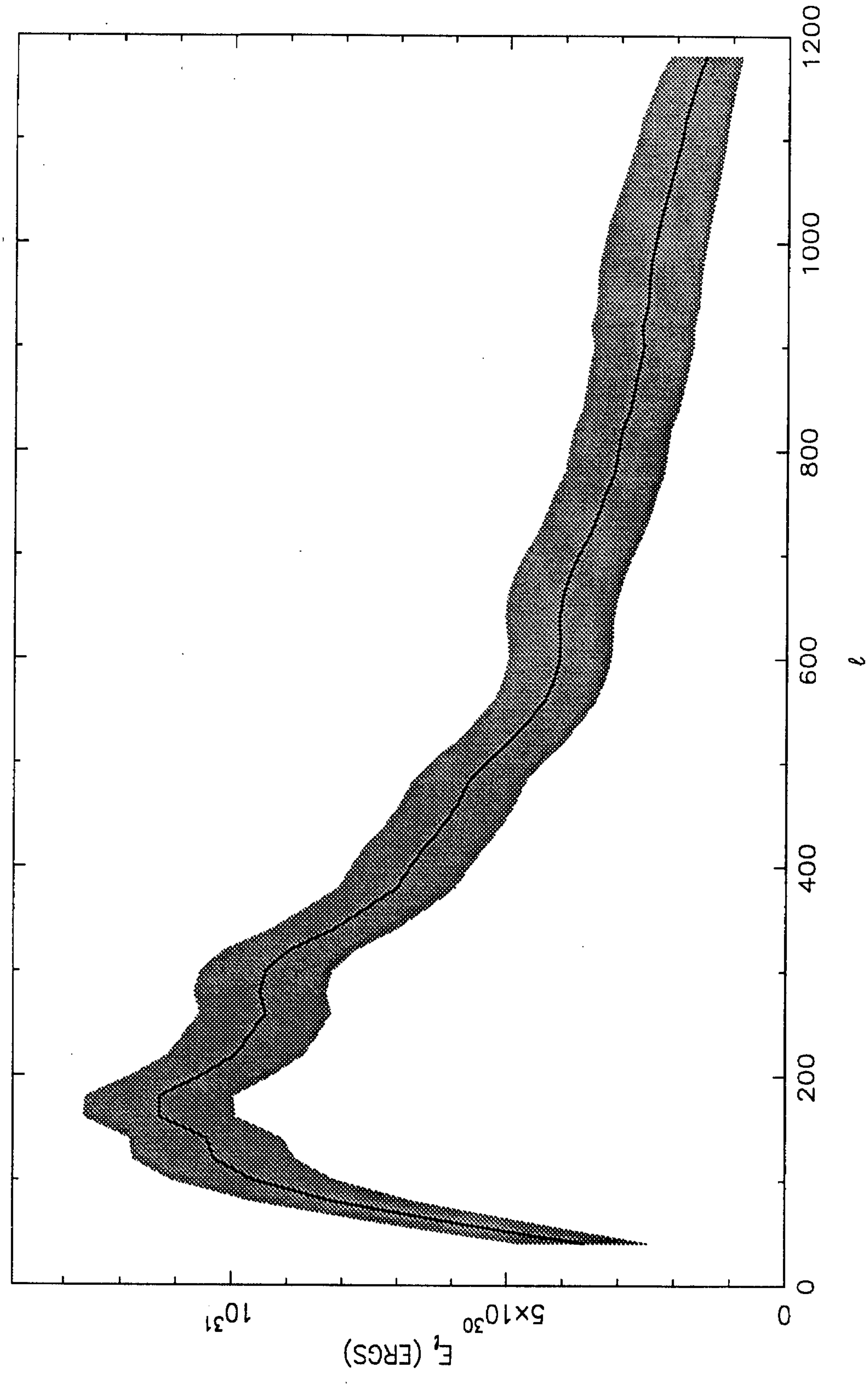

Fig. 4.24

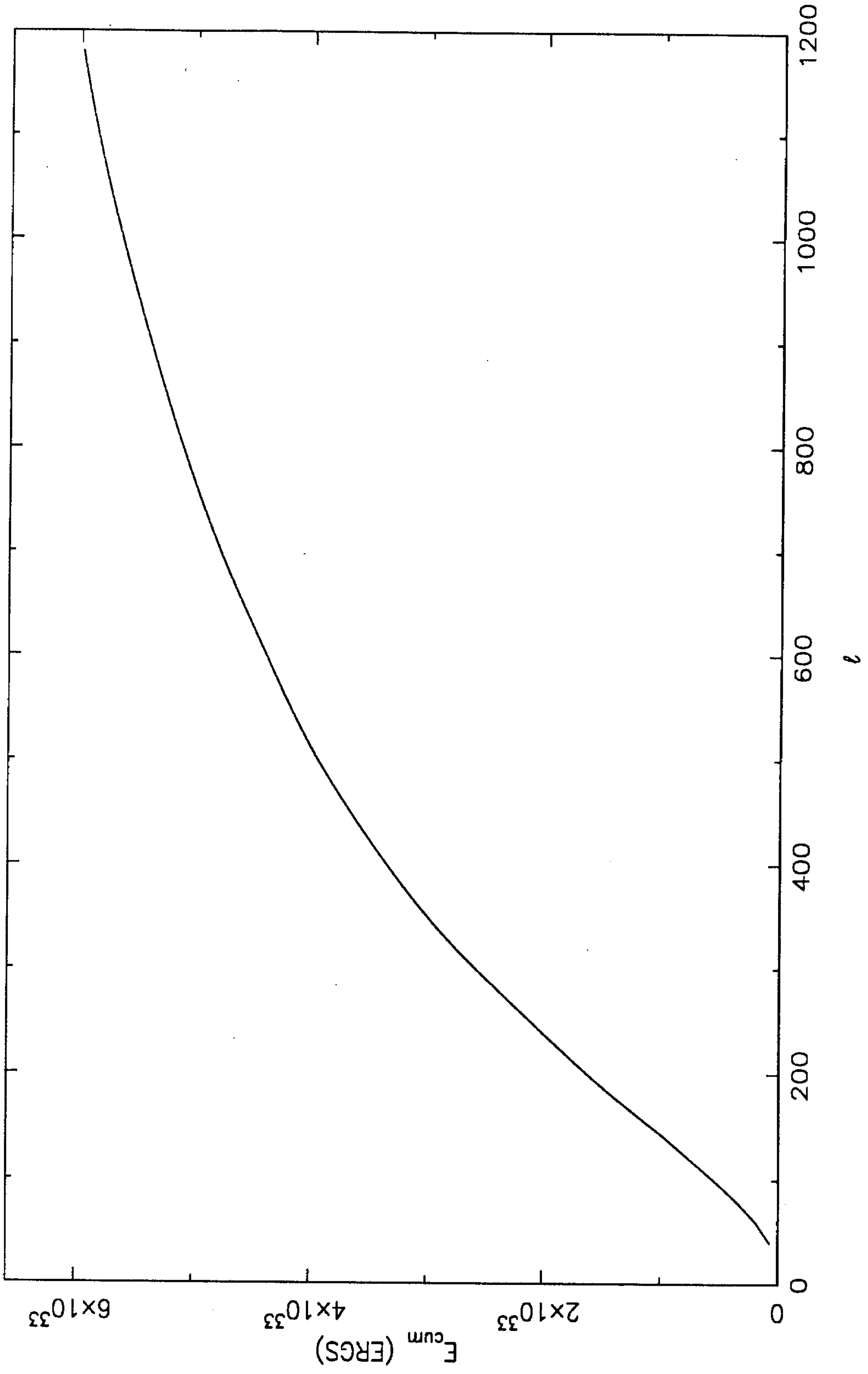

0
200
400
600
800
1000
1200
ℓ
0
2×10^{33}
4×10^{33}
6×10^{33}
E_{cum} (ERGS)

Fig. 4.25

CHAPTER 5

Accuracy of the Seeing Correction

5.1 Introduction

In this chapter, we shall consider a very difficult issue—the accuracy of the seeing-correction technique described in Chapter 4. In short, we have no easy way, at present, to quantitatively assess the accuracy of the seeing correction. We can, however, address several topics that we believe will make the seeing measurements and corrections more plausible. First, we briefly consider the choice of the PSF. That is, does our choice for the PSF accurately model the properties of the atmosphere and telescope optics? Second, we briefly address any possible systematic errors that may have been introduced by our choice for the PSF. Finally, we describe a test of the seeing-correction technique that we performed using the 1989 March 7 partial solar eclipse. It should be noted that this test is not a perfect test. That is, a negative result indicates that the seeing-correction technique is flawed, whereas a positive result indicates that the technique is self-consistent, but still possibly flawed. The ultimate test, of course, is to compare our results with space-based observations. This should be feasible in the mid-1990s when the NASA/ESA Solar and Heliospheric Observatory (SOHO) flies. Among the instruments on this spacecraft will be the the Solar Oscillations Imager (SOI), which uses a Michelson Doppler Interferometer (MDI) as a velocity analyzer. This instrument is expected to see out to $\ell \sim 4000$ (Domingo 1988; Scherrer *et al.* 1988; and Hoeksema, Scherrer, Title, and Tarbell 1988).

5.2 The Choice of the PSF

When the seeing-correction technique was developed, several different choices for the PSF were considered. The obvious choice of a single Gaussian was tried, but the two-Gaussian PSF with three free parameters, σ_1, σ_2, and α, yielded much better fits to the limb profiles. This is the primary reason for the choice of Eq. (4.2) as the PSF. Furthermore, the PSF given by Eq. (4.2) allows the following, very physical association to be made: $S_1(x)$ (the narrow, large-amplitude Gaussian) is related to blurring produced by the actual atmospheric seeing and by the optical system, and $\alpha S_2(x)$ (the wide, small-amplitude Gaussian) is related to scattered light produced by the atmosphere and by the telescope optics.

This association is consistent with the seeing measurements in Tsay *et al.* (1990), in which Anderson Mesa (at an elevation of 2198 m), near Flagstaff, AZ, is evaluated as a possible site for the location of an optical interferometric array. In this work they used an $f/11$, 14-inch Celestron telescope, a CCD camera, and an image processor to measure the FWHM of instantaneous stellar images. For each of their seeing measurements, they collected 60 32×32 pixel images of a bright star at video rates. They found that a single Gaussian adequately fit the one-dimensional stellar profile, with typical FWHMs of 1–2$''$. Their measurements were taken in the nighttime desert skies, which are presumably more transparent than the skies over Big Bear Lake (which is adjacent to the Los Angeles Basin). Furthermore, their optical system is considerably simpler than ours; i.e, they have no large pieces of glass or crystal (such as in the Zeiss filter), and they have fewer exposed mirrors and ancillary filters (which are excellent dust-collecting surfaces). Given these differences between the two systems, one would expect there to be less scattered light in the Anderson Mesa measurements, and therefore, the two choices for PSFs are not inconsistent with each other. Also, their FWHM values for the nighttime seeing are consistent with our daytime values of $\sim 4''$.

Subsequent to the completion of this work, we discovered that others have used a two-Gaussian PSF as a model for seeing. Lévy (1971) measured the brightness power spectrum of the solar granulation during the 1966 May 20 eclipse. The data consist of 10 photographs of the granulation and the lunar limb (at 5300 Å) made with 1/580 sec exposure times. The limb of the Moon in front of the Sun was used to measure the PSF in a manner similar to that described in Chapter 4 and § 5.4 below; however, their model for the PSF was slightly different from the one used in Chapter 4:

$$S(x) = \frac{1}{a}e^{-(x/a)^2} + \frac{1}{b}e^{-(x/b)^2}. \tag{5.1}$$

They find that the average FWHM for their PSF is $\sim 0.8''$. Deubner and Mattig (1975) essentially repeated these observations using the 1973 June 30 partial eclipse. Their data consist of six granulation/lunar limb images (at 6070 Å), which were selected out of total of about 21,000 exposures (made at a rate of 18 frames/sec). Using the same PSF model in Eq. (5.1), they find a FWHM of $\sim 0.5''$.

At first sight, the order-of-magnitude difference in PSF FWHMs from our data and from that of Lévy and of Deubner and Mattig seems quite disconcerting. One wonders if the seeing can be that substantially different between BBSO and these other sites. There are three parts to a possible explanation for this discrepancy, all of which are true to some degree. The first is simply that the seeing was better during the granulation measurements. BBSO (at an elevation of 2,067 m) is a site that is capable of having very good seeing; however, our measurements were made on days that were considered average for the seeing at BBSO. Deubner and Mattig's measurements were made at the Observatorio del Teide at Izaña, Tenerife in the Canary Islands. This observatory is at an elevation of 2,400 m, and is usually well above the inversion layer, and is surrounded by a large body of water (the Atlantic Ocean). These factors make for a site with excellent seeing characteristics, as the surrounding air mass is very homogeneous. Lévy's data were taken at the Pic-du-Midi Observatory (at an elevation of 2861 m), another site known for excellent seeing characteristics.

The second half of the explanation is that the optical system used in our measurements (see Fig. 3.1), specifically the filter, is very complex. The Zeiss birefringent filter used in our measurements consists of $\sim$ 40 crystal or glass elements (which have a total length of about 40 cm), each of which could introduce a small amount of defocussing. The net blurring effect from these and other ancillary optical elements is no doubt considerable. As discussed above, the sheer bulk of the optics in the Zeiss filter must also introduce considerable scattered light into our measurements, thereby contributing further to the width of the PSF. On the other hand, the optical systems used in the granulation measurements were very simple, consisting of the telescope, an interference filter, and a camera. This explanation is further substantiated by noting that σ_1 (the primary contributor to the FWHM of our PSF) is 2–4 times as big as σ_{x_0} (see Fig. 3.7 and also Figs. 5.4 and 5.5). In other words, the effects of image blurring are 2–4 times those of image motion. This suggests that the atmospheric image-blurring component of the PSF has been artificially enhanced. This is consistent with the above discussion concerning the complexity of our optical system.

Finally, the third part of the explanation is that, at least in the case of the Deubner and Mattig data, the very best images out of a set of many were selected for analysis; in particular, they chose the best 0.03% of their images. It is not clear from Lévy's paper if a similar technique was used, but given standard solar observational techniques, it is most likely that a movie of the eclipse was made and some form of image selection was employed. The technique of image selection is known to give improvements in the image quality by a factor of 2–4 (Beckers 1989). Image selection was not practical in our Doppler observations because of the requirement for an evenly spaced time sequence of images, and because of the inordinately large quantity of data that would be generated. Given all of these factors, it is not so surprising that the PSF FWHMs measured by Lévy and by Deubner and Mattig are so much better than ours.

5.3 Systematic Errors in the PSF

One of the most obvious features of the MTFs shown in Figs. 4.8a and b are the kinks that appear at $\ell \sim 170$. One might think that these kinks are a result of the two-Gaussian PSF used; however, we believe that these are real features in the MTFs. We tried several other PSFs of the form

$$S(x) = \frac{1}{\sum_{i=1}^{N} \alpha_i} \sum_{i=1}^{N} \alpha_i S_i(x) \tag{5.2}$$

with the σ_i in the $S_i(x)$ fixed and having a geometric ratio, i.e., $\sigma_n = 2^{n-1}\sigma_1$, and with the α_i all free parameters. Sums of Gaussians with up to $N = 5$ were tried. These PSFs are less physical than Eq. (4.2); i.e., physical properties cannot as easily be associated with the different terms, as was done above. However, they are more general than Eq. (4.2), and they always produced MTFs that essentially agreed with the ones in Figs. 4.8a and b. It is interesting to note that the MTFs produced by Lévy (1971) and Deubner and Mattig (1975) in their granulation brightness power spectrum measurements (described in § 5.2) also exhibit the same kink. We therefore conclude that the aforementioned kinks are real features in the MTFs, and are most likely a result of both atmospheric blurring and scattered light influencing the MTFs.

5.4 The 1989 March 7 Eclipse Test of the Seeing Measurements

As stated before, we can think of the atmosphere as a low-pass spatial filter. By measuring the inputs and outputs of this filter we are able to determine the properties of the filter, i.e., the MTF. One way to test this procedure would be to subject the filter to different inputs, measure the outputs, and see if the resulting MTFs are the same. One should note that this is not a perfect test. If the resulting MTFs are different, then there is a flaw in the procedure. However, if the MTFs come out the same, then the procedure is self-consistent, but may still contain flaws. We had the unique opportunity to perform such a test using the partial solar eclipse of 1989 March 7, with the two different inputs being the solar limb as seen on the background of space, and the lunar limb as seen in front of the solar disk. The path of the Moon across the solar disk, as seen from BBSO, is shown in Fig. 5.1. The model used to describe the seeing is still that of Eqs. (4.1) and (4.2). The unsmeared solar limb profile, $L_{\odot}(x)$, is still that given in Eq. (4.6); the unsmeared lunar limb profile is a step function given by

$$L_{☾}(x) = \begin{cases} I_0^* & \text{if } x < R_{☾}; \\ 0 & \text{if } x \geq R_{☾}. \end{cases} \tag{5.3}$$

I_0^* is the intensity of the Sun in the vicinity of the lunar limb and $R_{☾}$ is the lunar radius. It varies gradually, depending on the position of the Moon, and is a result of limb darkening. I_0^* is *not* the intensity of the Sun at the center of the solar disk. It should be noted that Eq. (5.3) is not completely valid when the lunar limb is near the solar limb, i.e., in regions of rapid change in the intensity of the solar disk due to limb darkening. This occurs at the beginning and end of the eclipse. Essentially what happens here is that the "top of the step" in the step function is no longer flat. The result of using this step-function limb profile in these regions is an underestimation of the actual MTF, i.e, overestimating the severity of the seeing.

The telescope optics and data acquisition system used to collect solar and lunar limb profiles were essentially the same as that described in §§ 3.3 and 4.2, with the VMG system mounted on the 25 cm (10 in) vacuum refractor. The data acquisition software was set up to collect limb profiles from the positions shown in Fig. 4.1. This necessitated that both the solar and lunar limb cut through the camera field of view (FOV) approximately vertically. In order to satisfy this requirement, the camera was mounted on a rotatable stage, which allowed the operator to adjust the camera angle to compensate for the changing limb orientation. The camera angles were predetermined for five-minute intervals, so that given the time, one could look up the appropriate camera angle to within 2.5 minutes. This amounted to, at most, a 3° error in the camera angle. Fig. 5.2 shows the Sun/Moon positions and the camera FOVs for three different times. Fig. 5.3 is a photograph of the eclipse taken through the BBSO 20 cm (8 in) Singer-Link refractor. Finally, the

Table 5.1

Eclipse Observational Parameters

Date	1989 March 7
Time of first contact (UT)	16:57
Time of last contact (UT)	18:48
Time of maximum coverage (UT)	17:52
Maximum coverage	29%
No. of profiles per sample	36
No. of solar limb samples	68
Total no. of solar limb profiles	2448
No. of lunar limb samples	66
Total no. of lunar limb profiles	2376
Horizontal images scale, S_H	$0.527''$/pixel
No. of pixels	128
Profile size	$67.4''$
Qualitative seeing	fair

relevant parameters describing the eclipse and the two limb profile data sets are shown in Table 5.1

It should be noted that these eclipse observations were a very exacting task, given that two other observing programs (on two different regions) had to be satisfied using three telescopes, all of which were essentially mounted on the same spar. These difficulties were overcome by extensive planning in which it was decided what each of the observer's responsibilities would be and the order in which the observations were to be carried out, and by the preparation of elaborate checklists. Furthermore, it was decided to hold dynamic redirection to a minimum by allowing only one person (the Chief Observer) access to the telescope control paddle. All requests for telescope repointing went through this person. Despite an addition to the observing program (at the very last minute), all the observing goals were successfully met. The BBSO observing staff should be complimented for their skill in carrying out these observations.

The limb profile analysis is the same as that described in § 4.4. Each limb profile was fit to the model given in Eq. (4.5). Eq. (4.6) was used for the unsmeared limb profile for the solar limb profiles. Since the unsmeared lunar limb profile is much simpler than that of the solar limb profile, Eq. (4.5) reduces to the much simpler, analytical form for the lunar limb profiles

$$\mathcal{L}_{☾}(x) \rightarrow \frac{I_0^*}{2}\left\{1 - \frac{1}{1+\alpha}\left[\mathrm{erf}\left(\frac{x - x_0 - R_{☾}}{\sqrt{2}\sigma_1}\right) + \alpha\,\mathrm{erf}\left(\frac{x - x_0 - R_{☾}}{\sqrt{2}\sigma_2}\right)\right]\right\}, \qquad (5.4)$$

where we have used Eq. (5.3) in place of $L_{\odot}(x)$ in Eq. (4.5). The five fit parameters, I_0 (or I_0^*), $\sigma_1, \sigma_2, \alpha$, and x_0, were corrected for the same effects described in § 4.4. Fig. 5.4 shows $I_0, \sigma_1, \sigma_2, \alpha$, and σ_{x_0} from one limb sample position, as a function of time, for the solar limb profiles; Fig. 5.5 shows $I_0^*, \sigma_1, \sigma_2, \alpha$, and σ_{x_0} from one limb sample position for the lunar limb profiles. In Fig. 5.5., there is a noticeable decrease in I_0^* at the beginning and end of the eclipse. As described above, this is a result of the variation in I_0^* with lunar limb position. Note that there is a very slight increase in α at the beginning and end of the eclipse. This is because the Moon is near the solar limb, and at that point, as described above, $L_{☾}(x)$ is a bad approximation of the unsmeared lunar limb profile because of the rapid variation in I_0^* due to limb darkening. The average PSF FWHM determined from these parameters is $\sim 2.8''$. Note that this FWHM is somewhat better than the FWHM determined from the seeing measurements described in Chapter 4.

The MTF is, again, given by Eq. (4.9). $\mathrm{MTF}_{\odot}(\ell, t)$ is shown in Fig. 5.6a, and $\mathrm{MTF}_{☾}(\ell, t)$ is shown in Fig 5.6b. The edge effects, which result from the breakdown of Eq. (5.3) at the limb, show up quite clearly in $\mathrm{MTF}_{☾}(\ell, t)$ as a decrease in the MTF at high ℓ. Finally, Fig. 5.7 shows the time-averaged MTFs. The average lunar MTF is slightly less that the average solar MTF at high ℓ, but this is attributable to the average's being pulled down by the artificially lowered lunar MTFs at the beginning and end of the eclipse. Other than this small difference, we see that the two MTFs are in quite good agreement with each other. This result lends credence to the seeing-correction technique. It does not prove that the technique is correct. However, had the two MTFs been different, this would have been cause for worry... to put it mildly!

Figure Captions

Figure 5.1: The path of the Moon across the face of the Sun for the partial solar eclipse of 1989 March 7, as seen from BBSO. The Moon is shown at three different instances: time of first contact, time of maximum coverage, and time of last contact.

Figure 5.2: A schematic showing the camera field of views (FOVs) for the three different Sun/Moon positions shown Fig. 5.1 (represented here by a dashed line, a dot-dashed line, and a dot-dot-dot-dashed line). The small rectangles represent the camera FOVs and the camera angles for each of the three times. Within each rectangle, limb profiles are taken, as in Fig. 4.1. I thank Dr. Dale Gary for his help in producing this figure and Fig. 5.1.

Figure 5.3: A photograph of the 1989 March 7 partial solar eclipse taken near the time of maximum coverage. The two small, white lines indicate the location and orientation of the solar and lunar limb profiles.

Figure 5.4: The averaged, corrected limb fit parameters from one of the four limb sample positions (shown in Fig. 4.1) for the solar limb profiles. The image scale is 0.527″/pixel. From the top down, the curves are: 1) I_0 (dashed line) measured in relative units; 2) σ_2 (solid line) measured in pixels; 3) σ_{x_0} (dot-dashed line) measured in pixels; 4) σ_1 (solid line) measured in pixels; 5) α (dashed line) measured in absolute dimensionless units. Taken separately, any of these five quantities as a function of time are not completely indicative of the seeing. The seeing can be interpreted only through the modulation transfer function (MTF).

Figure 5.5: Same as Fig. 5.4, except for the lunar limb profiles (with I_0^* replacing I_0).

Figure 5.6: The MTF shown as a function of spatial frequency (or spherical harmonic degree ℓ) and time. This is Eq. (4.9). (a) The MTF as derived from the solar limb profiles. (b) The MTF as derived from the lunar limb profiles. Note that there

is a slight decrease in the lunar-derived MTF at high ℓ at the beginning and end of the eclipse that results from a breakdown of Eq. (5.3).

Figure 5.7: The solar- and lunar-derived MTFs averaged over the duration of the eclipse. The two MTFs are essentially identical, thereby increasing the confidence level of the seeing-correction technique.

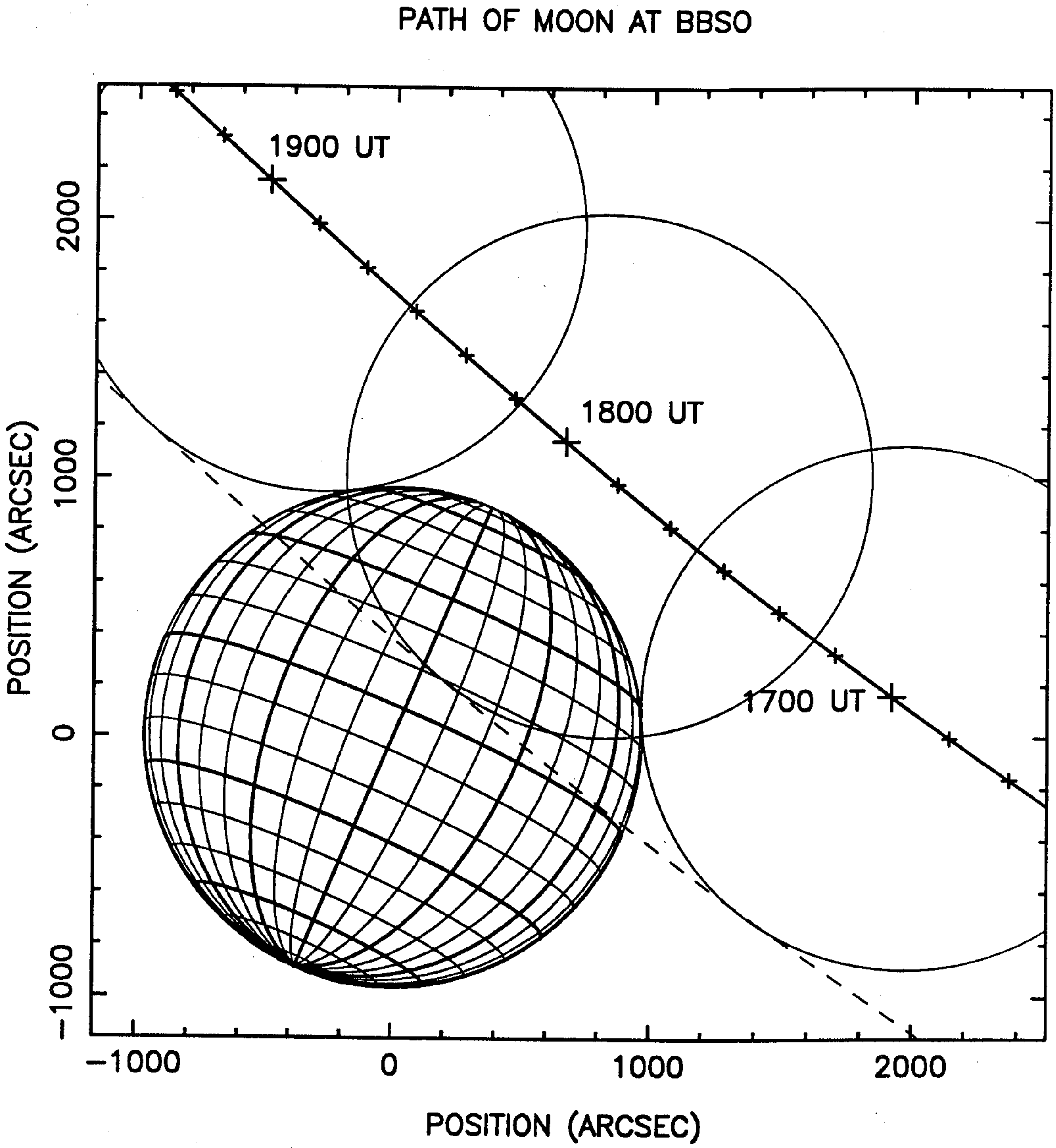
PATH OF MOON AT BBSO
1900 UT
1800 UT
1700 UT
2000
1000
0
−1000
POSITION (ARCSEC)
−1000
0
1000
2000
POSITION (ARCSEC)

Fig. 5.1

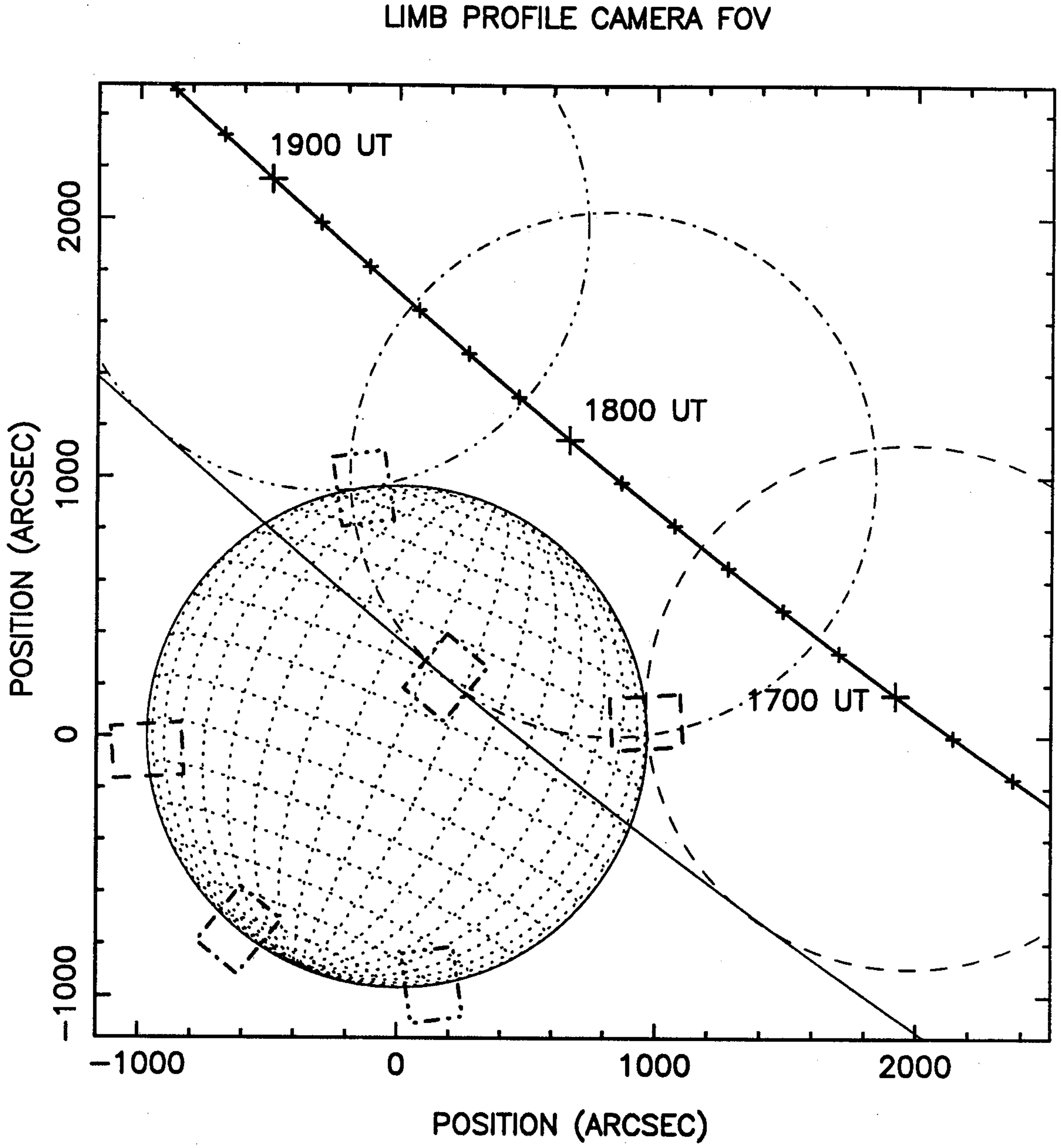
LIMB PROFILE CAMERA FOV
1900 UT
1800 UT
1700 UT
POSITION (ARCSEC)
POSITION (ARCSEC)
-1000
0
1000
2000
-1000
0
1000
2000

Fig. 5.2

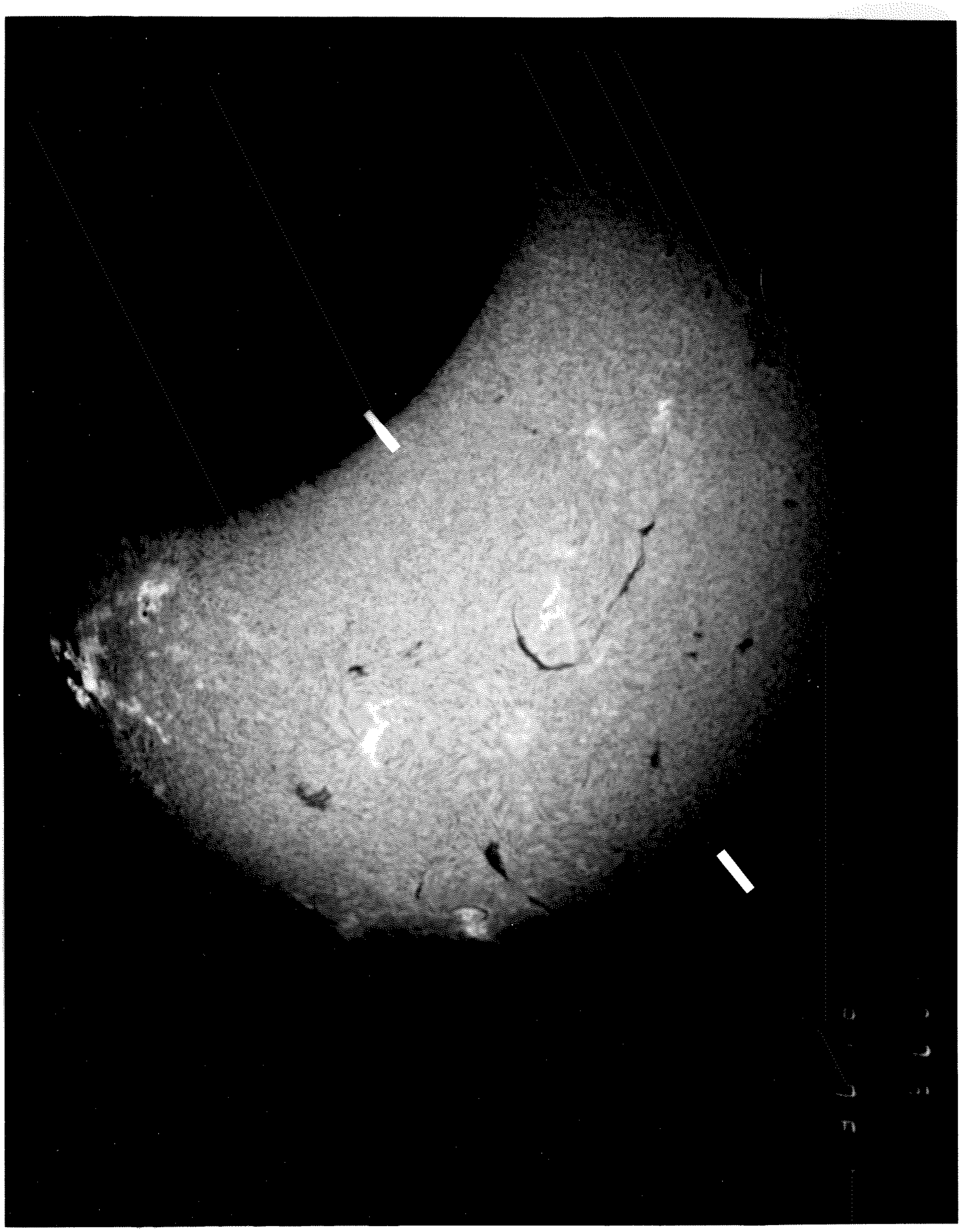

Fig. 5.3

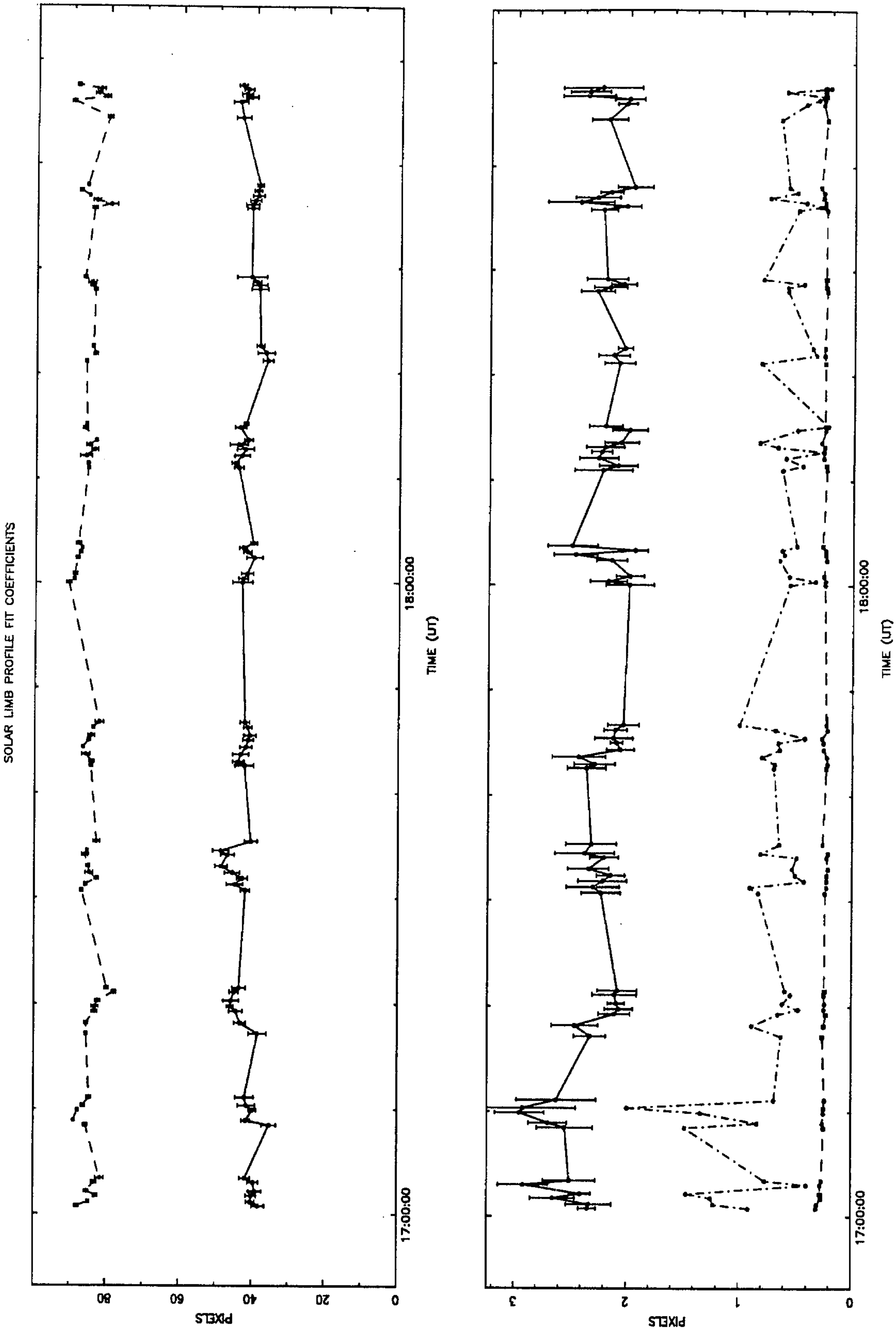
SOLAR LIMB PROFILE FIT COEFFICIENTS
PIXELS
80
60
40
20
0
TIME (UT)
17:00:00
18:00:00
PIXELS
3
2
1
0
TIME (UT)
17:00:00
18:00:00

Fig. 5.4

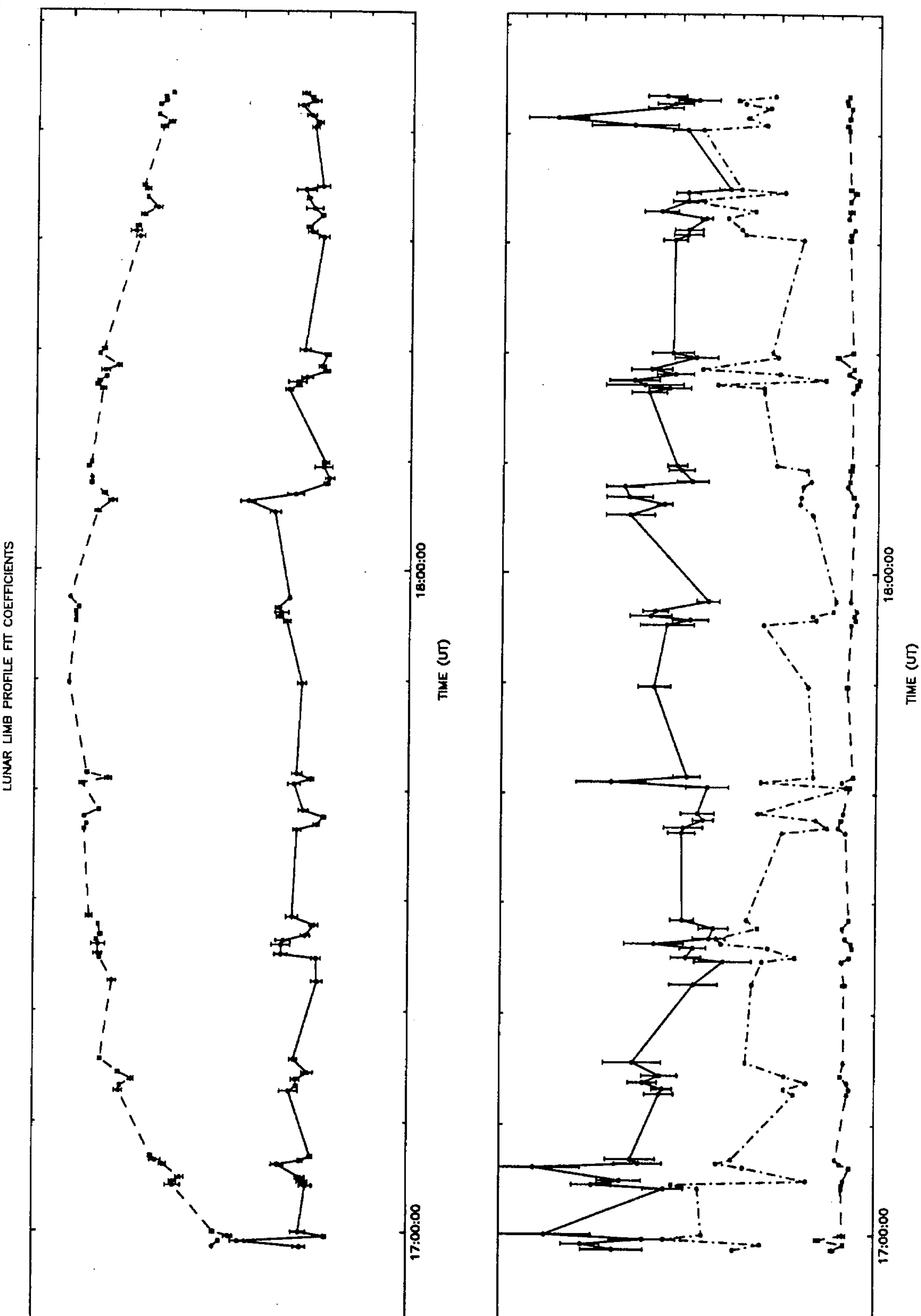
LUNAR LIMB PROFILE FIT COEFFICIENTS
PIXELS
0
20
40
60
80
TIME (UT)
17:00:00
18:00:00
PIXELS
0
1
2
3
TIME (UT)
17:00:00
18:00:00

Fig. 5.5

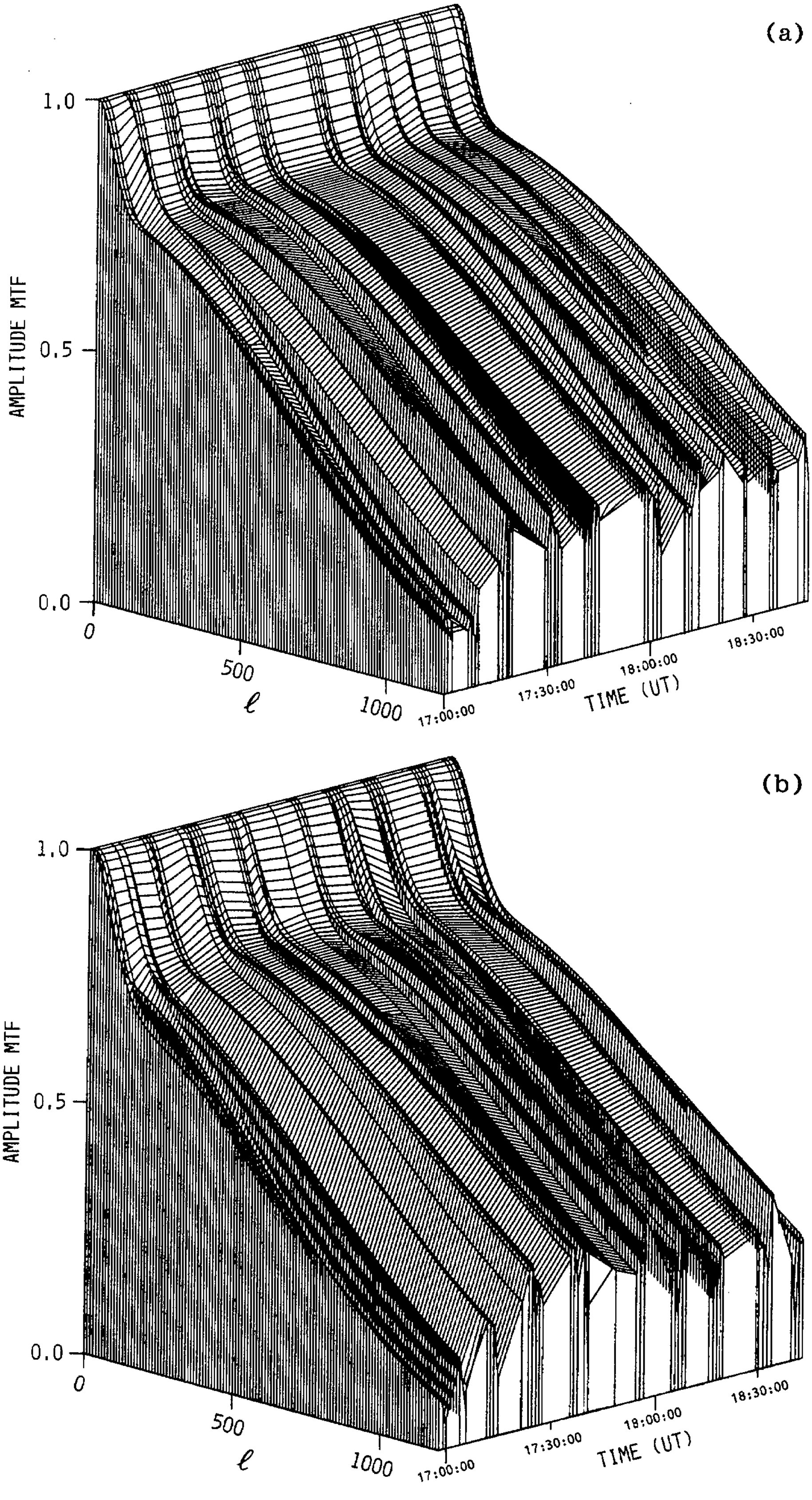
(a)
1.0
0.5
0.0
AMPLITUDE MTF
0
500
1000
ℓ
17:00:00
17:30:00
18:00:00
18:30:00
TIME (UT)
(b)
1.0
0.5
0.0
AMPLITUDE MTF
0
500
1000
ℓ
17:00:00
17:30:00
18:00:00
18:30:00
TIME (UT)

Fig. 5.6

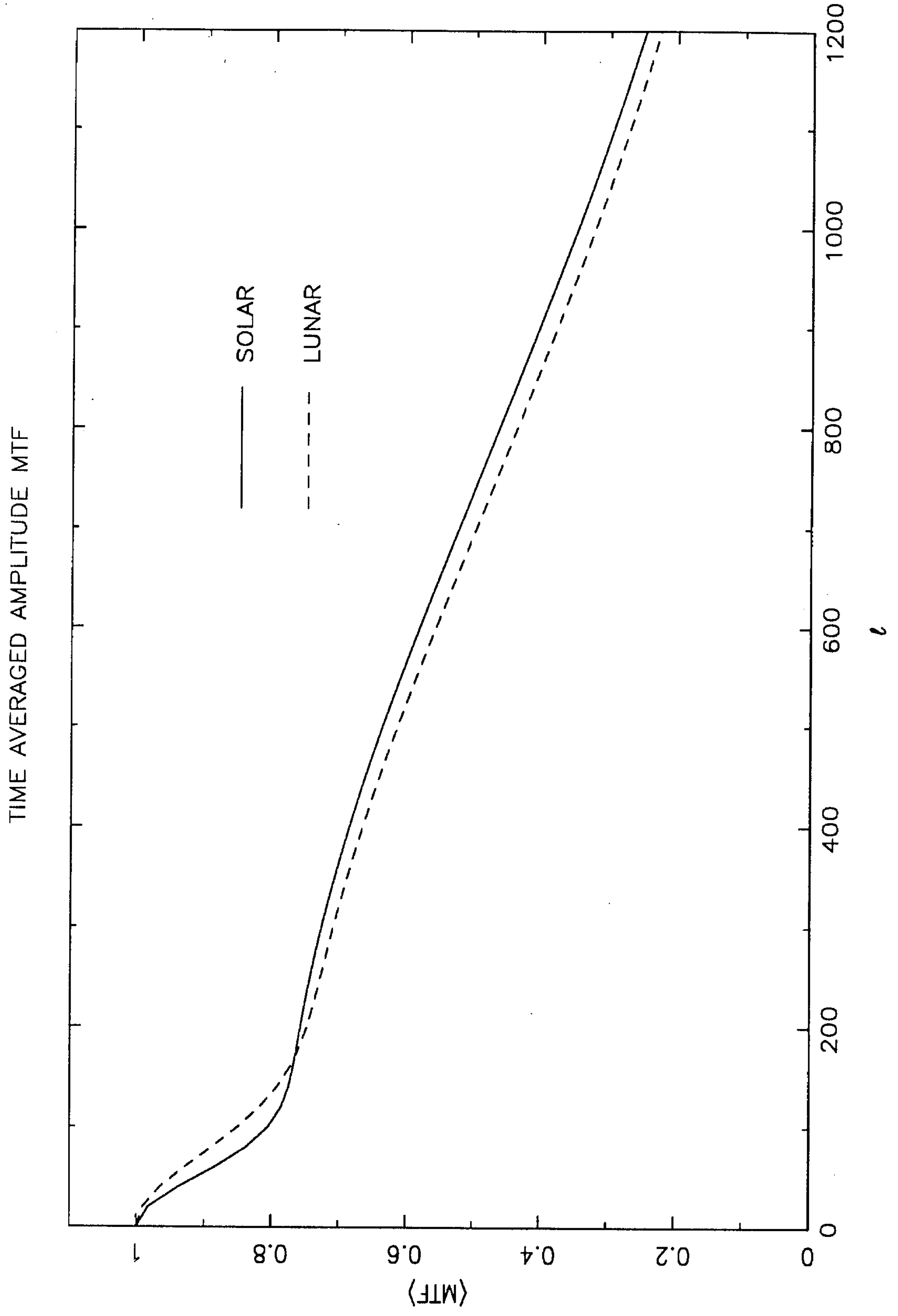
TIME AVERAGED AMPLITUDE MTF
SOLAR
LUNAR
⟨MTF⟩
1
0.8
0.6
0.4
0.2
0
ℓ
0
200
400
600
800
1000
1200

Fig. 5.7

APPENDIX I

The frequencies resulting from the ridge-fitting technique used in Chapter 3 are approximations of the actual mode frequencies. Each ridge peak is actually comprised of many individual mode peaks that result from power from modes with different ℓ' leaking into the power spectrum at ℓ. The centroid of this collection of mode peaks is used to approximate the actual $m = 0$ mode frequencies. We discuss here the corrections for the key systematic error in this procedure.

For a given ridge n, each ridge peak at ℓ consists of a peak from the actual mode frequency, at $\nu_{n\ell}$, and sideband peaks from nearby modes, at $\nu_{n\ell'}$. The measured centroid of this collection of mode peaks is the result of the ridge-fitting procedure, and is at $\nu'_{n\ell}$. Therefore, the error in the measurement of $\nu_{n\ell}$ (after dropping the subscript n) is

$$\Delta\nu_\ell = \nu_\ell - \nu'_\ell. \tag{A.I.1}$$

The measured frequency is the weighted sum of all the different frequencies present in the spectrum at ℓ. Therefore,

$$\nu'_\ell = \frac{\sum_{\ell'} \nu_{\ell'} P_{\ell\ell'}}{\sum_{\ell'} P_{\ell\ell'}}, \tag{A.I.2}$$

where $P_{\ell\ell'}$ is the power from the ℓ'th mode that has leaked into the ℓth power spectrum. The measurement error then becomes

$$\Delta\nu_\ell = \frac{\sum_{\ell'} \Delta\nu_{\ell'} P_{\ell\ell'}}{\sum_{\ell'} P_{\ell\ell'}}, \tag{A.I.3}$$

where $\Delta\nu_{\ell'} = \nu_\ell - \nu_{\ell'}$. $P_{\ell\ell'}$ can be expressed in terms of an overlap function

$$P_{\ell\ell'} = V(\ell,\ell')P_{\ell'}, \tag{A.I.4}$$

where $V(\ell,\ell')$ is the fractional amount of the ℓ' mode leaking into the ℓth power spectrum. In other words, $V(\ell,\ell') = |\langle\psi_\ell|\psi_{\ell'}\rangle|^2$, where ψ_ℓ is the eigenfunction of the ℓth mode. $P_{\ell'}$, above, is the power in mode ℓ'. So, Eq. (A.I.3) becomes

$$\Delta\nu_\ell = \frac{\sum_{\ell'} \Delta\nu_{\ell'} V(\ell,\ell')P_{\ell'}}{\sum_{\ell'} V(\ell,\ell')P_{\ell'}}. \tag{A.I.5}$$

Now, $P_{\ell'}$ can be expressed in terms of P_ℓ:

$$P_{\ell'} = P_\ell(\ell + \Delta\ell), \tag{A.I.6}$$

where $\Delta\ell = \ell - \ell'$. After performing a Taylor expansion on Eq. (A.I.6), we get

$$P_{\ell'} \approx P_\ell \left(1 + \Delta\ell \frac{d \ln P_\ell}{d\ell}\right). \tag{A.I.7}$$

Substituting this into Eq. (A.I.5), and after noting that

$$\Delta\nu_{\ell'} = \Delta\ell \frac{d\nu}{d\ell}, \tag{A.I.8}$$

we get

$$\Delta\nu_\ell \approx \frac{\sum_{\ell'} \Delta\ell \frac{d\nu}{d\ell} V(\ell,\ell') \left(1 + \Delta\ell \frac{d \ln P_\ell}{d\ell}\right)}{\sum_{\ell'} V(\ell,\ell') \left(1 + \Delta\ell \frac{d \ln P_\ell}{d\ell}\right)}. \tag{A.I.9}$$

We now assume that $V(\ell,\ell')$ is given by

$$V(\ell,\ell') = \exp\left[-\frac{(\Delta\ell - \alpha)^2}{2s^2}\right], \tag{A.I.10}$$

where $\alpha = \epsilon\ell$ represents a small scale error, and s is the approximate number of modes leaking into the ℓth power spectrum. After substituting for $V(\ell,\ell')$ in Eq. (A.I.9) and letting the sums go to integrals, we get

$$\Delta\nu \approx s^2 \frac{d\nu}{d\ell} \frac{1}{P_\ell} \frac{\partial P_\ell}{\partial \ell} + \epsilon\ell \frac{d\nu}{d\ell}, \tag{A.I.11}$$

where we have dropped negligible terms in α^2 and $\alpha\, d(\ln P_\ell)/d\ell$. This is the result obtained by Libbrecht and Kaufman (1988).

We are now faced with the task of evaluating s. For full-disk, spherical harmonic decompositions (as in the low- and intermediate-ℓ analyses in Libbrecht, Woodard, and Kaufman 1990), s is found to be approximately 2. In this case, the mode linewidths are smaller than the spacing between the leakage modes, and s can be determined essentially by counting the leakage modes. In the case of partial disk, Fourier-transform decompositions, s is not easily evaluated because of the artificially large linewidths. This makes counting the leakage modes difficult. In this case, we shall explicitly calculate $V(\ell, \ell')$ to find s.

The plane-wave approximation to a spherical harmonic is

$$\psi_\ell = e^{-2\pi i k x}, \tag{A.I.12}$$

where k is an integer, $\ell = k\, d\ell/dk$ ($d\ell/dk$ is the scale factor), and $x \in [0,1]$ and is defined over the observing window. Then,

$$\begin{aligned} \langle \psi_\ell | \psi_{\ell'} \rangle &= \int_0^1 e^{2\pi i k x} e^{-2\pi i k' x} dx \\ &= e^{\pi i (k-k')} \operatorname{sinc}\left[\pi(k-k')\right]. \end{aligned} \tag{A.I.13}$$

Therefore, we find that

$$V(\ell, \ell') = \operatorname{sinc}^2 \frac{\pi \Delta \ell}{d\ell/dk}. \tag{A.I.14}$$

We can approximate Eq. (A.I.14) by Eq. (A.I.10), which will allow us to approximate s, and to continue using the formalism developed in Eq. (A.I.11). We make the approximation by matching up the half width at half maxima (HWHMs) of the two functions. For the the Gaussian, the HWHM is

$$\mathrm{HWHM} = \sqrt{2 \ln 2}\, s, \tag{A.I.15}$$

and for the sinc^2 function, the HWHM is

$$\mathrm{HWHM} = 0.442946 \frac{d\ell}{dk}. \tag{A.I.16}$$

By equating these two HWHMs, we obtain

$$s = 0.376204 \frac{d\ell}{dk}. \tag{A.I.17}$$

This value of s can be used in Eq (A.I.11), and corrections for systematic errors can be made to the ridge-fit frequencies.

APPENDIX II

In order to properly measure the velocity power of the low-ℓ, we must calculate the frequency response, or modulation transfer function (MTF) of a best-fit linear subtraction filter. That is, given an input $f_{\rm in}(x)$, and the least-squares linear fit to the input, $g(x)$, we want the power spectrum of the difference, $f_{\rm out}(x) = f_{\rm in}(x) - g(x)$. Let the input be

$$\begin{aligned} f_{\rm in}(x) &= \sin(kx + \phi) \\ &= A \sin kx + B \cos kx, \end{aligned} \tag{A.II.1}$$

where $A = \cos\phi$ and $B = \sin\phi$. Let the linear least-squares fit to $f_{\rm in}(x)$ be

$$g(x) = a + bx \tag{A.II.2}$$

and the difference be

$$f_{\rm out}(x) = f_{\rm in}(x) - g(x). \tag{A.II.3}$$

Expressed as a Fourier series, this is

$$f_{\rm out}(x) = \sum_{j=1}^{\infty} A'_j \sin jx + B'_j \cos jx. \tag{A.II.4}$$

The power in the jth frequency component is

$$P_k(j) = A'^2_j + B'^2_j \tag{A.II.5}$$

and the MTF of this filter is

$$\mathrm{MTF}_k(j) = \langle P_k(j) \rangle, \tag{A.II.6}$$

where $\langle\ \rangle$ denotes an average over all phase angles ϕ.

We must first calculate $g(x)$ by minimizing

$$\chi^2 = \int_0^{2\pi} (f_{\rm in}(x) - a - bx)^2 \, dx \tag{A.II.7}$$

with respect to a and b. Of course, a line is not a very good approximation to a function like $f_{\text{in}}(x)$ given in Eq (A.II.1). Recall that the goal here is not accurate modeling, but, instead, filtering of an input signal. We find that

$$a = \frac{3A}{\pi k} \tag{A.II.8a}$$

and

$$b = -\frac{3A}{\pi k}\frac{1}{\pi}. \tag{A.II.8b}$$

Therefore, the least-squares linear fit is

$$g(x) = \frac{3A}{\pi k}\left(1 - \frac{x}{\pi}\right) \tag{A.II.9}$$

and the filter output is

$$f_{\text{out}}(x) = A\sin kx + B\cos kx - \frac{3A}{\pi k}\left(1 - \frac{x}{\pi}\right). \tag{A.II.10}$$

Calculating the Fourier series of $f_{\text{out}}(x)$ (Eq. A.II.4), we find that the Fourier coefficients are

$$\begin{aligned} A'_j &= A\delta_{jk} - \frac{6A}{\pi^2 jk} \\ B'_j &= B\delta_{jk}. \end{aligned} \tag{A.II.11}$$

Therefore, Eq. (A.II.5) becomes

$$P_k(j) = \left(1 - \frac{12A^2}{\pi^2 jk}\right)\delta_{jk} + \frac{36A^2}{\pi^4 j^2 k^2}, \tag{A.II.12}$$

where we have used the fact that $A^2 + B^2 = 1$. Finally, averaging over all phase angles, we get the MTF of the filter:

$$\text{MTF}_k(j) = \left(1 - \frac{6}{\pi^2 jk}\right)\delta_{jk} + \frac{18}{\pi^4 j^2 k^2}, \tag{A.II.13}$$

where we have used the fact that $\langle A^2 \rangle = \langle \cos^2\phi \rangle = \frac{1}{2}$.

I am indebted to Dr. Martin F. Woodard for his guidance in carrying out this calculation.

REFERENCES

Ando, H., and Osaki, Y. 1975, *Publ. Astron. Soc. Japan* **27**, 581.

Antia, H. M., Chitre, S. M., and Narashima, D. 1986, *Astrophys. Space Sci.* **118**, 169.

Beckers, J. M. 1989, in *Solar and Stellar Granulation*, eds. R. J. Rutten and G. Severino (Dordrecht: Kluwer), p. 55.

Brown, T. M. 1984, *Science* **226**, 687.

Brown, T. M., Mihalas, B. W., and Rhodes,E. J., Jr. 1986, in *Physics of the Sun*, Vol. I, *The Solar Interior*, eds. P. A. Sturrock, T. E. Holzer, D. M. Mihalas, and R. K. Ulrich (Dorddrecht: Reidel).

Campbell, W. R., and Roberts, B. 1989, *Ap. J.* **338**, 538.

Christensen-Dalsgaard, J. 1988a, in *IAU Symposium 123, Advances in Helio- and Asteroseismology*, eds. J. Christensen-Dalsgaard and S. Frandsen (Dordrecht: Reidel), p. 3.

Christensen-Dalsgaard, J. 1988b, in *Seismology of the Sun and Sun-like Stars*, ed. E. J. Rolfe (Noordwijk: ESA), p. 431.

Christensen-Dalsgaard, J. 1990, in *Inside the Sun*, eds. G. Berthomieu and M. Cribier (Dordrecht: Kluwer), p. 305.

Christensen-Dalsgaard, J., and Berthomieu, G. 1991, in *The Solar Interior and Atmosphere*, eds. A. N. Cox, W. C. Livingston, and M. S. Matthews (Tucson: University of Arizona Press), in press.

Christensen-Dalsgaard, J, Duvall, T. L., Jr., Gough, D. O., Harvey, J. W., and Rhodes, E. J., Jr. 1985, *Nature* **315**, 378.

Christensen-Dalsgaard, J., and Frandsen, S. 1983, *Solar Phys.* **82**, 469.

Christensen-Dalsgaard, J., Gough, D. O., and Thompson, M. J. 1988, in *Seismology of the Sun and Sun-like Stars*, ed. E. J. Rolfe (Noordwijk: ESA), p. 493.

Clare, F., Kennison, D., and Lackman, B. 1987, *NCAR Graphics User's Guide Version 2.00* NCAR Tech. Note NCAR/TN-283+IA (Boulder: National Center for Atmospheric Research).

Claverie, A., Isaak, G. R., McLeod, C. P., van der Raay, H. B., and Roca Cortés, T. 1979, *Nature* **282**, 591.

Coulman, C. E. 1985, *Ann. Rev. Astron. Astrophys.* **23**, 19.

Cox, A. N., Chitre, S. M., Frandsen, S., and Kumar, P. 1991, in *The Solar Interior and Atmosphere*, eds. A. N. Cox, W. C. Livingston, and M. S. Matthews (Tucson: University of Arizona Press), in press.

Deubner, F.-L. 1975, *Astron. Astrophys.* **44**, 371.

Deubner, F.-L. 1983, *Solar Phys.* **82**, 103.

Deubner, F.-L., and Gough, D. 1984, *Ann. Rev. Astron. Astrophys.* **22**, 593.

Deubner, F.-L., and Mattig, W. 1975, *Astron. Astrophys.* **45**, 167.

Domingo, V. 1988, in *Seismology of the Sun and Sun-like Stars*, ed. E. J. Rolfe (Noordwijk: ESA), p. 363.

Duvall, T. L., Jr., and Harvey, J. W. 1983, *Nature* **302**, 24.

Duvall, T. L., Jr., and Harvey, J. W. 1984, *Nature* **310**, 19.

Duvall, T. L., Jr., and Harvey, J. W. 1986, in *Seismology of the Sun and Distant Stars*, ed. D. O. Gough (Dordrecht: Reidel), p. 105.

Duvall, T. L., Jr., Harvey, J. W., Libbrecht, K. G., Popp, B. D., and Pomerantz, M. A. 1988, *Ap. J.* **324**, 1158.

Evans, D. J., and Roberts, B. 1990, *Ap. J.* **356**, 704.

Evans, J. W. 1949, *J. Opt. Soc. Am.* **39**, 229.

Goldreich, P, and Keeley, D. A. 1977a, *Ap. J.* **211**, 934.

Goldreich, P, and Keeley, D. A. 1977b, *Ap. J.* **212**, 243.

Goldreich, P, and Kumar, P. 1988, *Ap. J.* **326**, 462.

Goldreich, P, and Kumar, P. 1990, *Ap. J.* **363**, 694.

Goodman, J. 1990, private communication.

Gough, D. 1983, *Phys. Bull.* **34**, 502.

Gouttebroze, P., Damé, L., and Malherbe, J. M. 1984, *Mem. Soc. Astron. Ital.* **55**, 245.

Grec, G., Fossat, E., and Pomerantz, M. A. 1980, *Nature* **288**, 541.

Grec, G., Fossat, E., and Pomerantz, M. A. 1983, *Solar Phys.* **82**, 55.

Grigoryev, V. M., and Kobanov, N. I. 1988, *Astron. Astrophys.* **197**, 345.

Harvey, J. 1988, in *Seismology of the Sun and Sun-like Stars*, ed. E. J. Rolfe (Noordwijk: ESA), p. 55.

Harvey, J., and the GONG Instrument Development Team 1988, in *Seismology of the Sun and Sun-like Stars*, ed. E. J. Rolfe (Noordwijk: ESA), p. 203.

Harvey, J. W., Kennedy, J. R., and Leibacher, J. W. 1987, *Sky & Telescope* **74**, 470.

Henning, H. M., and Scherrer, P. H. 1986, in *Seismology of the Sun and Distant Stars*, ed. D. O. Gough (Dordrecht: Reidel), p. 55.

Hill, F. 1984, in *Solar Seismology from Space*, ed. R. K. Ulrich (Pasadena: Jet Propulsion Laboratory), p. 255.

Hill, F. 1988, *Ap. J.* **333**, 996.

Hill, F., and the GONG Site Survey Team 1988, in *Seismology of the Sun and Sun-like Stars*, ed. E. J. Rolfe (Noordwijk: ESA), p. 209.

Hoeksema, J. T., Scherrer, P. H., Title, A .M., and Tarbell, T. D. 1988, in *Seismology of the Sun and Sun-like Stars*, ed. E. J. Rolfe (Noordwijk: ESA), p. 407.

Jiménez, A., Pallé, P. L., Pérez, J. C., Régulo, C. Roca Cortés, T., Isaak, G. R., McLeod, C. P., and van der Raay, H. B. 1988, in *IAU Symposium 123, Advances in Helio- and Asteroseismology*, eds. J. Christensen-Dalsgaard and S. Frandsen (Dordrecht: Reidel), p. 205.

Kaufman, J. M. 1988, in *Seismology of the Sun and Sun-like Stars*, ed. E. J. Rolfe (Noordwijk: ESA), p. 31.

Kidman, R. B., and Cox, A. N. 1984, in *Solar Seismology from Space*, ed. R. K. Ulrich (Pasadena: Jet Propulsion Laboratory), p. 317.

Kneer, F. Newkirk, G., Jr., and von Uexküll, M. 1982, *Astron. Astrophys.* **113**, 129.

Kumar, P., Franklin, J., and Goldreich, P. 1988, *Ap. J.* **328**, 879.

Kumar, P., and Goldreich, P. 1989, *Ap. J.* **342**, 558.

Kumar, P. 1990, private communication.

Lawson, C. L. 1977, *Software for C^1 Surface Interpolation* JPL Publication 77-30 (Pasadena: Jet Propulsion Laboratory).

Leibacher, J. W., and Stein, R. F. 1971, *Astrophys. Lett.* **7**, 191.

Leibacher, J. W., and Stein, R. F. 1981, in *The Sun as a Star*, ed. S. Jordan (Washington, D. C.: NASA), p. 263.

Leighton, R. B. 1959, *Ap. J.* **130**, 366.

Leighton, R. B., Noyes, R. W., and Simon, G. W. 1962, *Ap. J.* **135**, 474.

Lévy, M. 1971, *Astron. Astrophys.* **14**, 15.

Libbrecht, K. G. 1988a, *Space Sci. Rev.* **47**, 275.

Libbrecht, K. G. 1988b, *Ap. J.* **334**, 510.

Libbrecht, K. G. 1988c, in *Seismology of the Sun and Sun-like Stars*, ed. E. J. Rolfe (Noordwijk: ESA), p. 3.

Libbrecht, K. G. 1988d, in *Seismology of the Sun and Sun-like Stars*, ed. E. J. Rolfe (Noordwijk: ESA), p. 131.

Libbrecht, K. G., and Kaufman, J. M. 1988, *Ap. J.* **324**, 1172.

Libbrecht, K. G., and Morrow, C. A. 1991, in *The Solar Interior and Atmosphere*, eds. A. N. Cox, W. C. Livingston, and M. S. Matthews (Tucson: University of Arizona Press), in press.

Libbrecht, K. G., Popp, B. D., Kaufman, J. M., and Penn, M. J. 1986, *Nature* **323**, 235.

Libbrecht, K. G., and Woodard, M. F. 1990, *Nature* **345**, 779.

Libbrecht, K. G., Woodard, M. F., and Kaufman, J. M. 1990, *Ap. J. Supp.* **74**, 1129.

Libbrecht, K. G., and Zirin, H. 1986, *Ap. J.* **308**, 413.

Lighthill, M. J. 1952, *Proc. Roy. Soc. A* **211**, 564.

Lyot, B. 1933, *Comptes Rendus* **197**, 1593.

Mosher, J., 1976, BBSO preprint #0159.

Murray, N. W. 1990, private communication.

Nishikawa, J., Hamana, S., Mizugaki, K., and Hirayama, T. 1986, *Publ. Astron. Soc. Japan* **38**, 227.

Peri, M. L. 1988, private communication.

Pierce, A. K., and Waddell, J. H. 1961, *M. N. R. A. S.* **68**, 89.

Pintar, J. A., and the GONG Data Team 1988, in *Seismology of the Sun and Sun-like Stars*, ed. E. J. Rolfe (Noordwijk: ESA), p. 217.

Press, W. H., Flannery, B. P., Teukolsky, S. A., and Vetterling, W. T. 1986, *Numerical Recipes: The Art of Scientific Computing* (Cambridge: Cambridge University Press).

Rhodes, E. J., Jr., Ulrich, R. K., and Simon, G. W. 1977, *Ap. J.* **218**, 901.

Roberts, B., and Campbell, W. R. 1988, in *Seismology of the Sun and Sun-like Stars*, ed. E. J. Rolfe (Noordwijk: ESA), p. 311.

Scherrer, P. H., Hoeksema, J. T., Bogart, R. S., and the SOI Co-Investigator Team 1988, in *Seismology of the Sun and Sun-like Stars*, ed. E. J. Rolfe (Noordwijk: ESA), p. 375.

Scherrer, P. H., Wilcox, J. M., Christensen-Dalsgaard, J., and Gough, D. O. 1982, *Nature* **297**, 312.

Severny, A. B., and Kotov, V. A. 1984, *Adv. Spa. Res.* **4**, 129.

Shibahashi, H., and Sekii, T. 1988, in *Seismology of the Sun and Sun-like Stars*, ed. E. J. Rolfe (Noordwijk: ESA), p. 471.

Stein, R. F., and Leibacher, J. W. 1981, in *The Sun as a Star*, ed. S. Jordan (Washington, D. C.: NASA), p. 289.

Stix, M. 1989, *The Sun: An Introduction* (Berlin: Springer-Verlag), §5.3.

Tassoul, M. 1980, *Ap. J. Supp.* **43**, 469.

Toomre, J. 1984, in *Solar Seismology from Space*, ed. R. K. Ulrich (Pasadena: Jet Propulsion Laboratory), p. 7.

Toomre, J. 1986, in *Seismology of the Sun and Distant Stars*, ed. D. O. Gough (Dordrecht: Reidel), p. 1.

Tsay, W.-S., Bagnuolo, Jr., W. G., McAlister, H. A., White, N. M., and Forbes, F. F. 1990, *Pub. A. S. P.* **102**, 1339.

Ulrich, R. K. 1970, *Ap. J.* **162**, 993.

Ulrich, R. K., Rhodes, E. J., Jr., Cacciani, A., and Tomczyck, S. 1984, in *Solar Seismology from Space*, ed. R. K. Ulrich (Pasadena: Jet Propulsion Laboratory), p. 263.

Unno, W., Osaki, Y., Ando, H., Saio, H., and Shibahashi, H. 1989, *Nonradial Oscillations of Stars* (2nd ed.; Tokyo: University of Tokyo Press), §41.

Vandakurov, Y. V. 1967, *Astron. Zh.* **44**, 786.

Vorontsov, S. V. 1988, in *Seismology of the Sun and Sun-like Stars*, ed. E. J. Rolfe (Noordwijk: ESA), p. 475.

Vorontsov, S. V., and Zharkov, V. N. 1989, *Sov. Sci. Rev. E. Ap. Space Phys.* **7**, 1.

Woodard, M.F., and Hudson, H. S. 1983, *Nature* **305**, 589.

Woodard, M. F., and Libbrecht, K. G. 1988, in *Seismology of the Sun and Sun-like Stars*, ed. E. J. Rolfe (Noordwijk: ESA), p. 67.

Zirin, H., 1985, *Aust. J. Phys.* **38**, 961.